



POLITECNICO
MILANO 1863

**SCHOOL OF INDUSTRIAL AND INFORMATION
ENGINEERING**

Master of Science in Materials Engineering and Nanotechnology

**RHEOLOGICAL STUDY AND INKJET PRINTING OF DOPANT
SOURCE INKS FOR APPLICATIONS IN HIGH EFFICIENCY
SILICON SOLAR CELLS**

Thesis Supervisor: Dr. Francesco Briatico Vangosa

Co-rapporteur: Dr. Roberto Chiesa

Research Supervisor: Dr. Zohreh Kiaee

Research Advisors: Dr. Roman Keding, Dr. Christian Reichel

Zulkifl Hussain

Matricola-898007

Student ID- 10604335

Academic year 2019/2020



This research has been carried out at the
Fraunhofer Institute of Solar Energy (ISE), Division Photovoltaics, Department of
Production Technology - Structuring and Metallization

Freiburg im Breisgau
October 2019 - April 2020

*To the ones who complete me-
my parents, Ubaid and Zun-nun;
to their selfless love and to their faith in me.*

DATA PROTECTION STATEMENT

This thesis contains internal confidential information of the Fraunhofer Institute for Solar Energy Systems. It may only be inspected by the reviewers and authorized members of the examination committee. It is not permitted to use contents of the thesis (including data and drawings) in whole or in part. No copies or transcripts of any kind, not even in digital form, may be made. Exceptions are possible but require the written consent of the Fraunhofer Institute for Solar Energy Systems

Die vorliegende Arbeit beinhaltet interne vertrauliche Informationen des Fraunhofer-Instituts für Solare Energiesysteme. Die Einsicht ist nur durch die Gutachter sowie berechnigte Mitglieder des Prüfungsausschusses gestattet. Die Weitergabe des Inhalts der Arbeit sowie eventuell beiliegender Daten und Zeichnungen im Gesamten oder auszugsweise ist nicht gestattet. Es dürfen keinerlei Kopien oder Abschriften-auch nicht in digitaler Form- gefertigt werden. Ausnahmen bedürfen der schriftlichen Zustimmung des Fraunhofer-Instituts für Solare Energiesysteme, ISE.

Questo documento contiene informazioni interne riservate dell'Istituto Fraunhofer per i sistemi di energia solare. Può essere ispezionata solo dagli esperti e dai membri autorizzati della commissione d'esame. Non è consentito trasmettere il contenuto della carta o i dati e i disegni allegati in tutto o in parte. Non possono essere effettuate copie o trascrizioni di alcun tipo, nemmeno in forma digitale. Le eccezioni richiedono il consenso scritto del Fraunhofer Institute for Solar Energy Systems, ISE.

Zulkifl Hussain

April 2020

DECLARATION OF ORIGINALITY

I, Zulkifl Hussain, declare that this master's thesis entitled "**RHEOLOGICAL STUDY AND INKJET PRINTING OF DOPANT SOURCE INKS FOR APPLICATIONS IN HIGH EFFICIENCY SILICON SOLAR CELLS**" has not been submitted elsewhere and was produced without external aid and is entirely my own work. All materials used in this research are quoted or acknowledged as appropriate.

Place, Date

Name

ESTRATTO

La tecnologia di stampa a getto d'inchiostro offre una soluzione economicamente conveniente e tecnologicamente fattibile per l'upscaling della tecnologia delle celle solari, in particolare per la produzione di prossima generazione 4.0 di celle solari ad alta efficienza con TOPCon (Tunneling Oxide Passivated Contact). Il lavoro di questa tesi è dedicato allo sviluppo di processi di stampa ottimizzati specifici per l'inchiostro. A tal fine viene condotta un'analisi reologica degli inchiostri, correlata ai parametri di stampa a getto d'inchiostro. Le strutture stampate con successo sono state ulteriormente caratterizzate per valutare le prestazioni elettriche degli inchiostri.

È stata analizzata la risposta reologica rispetto alla frequenza, alla temperatura e al tempo di invecchiamento. Per quanto riguarda la frequenza, i risultati sono stati ottenuti per un intervallo di 1-10.000 Hz. Secondo i risultati ottenuti nell'intervallo a getto d'inchiostro (2000Hz - 5000Hz), gli inchiostri con viscosità complessa (η^*) nell'intervallo 2-20mPa.s (costante o variabile), di solito producono risultati di stampa lisci. La tensione di azionamento richiesta per il getto d'inchiostro con questa viscosità si avvicina a 25V, la tensione di impulso predefinita della stampante a getto d'inchiostro. Tuttavia, il comportamento complessivo di stampa dipende maggiormente dal modulo elastico (G'). Gli inchiostri con modulo elastico inferiore a 10Pa e, cosa più importante, con una tendenza generale non crescente (almeno vicino alla gamma di frequenza di stampa a getto d'inchiostro), favoriscono buone caratteristiche di stampabilità come il minimo intasamento dell'ugello e la formazione ideale di goccioline. Inchiostri altamente viscosi con valori di G' fino a 200 Pa, non riescono a spurgare a causa dell'elasticità estremamente elevata. Un'elasticità troppo elevata può portare al fallimento della separazione delle gocce. È stato studiato anche il ruolo del modulo viscoso (G''). A causa della natura fluida intrinseca degli inchiostri, G'' , che aumenta linearmente con la frequenza, è stato sempre trovato superiore a G' . La reologia rispetto alla temperatura è stata studiata sottoponendo gli inchiostri a 25°C e 45°C. Si è scoperto che la maggior parte degli inchiostri obbedisce alle leggi convenzionali e mostra una riduzione delle loro proprietà (η^* , G' , G'') con l'aumento della temperatura. Alcuni inchiostri, tuttavia, hanno mostrato l'effetto opposto - i valori delle proprietà aumentano con la temperatura. Per tali inchiostri è stata tracciata una correlazione tra la stampa e i parametri critici. Oltre alla temperatura, è stato studiato anche l'invecchiamento degli inchiostri e l'impatto della loro durata di conservazione.

La caratterizzazione elettrica condotta in questa tesi, presenta uno studio comparativo delle caratteristiche elettriche degli stessi inchiostri su due diversi substrati. Entrambi i substrati possiedono un alto ma diverso livello di qualità di passivazione superficiale attraverso diverse profondità di c-Si/SiOx/poliestere sviluppato su campioni di durata. La passivazione dei contatti è realizzata da un ossido di silicio ultrasottile (SiOx) e da uno strato di poli-Si (TOPCon). Questi progressi sono considerati una tecnologia di follow-up delle celle PERC e hanno reso TOPCon una tecnologia superiore. TOPCon riduce al minimo la ricombinazione della superficie, consente una bassa resistività di contatto e fornisce un'elevata stabilità termica. Pertanto, in questo lavoro, è stata affrontata anche la soluzione industrialmente rilevante per la formazione di strati di n-

TOPCon drogati selettivamente, utilizzando la stampa a getto d'inchiostro con l'obiettivo di fornire una bassa resistenza di contatto. Si dimostrerà che la stampa a getto d'inchiostro di fonti di droganti al fosforo per la deposizione di vapori chimici depositati (PECVD) a spessore con plasma potenziato TOPCon fornisce un'eccellente passivazione superficiale con $iV_{oc} = 734$ mV, $iFF = 87\%$, e una sufficiente concentrazione di doping di Npoly-Si $\sim 2 \times 10^{20}$. Allo stesso modo, per i sottili strati TOPCon di deposito di vapore chimico a bassa pressione depositati (LPCVD) abbiamo ottenuto ancora una volta una notevole passivazione superficiale con $iV_{oc} = 710$ mV, $iFF = 85\%$. Più campioni di entrambi i tipi sono stati sottoposti a diversi trattamenti termici, stabilendo così le migliori condizioni per ogni tipo, al fine di ottenere risultati molto promettenti.

ABSTRACT

Inkjet printing technology offers an economically viable and technologically feasible solution for upscaling solar cell technology, especially for next-generation manufacturing 4.0 of high-efficiency solar cells with TOPCon (Tunneling Oxide Passivated Contact). The work in this thesis is dedicated to the development of ink-specific optimized printing processes. To this end, rheological analysis of the inks is conducted and correlated with inkjet printing parameters. Successfully printed structures were further characterized to assess the electrical performance of the inks.

Rheological response with respect to frequency, temperature and aging time was analyzed. With respect to frequency, results are obtained for a range of 1-10,000Hz. According to the results obtained in the inkjet range (2000Hz – 5000Hz), inks with complex viscosity (η^*) in the range of 2-20mPa.s (constant or varying), usually produce smooth printing results. Actuation voltage required for jetting inks with this viscosity lies close to 25V, the default pulse voltage of inkjet printer. However, overall printing behavior depends more on elastic modulus (G'). Inks with elastic modulus less than 10Pa and more importantly, with an overall non-increasing trend (at least near the inkjet printing frequency range), favor good printability features such as minimum nozzle clogging and ideal droplet formation. Highly viscous inks with G' values as high as 200 Pa, fail to purge due to extremely high elasticity. Too high elasticity can lead to failure of drop separation. The role of viscous modulus (G'') was also studied. Due to the inherent fluid nature of inks, G'' , which increases linearly with frequency, was always found to be higher than G' . Rheology with respect to temperature was studied by subjecting the inks to 25°C and 45°C. It was found that most inks obey conventional laws and show reduction in their properties (η^* , G' , G'') with increasing temperature. Some inks, however, exhibited the opposite effect - properties' values increased with temperature. For such inks, correlation between printing and critical parameters has been drawn. Besides temperature, aging of inks and the impact of their shelf lives has also been studied.

Electrical characterization conducted in this thesis, presents a comparative study of electrical characteristics of same inks on two different substrates. Both substrates possess high but different level of surface passivation quality through different depths of c-Si/SiOx/poly-Si junction developed on lifetime samples. Passivation of contacts is realized by an ultra-thin silicon oxide (SiOx) and an efficiently-doped poly-Si layer (TOPCon). These advancements are considered a follow-up technology of PERC cells and have made TOPCon a superior technology. TOPCon minimizes surface recombination, enables low contact resistivity, and provides high thermal stability. Therefore, in this work, industrially relevant solution for the formation of selectively doped *n*-TOPCon layers has also been addressed, by utilizing inkjet printing with the goal to provide a low contact resistance. It will be shown that inkjet printing of phosphorus dopant sources for thick plasma-enhanced chemical vapor deposition deposited (PECVD) TOPCon layers provides excellent surface passivation with $iVoc = 734$ mV, $iFF = 87\%$, and a sufficient doping concentration of $N_{poly-Si} \sim 2 \times 10^{20}$. Similarly, for thin low pressure chemical vapor deposition deposited (LPCVD) TOPCon layers we again obtained remarkable surface passivation with $iVoc = 710$ mV, $iFF = 85\%$. Multiple samples of both kinds have undergone different heat treatments thus setting forth best conditions for each kind to obtain highly promising results.

Table of Contents

ABSTRACT	viii
Chapter 1 Introduction	1
1.1 Motivation	1
1.2 Aim of the thesis	2
1.3 Thesis outline	3
Chapter 2 Fundamentals	4
2.1 Photovoltaic effect and semiconductors.....	4
2.1.1 Charge carriers	7
2.1.2 Diffusion of dopants.....	8
2.2 Principles of solar cell operation.....	10
2.2.1 Recombination	12
2.2.2 Charge carrier lifetime	14
2.3 Passivation.....	15
2.4 Rheology	18
2.4.1 Dynamics of rheology: Role of time scale	21
2.4.2 Rheology of polymer solutions	22
2.4.3 Temperature Dependence.....	26
2.4.4 Aging of polymers.....	26
2.4.5 Model fitting.....	28
2.5 Inkjet Printing Technology.....	35
2.5.1 Inkjet mechanism	35
Inkjet process development.....	38
Chapter 3 Experimental setup and Tools	44
3.1 Experimental Design	44
3.1.1 Lifetime sample development	45
3.2 Ink Characterizations.....	50
3.2.1 Dopant source inks	50
3.2.2 Rheological Measurements	51
3.2.3 Picoscope-Oscilloscope Measurements	57

3.3	Inkjet Printing.....	59
3.4	Printed Sample Characterization	61
3.4.1	Optical Microscope	61
3.4.2	Electrochemical Capacitance Voltage (ECV)	62
3.4.3	Quasi-Steady-State Photo-Conductance (QSSPC).....	63
Chapter 4 Results and Discussion.....		65
4.1	Rheometry	65
4.1.1	Rheological analysis with respect to frequency	65
4.1.2	Rheological analysis with respect to temperature	85
4.1.3	Rheological analysis with respect to aging time	94
4.2	Inkjet Printing Process Development	99
4.2.1	Waveform simulation	99
4.2.2	Optimization of Printing Parameters	103
4.3	Electrical Properties of inks	107
4.3.1	Evaluation of passivation quality of P-doped TOPCon layers.....	107
4.3.2	Evaluation of Passivation Quality after Hydrogen Passivation (RPHP).....	112
4.3.3	Evaluation of charge carrier profiles	118
Chapter 5 Summary and Outlook		122
List of Figures		127
List of Symbols.....		132
List of Acronyms and Abbreviations.....		133
References		134
ACKNOWLEDGEMENT		141

This page is intentionally left blank.

Chapter 1

Introduction

1.1 Motivation

As a measure to increase the photo-conversion efficiency (PCE) of solar cells, introduction of a Tunneling Oxide Passivated Contact (TOPCon) layer between the wafer substrate and the doped poly-Si layer has played a very important role. The implementation of TOPCon technology has led to the achievement of 25.8% [1] PCE. Results are further enhanced by using passivating contacts on Interdigitated Back Contact (IBC) solar cell - efficiency reaching up to 26.7% [2]. As shown in Figure 1.1, both contacts on IBC solar cells are located on one side of the wafer. Fabrication of such a device requires many patterning steps and the specific architecture of such cells demands precision of consecutive or even simultaneous patterning process, e.g. local printing of Boron (B) and Phosphorus (P) dopant sources. Precision at each step plays a deterministic role in efficiency improvement. Besides improving the efficiency, another major concern related to the development of such devices, is their price. Inkjet printing offers a simple and a cost efficient route and thus addresses all such concerns. The appeal of this technology lies in its flexibility, precision, digital printing templates, feature size down to $20\mu\text{m}$ [3] (using drop volume as low as 1pl) and the non-contact mode. Because of its non-contact mode, wafer breakage and contamination during solar cell manufacturing is significantly reduced, which is extremely important for high efficiency solar cell fabrication.

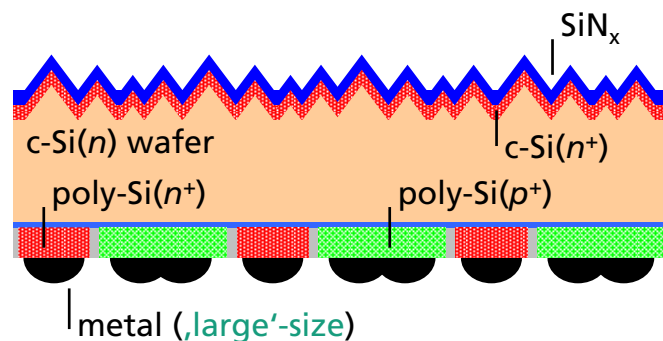


Figure 1.1: Schematic cross-section of different IBC solar cells containing thin, highly doped c-Si (crystalline Si) below passivating nitride layer.

The main considerations of printing technology are those of achieving small feature size, homogenous and uniformly printed layers and development of structures with accurate design and – in case of their application in mass production – process stability. All these quality parameters require a fundamental understanding on rheology of printing media and the investigation of adequate process-material combinations, as objected in this thesis. For the applications considered in this thesis, dopant sources are locally printed over TOPCon layers. Development of a non-uniform printed layer would lead to inhomogeneous distribution of charge carriers which would further lead to non-uniform passivation of contacts over a single device. Similarly, inaccurate design would produce an overall inefficient system. Motivation behind the work of this thesis lies in finding solutions to such problems encountered while printing and to minimize them by developing optimum printing procedures.

Common problems faced during printing dopant source inks emerge due to their complex rheology, since most of them are polymer based solutions. Rheology dictates the droplet formation and the possibility of related structural defect generation. However, due to certain level of flexibility offered by the rheological properties, we can tune the response of inks according to our requirements. This can be done by varying the external parameters of inkjet printer, such as applied pressure behind nozzle plate, temperature of print-head, voltage and timing of the (actuation and printing) waveform and frequency of firing. Finding such ways of tailoring the behavior of inks and producing smooth printing results is the key motivation behind this work.

1.2 Aim of the thesis

The main aim of this thesis is to address the viability of dopant source inks for inkjet printing process, to develop the process according to specific characteristics of the inks and finally conduct local doping of high efficiency silicon solar cells using those inks.

The approach used, in order to reach this target is through several steps such as, fundamental understanding of the rheological properties of inks, investigation of adequate process-material combinations and characterization of doped silicon layers by typical quality parameters of solar cells.

Accordingly, the main objectives of this thesis are:

- Investigation of rheological parameters for inks used as dopant sources of phosphorus and boron. Rheological properties of inks determine their behavior in response to the stimulus of shear strain, which is applied through the piezoelectric nozzles of inkjet printer. Therefore, the success in obtaining desired print designs for our devices is determined, to a large extent, by rheology of the inks. Rheology of inks in response to shear strain (or frequency), temperature and aging time has been studied. This gives a better understanding of feasible approach that needs to be adopted for each ink during its printing process. The inks used in this work differ in terms of their base polymer concentration, phosphorous (P)/boron (B) concentration in the polymer chains,

concentration of solvents, additives, etc., all of which determine their varied rheological response.

- Adaption of rheological parameters for inkjet printing, through the selection of particular temperature, pressure and frequency range in which each polymer ink behaves desirably. Ideal printing behavior means minimum nozzle clogging, absence of satellites, tails, ligaments and threads and homogeneous and precise deposition of ink over the substrate.
- Process integration into specific sampling for the characterization of ink-substrate interaction, charge carrier concentration and electrical properties like minority charge carrier lifetime. The relevant characteristics investigated are iV_{oc} and iFF .

From a broader perspective therefore, this thesis aims to tune the inkjet printing technology through small measures and steps with the intention of reducing the distance that remains to reach the larger aim of promoting clean and green energy.

1.3 Thesis outline

Chapter 2: This chapter explains the science behind the concepts and the technology used in this thesis. It includes a brief introduction to the Photovoltaic effect, semiconductors and solar cells. The second part of the chapter includes a comprehensive study on rheology of polymers and the theory behind the changing response of polymers to various stimuli. The last part of the chapter focuses on inkjet printing technology, its mechanism and the process development according to our requirements.

Chapter 3: This chapter describes the experimental design adopted for this thesis and explains the tools used to characterize dopant source inks and lifetime samples at various stages of thesis experimentation.

Chapter 4: This chapter explains in detail the results obtained, ensued by their relevant discussions. The first part of the chapter concerns rheological analysis and the study of rheology of dopant source inks with respect to frequency, temperature and aging time. The second part deals with inkjet process and the optimization of the process according to the requirement of inks. The last part of this chapter explains the results obtained upon electrically characterizing the passivated contacts hence developed, on different lifetime samples.

Chapter 5: This chapter summarizes the work done in thesis and from the conclusions deduced mentions the prospective steps which can be taken in order to further improve the process of printing and achieve better results.

Chapter 2

Fundamentals

This chapter focuses on fundamental concepts governing the materials, their intrinsic properties, and the science behind the technologies used in this work

2.1 Photovoltaic effect and semiconductors

Photovoltaic effect – the fundamental effect, on which the solar industry operates, consists of two main effects. The foremost is the absorption of light, which generates electron-hole pairs followed by separation of these two charge carriers channelized by the structure of the device – electrons being shifted to the negative terminal and holes to the positive terminal, generating large voltages across the solar cell, as shown in Figure 2.1. The two steps result in the production of photo-electric power, which is dissipated across the load and the parasitic resistances of the circuit. The generation of such power is only possible if the energy supplied by sunlight is enough to meet the energy requirements of both steps mentioned above. This requires a match between the band gap of the material (the energy by which the conduction and the valence bands are separated) and the solar energy. Semiconductors offer the possibility of both, absorption of solar spectrum and production of large built-in voltage. As a result, semiconductors produce a band gap between 1.0 and 1.7 eV (1.1 eV for crystalline Silicon). In this range electrons can be freed from the atoms, without creating too much heat. The energy of the photons supplied through solar radiations varies depending on the wavelength of the spectrum. The entire spectrum, ranging from infrared (IR) to ultraviolet (UV) radiation offers energy in the range of 0.5 eV to ~2.9 eV. However, semiconductors do not respond to the entire solar spectrum, as a result of which solar cells cannot be 100% efficient. Photons with energy less than the bandgap of semiconductors, pass the material without absorption, which accounts about 18% of the incoming energy. The amount of radiation with energy above the bandgap is re-emitted as heat or light, accounting for additional 49% loss. This amounts to a loss of ~ 67% of the energy obtained from the Sun which leaves only 33% available for an ideal solar cell [4].

Radiations of energy greater than the band gap, can alter the atomic structure of the material by freeing a bound electron from the nucleus, which is then able to move around in the crystal and thus conduct electricity. This is the fundamental concept that lies behind the operation of semiconductors. As electrons leave the atom, there is a rise of positive charge density in its vicinity, which is known as a “hole” or a “positron” (the positive counterpart of electron). Free electrons (and holes) which can move (or appear to move) around in the crystal comprise the conduction band, while the charges bound to the nucleus form the valence band. The electrons and holes liberated from atomic bonds in this manner are called light-generated electron-hole (e-h) pairs. The movement of these pairs is further increased with rising temperature which supplies thermal energy (to be later converted into kinetic energy).

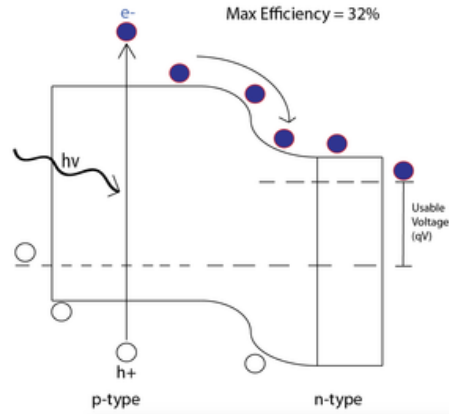


Figure 2.1: p-n junction of a silicon solar cell with e-h pairs being created by incoming photons with energies of $h\nu$ and electrons being swept away to the right to be used for electricity [5].

An ideal solar cell must have a direct band gap of 1.4 eV to absorb maximum number of photons from the solar radiation. Silicon, on the other hand, has an indirect band gap of 1.1 eV. Difference between direct and indirect bandgap semiconductors is shown in Figure 2.2. Silicon is not an ideal material for solar cells, but it provides several advantages. It is mechanically very stable, sharing the same crystal structure as diamond (Figure 2.3), it is non-toxic, it is the second most abundant element in the earth's crust, and silicon engineering has already been heavily studied (manufacturing of wafers, doping, patterning, and making electrical contacts are all well understood).

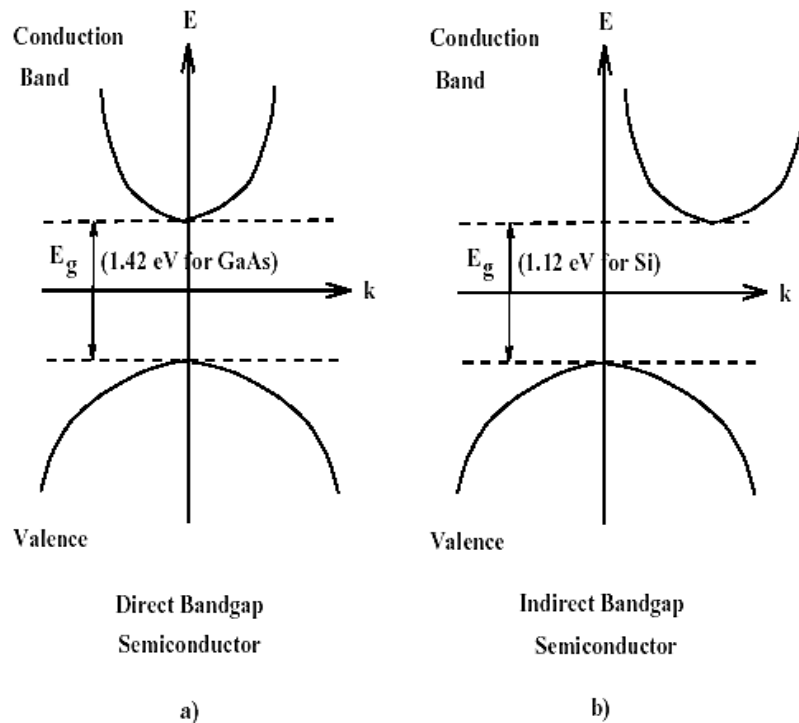


Figure 2.2: Energy Band Diagram with E versus k for a) GaAs and b) Silicon [6].

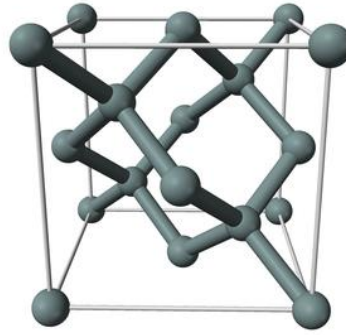


Figure 2.3: Diamond crystal structure of Silicon atom [5].

The seemingly infinite lattice of a crystal creates bands of allowed energy states. But, due to the presence of a band gap of a certain width, a zone is created where no charge carriers are allowed to exist; silicon creates a band gap with a width of 1.1eV. Allowed states exist beyond the two ends of this range, thus defining the valence band – below the band gap and conduction band – above the band gap. However, electrons can be excited through this band gap into the conduction band from where they can be extracted for conducting electricity. Conductors (metals typically) on the other hand can be understood analogous to a sea of electrons where there is no band gap. Classification of materials on the basis of energy band gaps is shown in Figure 2.4. Doping silicon with different elements changes the electronic structure and imbues new properties into silicon. Dopants introduce new energy states within the band gap. Boron doping creates p-type silicon (excess holes/electron acceptors) with new levels close to valence band – acceptor sites. Similarly, phosphorus doping creates n-type silicon (excess electrons) with new energy levels lying close to the conduction band – donor sites. The presence of these additional energy levels known as “dopant-site bonding energy (E_B)” reduces the width of the barrier and allows easier excitement and transfer of electrons, leading to conduction of electricity. The value of ‘ E_B ’ can be easily met with the thermal energy gained at room temperature ($k_B T$), which is enough to generate charge carriers, in their respective bands. On combining p-type and n-type silicon a p-n junction is generated, which separates electron and hole pairs to sweep away electrons as current.

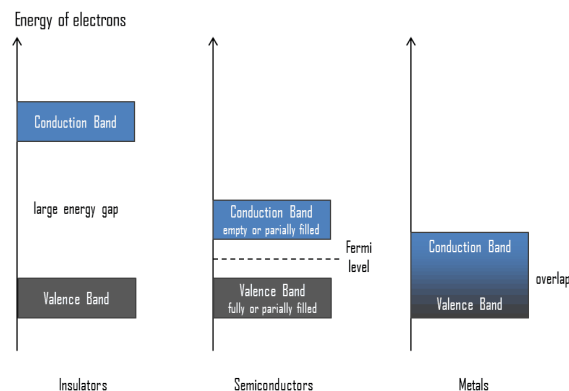


Figure 2.4: Energy bands (Valence band and Conduction band) of insulators, semiconductors and metals [7].

2.1.1 Charge carriers

We can classify charge carriers into two categories- *intrinsic* and *extrinsic*. Intrinsic charge carriers constitute the electrons and the holes, which are intrinsic to the structure of the semiconductor. Their role in conduction of electricity has been defined in the previous section. At room temperature, the conductivity generated through them is extremely low to account for any significant value. They make substantial contributions at high temperatures. The number of intrinsic charge carriers (n_i) is always the same, i.e. the number of electrons (n_0) will always be equal to the number of holes (p_0), to maintain the overall electrical neutrality, according to the electron mass action law and is written as,

$$n_i = n_0 = p_0 \quad (2.1)$$

The conductivity of an intrinsic semiconductor is expressed in the terms of mobility and concentration of the charge carriers, as described by the following equation:

$$\sigma_i = n_i e(\mu_e + \mu_h) \quad (2.2)$$

where, σ_i is the conductivity of an intrinsic semiconductor, n_i is the intrinsic carrier concentration, μ_e is the mobility of electrons and μ_h is the mobility of holes. For Silicon, the intrinsic charge carrier concentration is, $n_i = 1.5 \times 10^{10} \text{ cm}^{-3}$.

The extrinsic charge carriers, on the other hand are the ones which are externally added to the semiconductor to increase their number and hence the overall conductivity. In case of Si semiconductors, extrinsic charge carriers are provided by doping the element with other elements of group II, III, V or VI.

Elements belonging to lower groups, such as Boron (B), which possess only three valence electrons, produce deficiency of electrons and enrichment of holes when added to Silicon and change the semiconductor into '*p-type*', i.e. possessing extra positive charge carriers. On the other hand, elements belonging to higher groups, such as Phosphorus (P), which possess five electrons, contribute to the addition of negative charge carriers and change the neutral semiconductor to be electron rich, written as '*n-type*'.

Dopants can be added to semiconductors in the form of solids (As_2O_3 , Sb_2O_3 for n-type and B_2O_3 and BN for p-type), liquids (PBr_3 , POCl_3 for n-type and BBR_3 for p-type) and gases (AsH_3 and PH_3 for n-type and B_2H_6 and BCl_3 for p-type). However, after coming in contact with the semiconductor surface, dopants need to diffuse into the bulk in order to reach and displace Silicon atoms. The mechanism is explained in the following section.

2.1.2 Diffusion of dopants

Diffusion is the movement of molecules or particles along the concentration gradient in order to attain homogenous distribution of constitutive elements, which in our case are group III and group V elements. There are various factors that determine the rate and efficiency of diffusion, especially the size of the dopants. Since the dopants have to travel through Si crystal, diffusion of smaller atoms is faster compared to bigger ones. Diffusion has been explained through Fick's first and second laws related to concentration gradient and the rate of diffusion, respectively.

Fick's first law

According to Fick's first law the flux of atoms along direction x is proportional to the concentration gradient and is described by:

$$J_D = -D \frac{\partial C}{\partial x} \quad (2.3)$$

where, D represents the *diffusivity* or *diffusion coefficient*, dC/dx is the concentration gradient and J_D is the flux describing the amount of atoms that will flow through infinitesimal area in infinitesimal time. Minus sign signifies the motion of particles down the concentration gradient.

The diffusivity, D , of the dopants in the material, is mathematically defined according to the Arrhenius law as:

$$D = D_0 \exp\left(-\frac{E_A}{k_B T}\right) \quad (2.4)$$

where k_B is the Boltzmann constant, T is the absolute temperature, E_A is the activation energy, and D_0 is the diffusivity constant (material specific). Temperature and the activation energy strongly influence the dopant diffusion. Furthermore, the mechanism of diffusion related to the diffusivity is a function of the dopant concentration. The boron diffusion mechanism is related to the silicon self-interstitials [8] and under non-oxidizing atmosphere, boron atoms diffuse exclusively through vacancy mechanism. However, phosphorus diffusion mechanism depends on the phosphorus concentration, thus generating different slopes in the diffusion curve, as will be seen later in Chapter 4. For the concentration level above 10^{20} cm^{-3} , a fraction of P^+ ions pair with V^- vacancies and form $(PV)^-$ pairs, the concentration of which is proportional to surface electron concentration cubed (n_s^3). For such higher concentration, phosphorus diffuses through the mechanism of vacancies and interstitial sites [9]. At lower concentration the V^- vacancy changes state and the binding energy decreases enhancing the probability of dissociation of $(PV)^-$ pairs and increasing the vacancy flux. According to Vick and Whittle, boron diffusivity in silicon is a constant - $6.0 \cdot 10^{-11} \text{ m}^2/\text{s}$ for the impurity levels below $10^{24} \text{ atoms/m}^3$. Above this impurity level, the diffusivity becomes dependent on the impurity levels [10].

Fick's second law

Fick's first law however assumes an infinite source of diffusing elements without any change in their availability, which is seldom found in reality. Fick's second law is more realistic, considering exhaustion of dopant sources and can be derived using Fick's first law and the continuity equation.

It describes the dependence of the dopant concentration on time through the following partial differential equation in one dimension;

$$\frac{dc}{dt} = D \frac{d^2c}{dx^2} \quad (2.5)$$

where, the time-dependent change in dopant concentration at a fixed position is a function of the change in the concentration gradient along the x-coordinate.

Thus, depending on the boundary conditions, we have two kinds of dopant sources:

- (1) Finite dopant source and
- (2) Infinite dopant source,

the concentration of which varies with time, as shown in Figure 2.5.

In infinite dopant source, the amount of dopant does not diminish substantially over time, which enables an almost constant concentration of dopants. The time-dependent progress of the dopant concentration profile in the dopant receiver is:

$$C(x, t) = C_s \operatorname{erf} \left(c \frac{x}{2\sqrt{Dt}} \right) \quad (2.6)$$

where, C_s is the dopant concentration at the interface between the dopant receiver and the dopant source. The amount of dopant at the interface remains constant with time during the diffusion. However, in case of a finite dopant source, which diminishes over time, concentration is given by:

$$C(x, t) = \frac{DA}{\sqrt{\pi Dt}} \exp \left(-\frac{x^2}{4Dt} \right) \quad (2.7)$$

where, DA is the dopant assignment of the dopant source given by the product of dopant concentration and the layer thickness of the dopant source. In this case, the dopant concentration at the interface between the dopant source and the receiver decreases with time. The deduced profiles of dopant concentration forecast the diffusion processes related to a single diffusion mechanism, for example, for boron. The concentration profiles for different regions of solar cell have a significant impact on the performance of the solar cell.

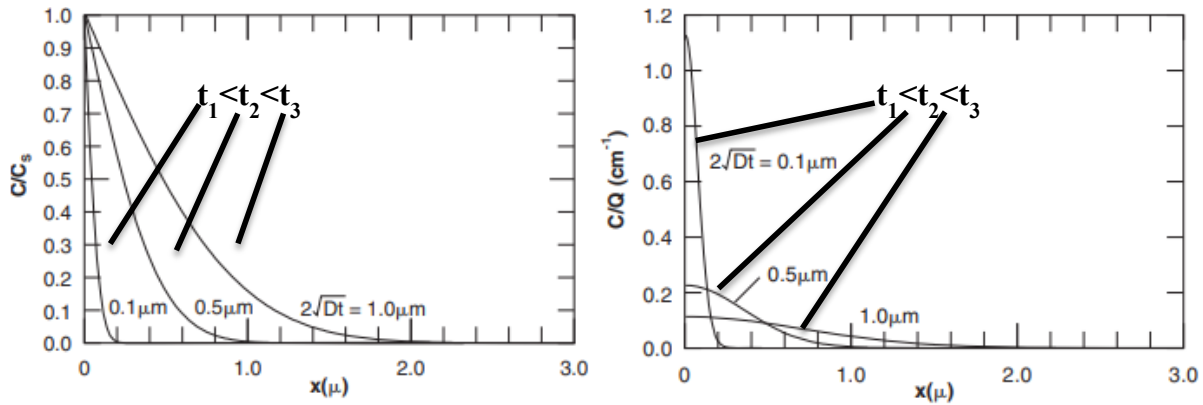


Figure 2.5: Infinite and finite diffusion sources [11].

2.2 Principles of solar cell operation

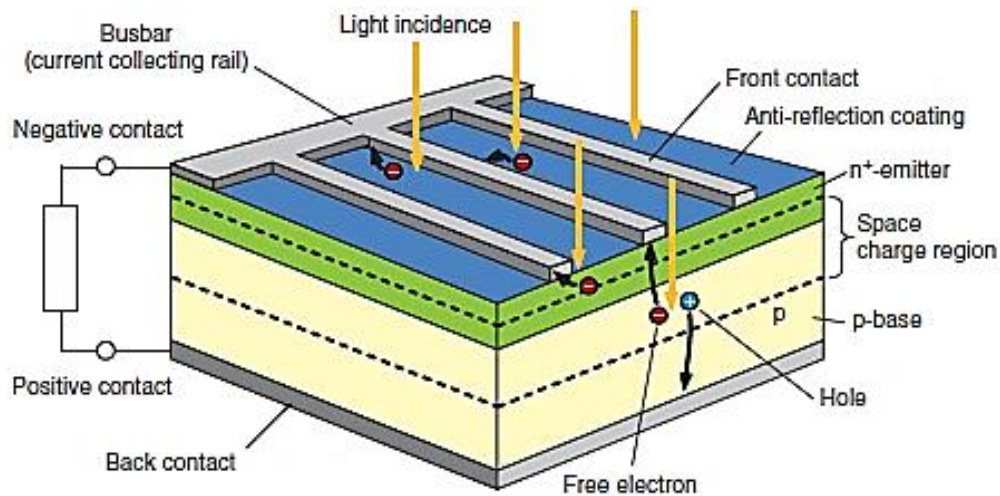


Figure 2.6: The complete structure and working of a solar cell [12].

A PV cell has three main regions; emitter, base and the space-charge-region (SCR). As shown in Figure 2.6, a conventional p -type cell, the emitter is 200 nm thick and highly negatively ($n+$) doped while the base is 180 μm thick and lightly positively (p) doped. SCR, as already mentioned, is the region that contains the fixed charges across the junction. The front surface is textured and provided with an antireflection coating (ARC), which reduces light reflection from the cell (colored in blue in Figure). Grid of electrode fingers on the front side of the cell are used to transport the generated electrons to the bus-bar for collection and finally to the metal contacts on both sides, negative on front and positive on rear side of the cell to which a load is connected, as shown.

The charge carriers, after separating, need to be collected by the p-n junction and the distance they have to travel before collection, i.e. the diffusion length, determines the probability of getting collected, termed as ‘collection probability’. The collection probability in the depletion region or the SCR is unity due to immediate sweeping of the charges by the built-in electric field. The further we move from the region, the lesser the collection probability. Moreover, the surface properties of the solar cell also plays a prominent role, as shown in Figure 2.7, thus making techniques such a surface passivation extremely beneficial.

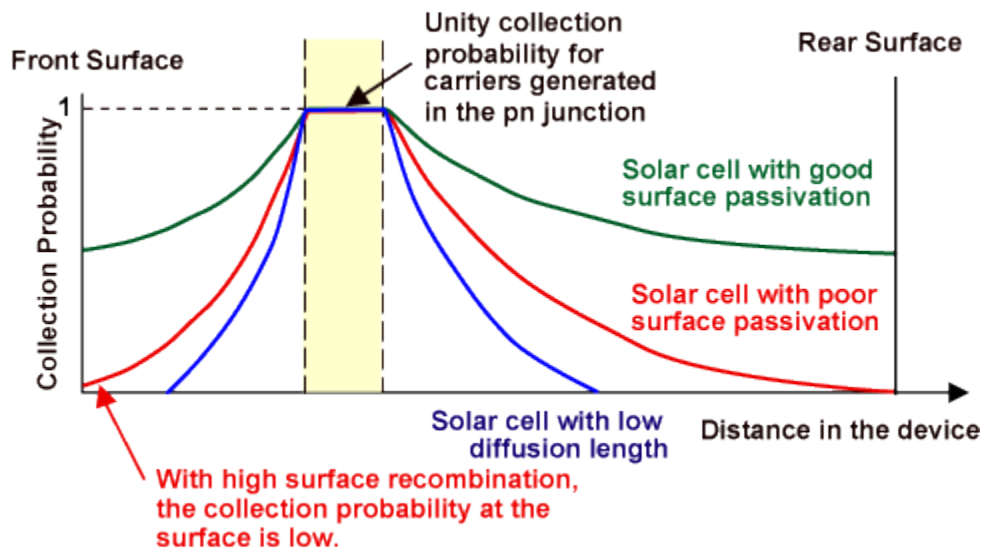


Figure 2.7: Collection probability of charge carriers under different circumstances [13].

An equivalent circuit of an ideal solar cell can be represented by a current source connected in parallel with a rectifying diode, as shown in Figure 2.8. The corresponding I-V characteristic is described by the Shockley solar cell equation (2.8):

$$I = I_{ph} - I_0 \left(\exp \frac{qV}{k_B T} - 1 \right) \quad (2.8)$$

where, q (> 0) is the electron charge and V is the voltage at the terminals of the cell. I_0 is the diode saturation current, explaining that the solar cell in the dark is simply a semiconductor current rectifier or a diode. The photo-generated current is dependent on the photon flux incident on the cell as well as on the wavelength of the incoming photons, marked by quantum efficiency or spectral response of the cell (the ratio of the current generated by the solar cell to the power incident on the solar cell).

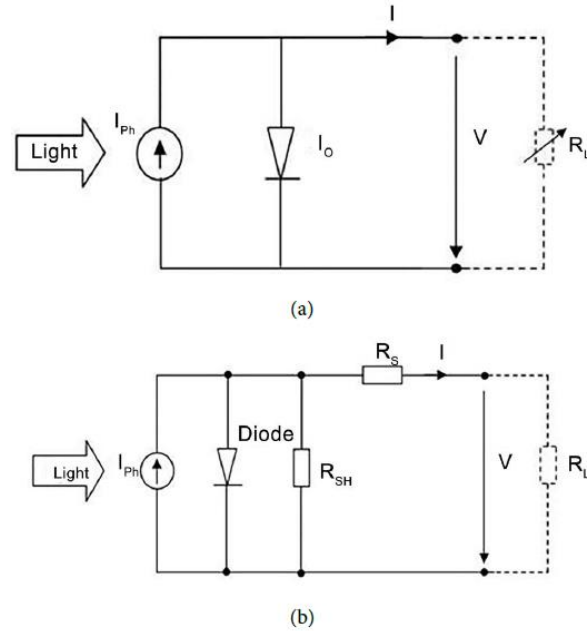


Figure 2.8: (a) Equivalent circuit of an ideal solar cell; (b) Practical solar cell equivalent circuit [14].

The photo-generated current is independent of the applied voltage except for amorphous Silicon (a-Si) and some thin film materials. I-V characteristics of an ideal solar cells are as shown in Figure 2.9, wherein the short-circuit current I_{sc} is equal to the photo-generated current I_{ph} , and the open-circuit voltage V_{oc} is given by

$$V_{oc} = \frac{k_B T}{q} \ln\left(1 + \frac{I_{ph}}{I_0}\right) \quad (2.9)$$

The cell generates a maximum power P_{max} at a voltage V_m and current I_m , through which we can conveniently define the fill factor FF as

$$FF = \frac{I_m V_m}{I_{sc} V_{oc}} = \frac{P_{max}}{I_{sc} V_{oc}} \quad (2.10)$$

2.2.1 Recombination

Of the several losses encountered in the whole process of photoelectric conversion, such as optical losses, resistance losses, degradation, etc., recombination losses are major contributors. They are material dependent and can be taken care of, to some extent. Recombination mechanisms can be classified into ‘direct’ and ‘indirect’ recombination based on whether the electrons and holes recombine with each other or due to interactions influenced by other circumstances. *Direct recombination*, which involves recombination of electrons and holes before they reach their respective terminals. It occurs rarely because usually the voltage supplied to separate the charges is strong enough to drive the charges apart before they randomly recombine with the majority charge carriers (e.g. holes getting filled with abundant electrons in n-type material). Direct recombination takes place in a time window of about one second. *Indirect recombination* is, however, more of a problem and e-h pairs are lost within a hundredth

of a second in average, hundred times faster than direct recombination. This gives us an idea of how fast the charges should be separated by the junction. Indirect recombination mechanisms are manifold and can be caused by empty or dangling bonds, from impurities, defects, or fractures, which can capture free electrons or holes. It can also be aided by random collisions of free charge carriers, which reduce their energy and increase their chance of forming a bond. This is related to the intrinsic resistance of the cell; higher resistance values cause higher recombination and also a loss in current and voltage.

Some of the common recombination mechanisms are pictorially explained in Figure 2.9.

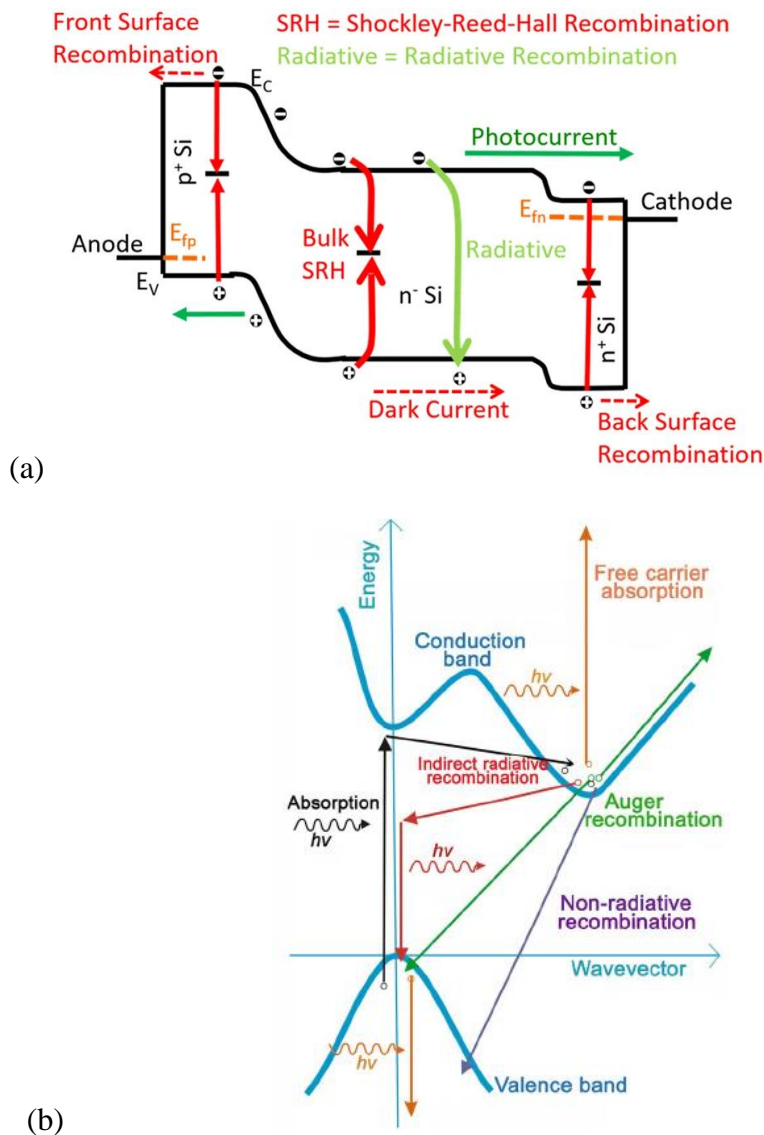


Figure 2.9: (a) Energy band diagram of a p/n/p junction solar cell showing common recombination mechanisms [15], (b) Energy vs wave-vector (k) representation of recombination mechanisms [16].

Surface Recombination

There are many aspects attributed to surface which cause recombination and impact the quantum efficiency of the solar cell. The largest possible disturbance of the symmetry of the crystal lattice is exhibited on the surface. This causes a large density of defects to be concentrated on the surface, due to the unsaturated dangling bonds. These defects can provide a pathway for the charge carriers through which they can effectively avoid the junction field. Charge carriers can thus filter back across the junction diminishing the cell voltage and current.

Surface defects can be intrinsic to the Si wafer or extrinsically induced through experimental procedures while preparing it. Defects manifest in several forms, such as surface charges, which can give rise to energy band bending and dislocations and grain boundaries, which can be associated to broken or strained bonds and impurities. The latter form planar defects and introduce bands of electronic states in the band gap.

Several methods have been developed over the years to reduce the surface recombination losses and hence *passivate* the surface. Using wafers produced through Float Zone (FZ) or Czochralski (Cz) process show very less surface defect generation intrinsic to Si, and have been used in this thesis. To further reduce the losses, the surface of FZ/Cz wafers can be further passivated by depositing a dielectric film on the surface, through chemical methods, using high-low junction, etc. In this thesis thermally grown SiO_x layers have been used for passivation over both FZ and Cz lifetime samples, producing excellent passivation results. In the latter stages Remote Plasma Hydrogenation Passivation (RPH) has also been incorporated to further increase the passivation of surface through H atoms. As has been explained in literature [17] hydrogen is capable of passivating the electrical activity of dangling or defective bonds. It also passivates many deep defect and impurity states in elemental and compound semiconductors besides unreconstructed surface dangling bonds and trivalent Si defects at Si-SiO₂ interfaces. More details about passivation has been explained later.

2.2.2 Charge carrier lifetime

The minority charge carrier lifetime is often represented by τ , which is the average time for which a charge carrier can live in an excited state after the electron-hole generation, before it recombines. Wafers with a high lifetime are more efficient. As the lifetime is limited by recombination, therefore, it describes the basic recombination mechanisms in semiconductor materials. Lifetime is related to the recombination rate by [18]:

$$\tau = \frac{\Delta n}{R} \quad (2.11)$$

Where, Δn is the excess minority charge carrier concentration and R is the recombination rate.

The lifetime of the minority charge carriers in the bulk of the wafer comprises the radiative lifetime τ_{rad} , Auger lifetime τ_{Aug} and SRH lifetime τ_{SRH} with the following relation:

$$\frac{1}{\tau_{\text{bulk}}} = \frac{1}{\tau_{\text{rad}}} + \frac{1}{\tau_{\text{Aug}}} + \frac{1}{\tau_{\text{SRH}}} \quad (2.12)$$

For indirect semiconductors, the radiative lifetime is substantially larger than the others and therefore usually neglected [19]. The saturation current density of a highly doped emitter (j_{0E}) can be defined by the recombination current density j_{surf} flowing to the surface, is given by [20]:

$$j_{\text{surf}} = j_{0E} \left(\frac{\Delta p}{n_i} \right)^2 \quad (2.13)$$

where n_i is the intrinsic carrier concentration and Δp is the excess number of holes.

Moreover, j_{0E} can be given by:

$$j_{0E} = S_{\text{eff}} \left(\frac{q \cdot n_i^2}{N_D + \Delta p} \right) \quad (2.14)$$

where S_{eff} is the effective surface recombination velocity, N_D is the donor carrier concentration, and q is the elementary charge.

The effective lifetime of minority charge carriers τ_{eff} is determined by the recombination at the surface of a wafer and the recombination in the bulk:

$$\frac{1}{\tau_{\text{eff}}} = \frac{1}{\tau_{\text{bulk}}} + \frac{1}{\tau_{\text{surf}}} \quad (2.15)$$

According to A.B Sproul et al [21], for symmetrical wafers with thickness W , exhibiting low but same surface recombination velocities S at both wafer surfaces the effective lifetime can be given by:

$$\frac{1}{\tau_{\text{eff}}} = \frac{1}{\tau_{\text{bulk}}} + \frac{2S}{W} \quad (2.16)$$

In high level injection (HLI), the first term of eq. 2.14 can be neglected. The surface lifetime is limited by the diffusion of charge carriers to the wafer surface in this case. Eq. 2.14 is applied in this work for the determination of j_{0E} to assess the electrical quality of co-diffused boron emitters.

2.3 Passivation

There are numerous ways that have been incorporated in order to reduce the impact of the largest contributing factors, such as by introducing a back surface field (BSF) or by growing dielectric or insulating layers (such as SiN_x , Al_2O_3 , SiO_x , etc.) over the rear surface. It has been due to the introduction of these passivating layers that the efficiency of solar cells has risen above 20%. The application of thermally grown oxide on Silicon in various forms has led to the development of various architectures of solar cells, such as PESC (Passivated Emitter Solar Cell), PERC

(Passivated Emitter Rear Contact), PERT (Passivated Emitter Rear Contact) and IBC (Interdigitated Back Contact), etc. For PERC/PERT cells, dielectric surface passivation layers are plasma-enhanced chemical vapor deposition (PECVD)-generated SiN_x and PECVD (ALD) Al_2O_3 , whereas thermally grown SiO_x usually finds its place in case of poly-Si (Polycrystalline Silicon) based passivating contacts. The latter offers low minority carrier recombination and efficient majority carrier transport, more so with an additional layer of ultra-thin SiO_x as an additional passivation layer between the poly-Si and the crystalline silicon (c-Si), promising higher V_{oc} as has been reported in literature. [22] Another approach that has been used in order to increase the efficiency of the cell and its V_{oc} is using the tunnel oxide passivated contact (TOPCon) consisting of an ultra-thin tunnel oxide and an amorphous (a-Si) or polycrystalline Silicon (poly-Si) as an electron selective contact. This approach has enabled a V_{oc} as high as 720mV and a contact resistivity below $10\text{m}\Omega/\text{cm}^2$ [22]. TOPCon concept has been used in the lifetime samples used in this thesis.

Front surface passivation

Most conventional contacts utilize only front surface passivation, applied in-between the front contact points and establishing a direct metal-semiconductor contact. A simple design of using a thin SiO_2 layer enabled an improvement of the open-circuit voltage from 590 mV (in cells without oxide) to 620 mV. An optimization of the design led to the formation of ‘Passivated Emitter Solar Cells’ (PESC) with V_{oc} improved to 650 mV owing to the feature of contact openings in the front oxide, smaller than the contact finger. This feature reduces the metal-semiconductor recombination. Another development in the architecture was the introduction of micro-grooving, i.e, texturing the surface, as shown in Figure 2.10. PESC was the first solar cell type to attain efficiency above 20%.

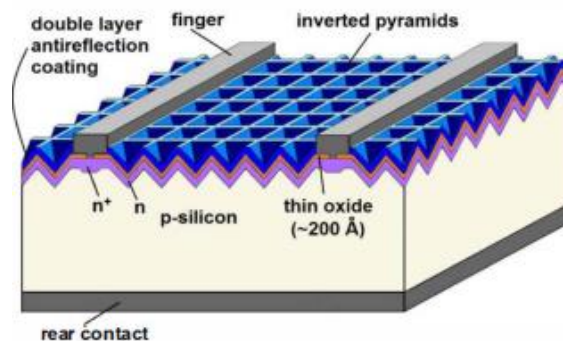


Figure 2.10: Micro-grooved PESC [23].

Front and rear surface passivation

Traditionally, recombination was reduced by using a back surface field, a high-low junction, which decreases the number of minority carriers at the rear surface of the cell and thus reduces recombination by changing the carrier statistics. However, it doesn't involve the surface defect

density. Therefore, an improvised design which focused on utilizing the features of PESC, further reducing the local contacts at the rear end to a minimum and passivating the rest of the rear surface with SiO_2 was developed, which came to be known as PERC (Passivated Emitter Rear Contact), as shown in Figure 2.11. It increased the efficiency to 22%, the improvements in both V_{oc} and I_{sc} being attributed to the reduction of the recombination density. Moreover, the rear oxide which acted as a mirror, resulted in total reflection of the light, improving light-trapping efficiency as well. The carrier separation takes place at the rear side at relatively small, point-like diffused regions. Thus, most of the photo-generated carriers have to diffuse from the front to the rear, therefore the front surface passivation is of even greater importance compared to other cell architectures

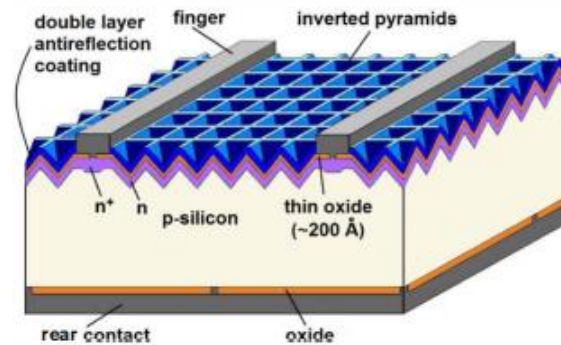


Figure 2.11: Structure of PERC cell [23].

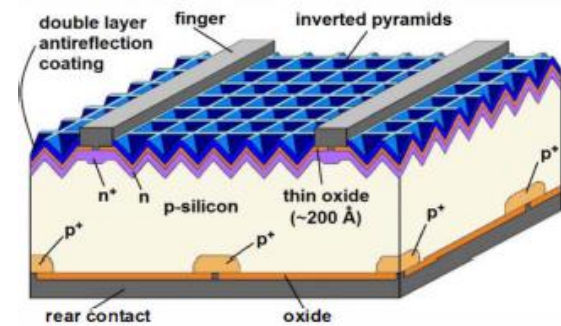


Figure 2.12: Structure of IBC solar cell [23].

For IBC (Interdigitated Back Contact) structure, shown in Figure 2.12, efficiency further improved to 22.3%. This architecture involves efficient passivation of both surfaces. Utilizing similar architectural approach solar cell featuring a boron-doped p^+ emitter was developed at Fraunhofer ISE achieving record efficiency of 25.8% [24].

Poly-Si/ SiO_x passivating contacts generated in TOPCon structures, not only enable an excellent surface passivation but also an improvement of bulk properties [25]. Results regarding the performance of Selective TOPCon, used in this thesis are explained in Chapter 4. Development of TOPCon solar cells is explained in Chapter 3.

2.4 Rheology

Given the complexity of polymer molecules, the theories are astonishingly simple...

~Masao Doi (1986)

The ability of rheological measurements to solve material characterization and processing problems has been the driving force behind the research conducted in the field of rheology. Application of rheology is broadly found in three areas: characterization, processing and design.

Rheology establishes relation between two seemingly unrelated fields of mechanics: flow and plasticity. The flow of polymers can be categorized into: shear and extensional flow. Extensional flow demands elastic character of the fluid for it to sustain normal (tension) forces and governs droplet formation. However, obtaining a controlled extensional flow in a purely viscous material is quite complex.

The basic understanding of rheological properties lies in the constitutive relations exhibited by the material subject to peculiar conditions such as constant or dynamic shear stress or strain, etc. The simplest constitutive relation that explains the flow of liquids is the *Newton's law of viscosity*, which states that the shear stress generated in the material is proportional to the rate of straining;

$$\tau = \eta \dot{\gamma} \quad (2.17)$$

where,

$\dot{\gamma}$ [s^{-1}] (= $d\gamma/dt$) is the rate of straining,

τ [Pa] is the shear stress generated in the fluid,

η [Pa.s], the (stationary) Newtonian viscosity, is the constant of proportionality,

γ , the shear strain describes the displacement gradient that exists between the two plates as explained through parallel plate model, in Figure 2.13.

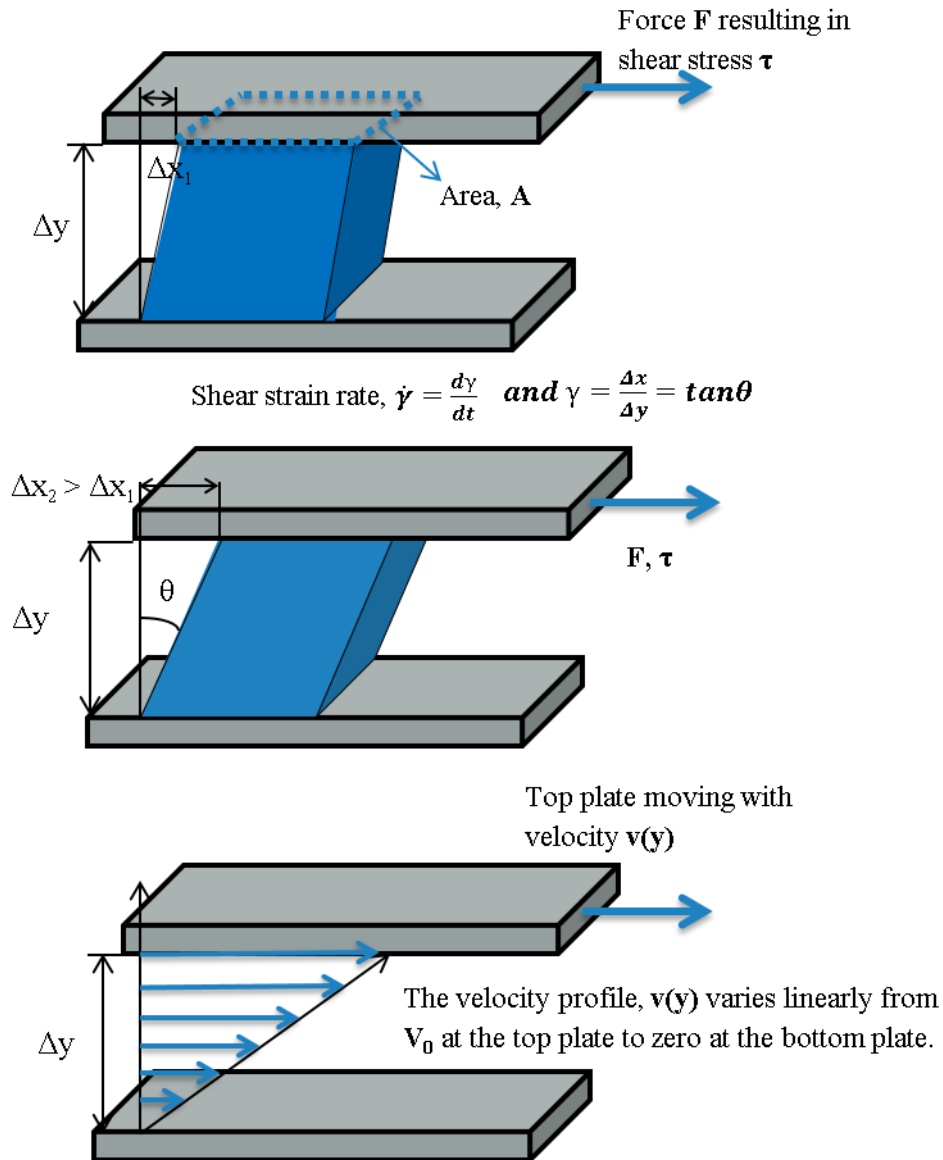


Figure 2.13: Parallel plate model

Rheological properties of materials often show dependence on shear strain or strain rate (non-linear behavior) and sometimes on the time of deformation (non-equilibrium behavior). The typical reaction of a material to stress or strain determines its properties and consists partly of its elastic nature and partly of viscous nature, thus making it a viscoelastic [26]. The speed of deformation determines the extent to which both the natures are exhibited. There are numerous rheological quantities which characterize the rheological behavior e.g. *Shear modulus*, G [Nm^{-2}]

for an ideal elastic material under shearing forces (*Young's modulus*, E [Nm^{-2}] under uniaxial tension or compression) (the relation of G with shear stress and strain is given by equation 2.18)

$$\tau = G\gamma \quad (2.18)$$

and *Shear viscosity*, η [Nm^{-2}s] for an ideally viscous fluid, as described by Newton's law, in equation 2.17.

Figure 2.14 provides a graphical overview of different relationships between stress and strain rate for fluid and fluid like materials subjected to a shearing deformation at a given rate. Specific response of a material puts it under a specific category, as is shown in the figure. When the relation between shear stress, τ , and shear rate $\dot{\gamma}$ is linear, the fluid is defined as *Newtonian* and exhibits constant viscosity under shear deformation. This is represented by straight line in the figure. All other curves fall under *non-Newtonian* category and exhibit stress dependence of viscosity.

Non-Newtonian fluids are categorized as:

- Shear thickening – viscosity increases with shear strain rate
- Shear thinning – viscosity decreases with shear strain rate
- Bingham fluids – solids at low stresses but flow as a viscous fluid at high stresses
- Thixotropic – viscosity reduces with time on application of stress
- Rheopectic (dilatant) – viscosity increases with time on application of stress

Behavior of polymer solutions can be Newtonian or non-Newtonian depending on their structure, concentration, molecular weight and solvents present in them besides the temperature to which they are subjected. However, polymer melts typically show non-Newtonian behavior.

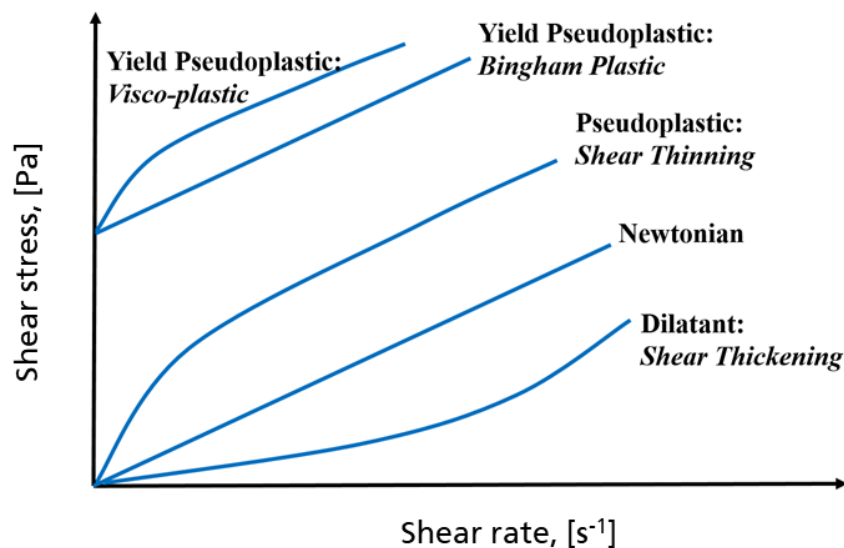


Figure 2.14: Flow curves [27]

For non-Newtonian fluids the viscosity obtained, which shows dependence on shear rate, is known as apparent viscosity ($\eta_{\text{app}} = f(\dot{\gamma})$). Polymer solutions, which exhibit a shear-thinning nature, obey power law, which is quantified empirically as,

$$\tau = k(\dot{\gamma})^n \quad (2.19)$$

where, k representing the consistency index, is the measure of η_{app} for $\dot{\gamma} = 1 \text{ s}^{-1}$. $n = 1$ for Newtonian fluids, $n < 1$ for shear thinning and $n > 1$ for shear thickening, n being the power law index. For practical purposes, both are constant over a limited range of frequency. At low shear rates, owing to the restorative effects of Brownian movements and particle/molecular interaction, materials tend to maintain irregular order with a high zero shear viscosity (η_0). A high shear viscosity can result in network formation through entanglements, which must be broken to enable flow of the material. As the shear rates or stresses become high enough to overcome these effects, aggregates can be broken down and polymers stretch out and align in the direction of flow. As a result of such rearrangements there is a decrease in molecular interactions and an increase in the free space between dispersed components of the solution, which thus results in significant reduction of viscosity. The maximum attainable viscosity (equilibrium viscosity, η_∞) is a result of the maximum achievable degree of orientation. It is influenced largely by the solvents available and the related hydrodynamic forces influence it [28].

Various materials like clay mold, toothpaste and mayonnaise exhibit solid behavior under small stresses until a threshold of stress (yield stress) is attained, above which they behave as fluids. Such fluids fall under the category of Bingham fluids. Their viscosity is referred to as Bingham viscosity (η_B) and their flow can be empirically expressed as,

$$\begin{aligned} \tau &= \tau_y + \eta_B(\dot{\gamma}), \text{ or} \\ \tau &= \tau_y + k(\dot{\gamma})^n, \end{aligned} \quad (2.20)$$

where, τ_y is the yield stress. As can be anticipated, Bingham behavior can be observed at stresses above the yield stress, which makes it usable for engineering applications and calculations.

For further understanding on classification of fluids, one can refer to sources elsewhere [26].

2.4.1 Dynamics of rheology: Role of time scale

An ideal situation would be when all the fluids would behave as they do under constant shear stress and strain. In such cases, the behavior of the material could well be anticipated under higher or lower values of stress, only by extrapolating the already known values. However, in service conditions, one seldom finds constant values of forces and strains. Therefore, to understand the role of change of stress, or in other words the role of *time scale* (the time for which a stress with certain magnitude and direction is applied) on the material behavior becomes imperative. Time scale of interesting phenomena is often different from those available in fluid characterization. The two can be equal only in ideal cases e.g. steady state compression of an

ideally elastic fluid. Timescale behavior originates from the structure of the particular material. Elastic materials tend to store the energy of deformation (usually dissipated as heat) and release it as the applied stress is removed. This would imply that no change was induced on the molecular level, particularly referring to the breakage of bonds in the material. In such materials, timescale doesn't play as significant a role, since the structural elements stay unchanged over the time scale. Contrarily, viscoelastic materials which flow on application of force, due to their inherent minimal resistance, are therefore not able to release the energy back. The energy is lost in spontaneous (stress free) breakage and re-formation of bonds in the material and is referred to as '*Dissipation Energy*'. The time scale of this phenomenon varies from seconds to days. Quantifying such effects can be done by first inducing a deformation into a material and then evaluating the stress required to keep that deformation constant. This approach is referred to as 'Stress relaxation' approach (as in case of elastic material the applied stress will start reducing until the constancy is reached). Time taken by a material to reduce its stress by 1/e factor is referred to as '*relaxation time*' τ (different from the τ used for shear stress). Visualization of such effects can be done through several models such as the famous Maxwell's model, explained later.

2.4.2 Rheology of polymer solutions

Zero shear viscosity for diluted and semi-diluted solutions

An accurate theory of intrinsic viscosity of dilute polymers is constructed using Einstein's results for dilute suspension of spheres. The formulated result relating the viscosity to the Volume of molecular sphere is expressed as,

$$(\eta - \eta_s)/\eta_s = 2.5 \Phi = 2.5 (n_2/V) V_{sph} \quad (2.21)$$

where, η_s is the viscosity of the solvent, Φ is the solute volume fraction, n_2/V is number of molecules n_2 per unit volume of solution (V), and V_{sph} is the volume of the molecular sphere. ($n_2/V = cN_{AV}/M$, where c is the concentration, M is the molecular weight, and N_{AV} is the Avogadro's number). Intrinsic viscosity of dilute solutions also depends on its molecular weight, according to Mark-Houwink relation:

$$[\eta] = (\eta - \eta_s)/(\eta_{sc}) = K M^a \quad (2.22)$$

where, the constant 'a' varies from 0.5 to 0.8 depending on polymer-solvent combinations.

Rheology of concentrated polymeric solutions, however, is quite different to the above notion owing to the different dynamics that we come across due to the polymer structure. Expansion in powers of concentration is a conventional way to account for the increase of viscosity with increasing concentration. This is quantified as,

$$\eta = \eta_s(1 + [\eta]c + k'[\eta]^2c^2 + \dots) \quad (2.23)$$

where, $k'[\eta]^2$ is known as the Huggin's constant and k' is independent of molecular weight for long chains. Its average value ranges from 0.3 to 0.4 for good solvents (which cause the polymer coil to expand due to energetically favorable interactions between polymer segments and solvent molecules). For theta solvents, which assume ideal chain nature of polymer coil, with no monomer interaction and random walk dimensions, the value for Huggin's constant ranges between 0.5 to 0.8. At low concentrations the interactions in a polymeric solution observed resemble a suspension of discrete rigid molecules. As concentration increases, so do the interactions on the neighborhood of each molecule. These interactions depend on volume occupied by the molecules determining the degree of overlap of individual molecular domains [29].

Entanglements and Zero Shear Viscosity of concentrated solutions

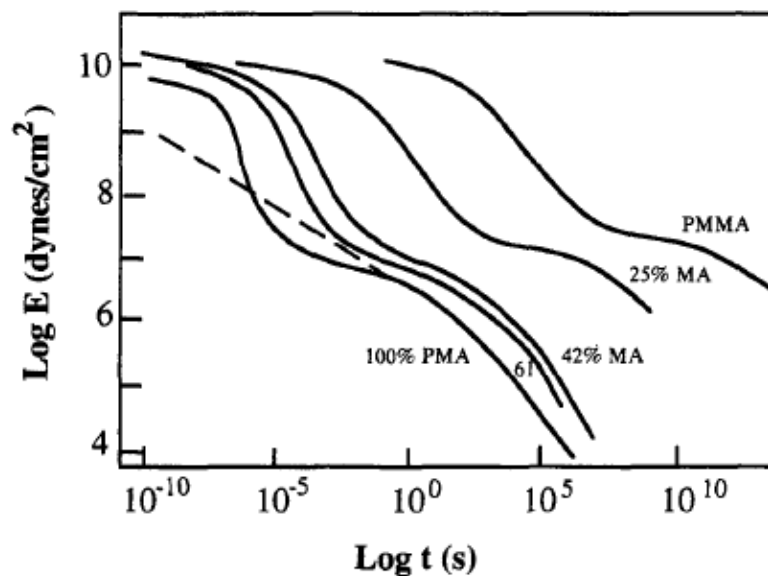


Figure 2.15: Stress relaxation modulus for methyl acrylate-methyl methacrylate copolymers. Dashed line represent a typical Rouse theory prediction. Adapted from Fujino et al. (1961) [29].

As has been established in literature, role of entanglements is evident through their impact on G' and G'' , in the form of plateaus (Figure 2.15, E being equivalent to G) or $\tan\delta$ (loss factor), in the form of additional peaks. Above a critical molecular weight and/or concentration a new relaxation appears.

Above critical molecular weight (M_c – the break point), for the formation of effective entanglement couples the slope of the viscosity - $c \cdot M_w$ curve changes from 1 to 3.4, and can be quantified as,

$$\eta_0 = K M, \quad M < M_c \quad (2.24)$$

$$\eta_0 = K M^{3.4}, \quad M > M_c \quad (2.25)$$

This change is demonstrated graphically in Figure 2.16. The number of intermolecular contacts per unit volume giving rise to the entanglements, is proportional to c^2 . It is noteworthy that the transition for different concentrations starts at almost same $c \cdot M_w$ value.

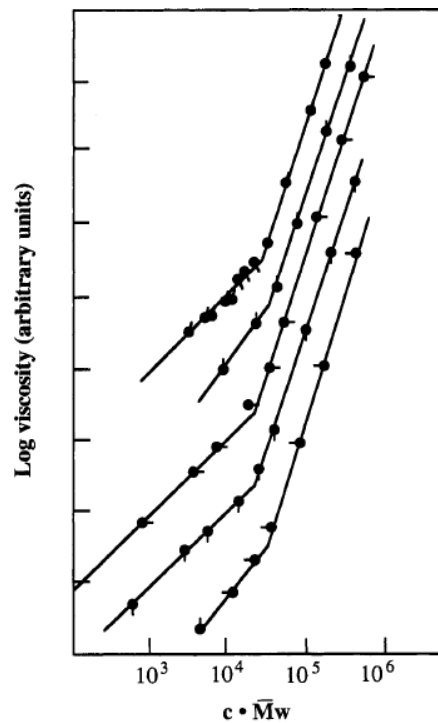


Figure 2.16: Viscosity versus the product cM , for polystyrenes at concentrations between 25 and 100%. Data at the various concentrations are shifted vertically to avoid overlap. Adapted from Graessley (1974) [29].

In steady flow, there are numerous factors that control the number of entanglements per unit volume (– the entanglement density). Material observes relative motion as the molecules, which were close enough to entangle extensively, start separating. The rate of entanglement formation of a molecule depends on its tendency to form more entanglements as it approaches more molecules. This conceptualizes entanglement formation as a kinetic process. Moreover, for any pair of chains close enough to entangle extensively, most conformations available to the two chains furnish a high entanglement density. However, as the chains get close to each other, the conformation is necessarily an improbable one as no entanglement is involved. Therefore, a

succession of diffusive rearrangements is involved for passage of a pair to high entanglement density. As the conformations become increasingly independent of the initial conformation, a more probable state with respect to entanglement density is attained, approached with equilibrium entanglement density.

The formation of entanglements is possible if the environment provides conducive factors, like thermal motion of sizable sections of the chains and at least two or three sequential movements, which are necessary to produce loops of entanglement. It is therefore understandable that initially the entanglement formation is sluggish, but it increases rapidly towards the equilibrium entanglement density. During steady flow of the polymer, the entanglement density between any two molecules depends on the characteristic time necessary for entanglement formation compared to the “contact” time between the two molecules.

In a shear field, two molecules tend to approach each other and for an entanglement to exist,

- a) Two molecules must be within a certain distance to each other and
- b) They must remain within that distance for a finite time.

As a result, as shear rate gets extremely high, the entanglement density gets reduced because fewer molecules remain in the “entanglement sphere” for a sufficiently long time. Such behavior of polymers is capable of explaining ‘non-linear’ rheological properties to a certain extent, beyond which the ‘Reptation Model’, which will be described later, provides quantitative explanation [29].

Effect of Branching

Due to the anchoring ability of long chains, the reptation mechanism is not possible for highly branched molecules, which need to pull out all their branches for relaxation, as depicted in Figure 2.17. Such movements results in a much slower motion than reptation. Individual arms cannot reptate and instead, they relax by retracting from the tubes created by entanglements with surrounding polymers. Branched polymers with smaller branches have a lower zero shear viscosity than linear molecules of the same total molecular weight and for the case of larger branches, the branch chain viscosities overtake those of equally massive linear chains.

Effect of Molecular Weight Distribution

Determining zero shear viscosity of monodisperse polymers might be problematic as they exhibit a sharp onset of shear rate dependence of viscosity, which gets more diffuse as the molecular weight distribution broadens.

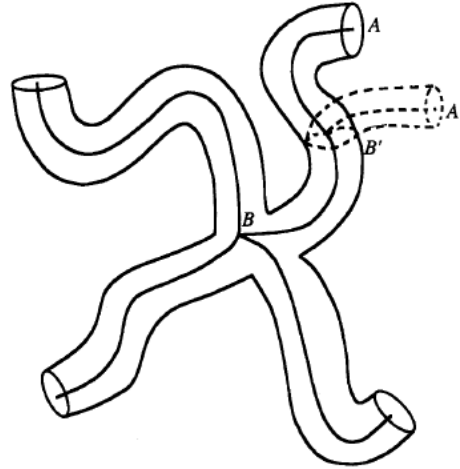


Figure 2.17: Star polymer relaxation process[29].

2.4.3 Temperature Dependence

Temperature plays a strong role in determining structural properties of a polymer, which in turn determine its flow. Like other liquids, viscosity of a synthetic polymer reduces with temperature exhibiting a complex dependence. Sufficiently above the glass transition temperature (T_g), viscosity follows the Arrhenius relation,

$$\eta = \eta_{\infty} \exp \left[\frac{E_{\eta}}{RT} \right] \quad (2.26)$$

where, E_{η} , is the activation energy for viscous flow.

For melts of glassy polymers in the region of T_g to T_g+100 , Williams-Landel-Ferry (WLF) equation describes the temperature dependence more appropriately as follows,

$$\log \left[\frac{\eta}{\eta_r} \frac{T_r \rho_r}{T \rho} \right] = \frac{-C_1(T-T_r)}{C_2+T-T_r} = \log a_T \quad (2.27)$$

where, subscript 'r' refers to reference condition (usually the glass transition temperature). C_1 and C_2 are constants. WLF equation is based on free volume concept and is the basis of Time-temperature superposition, which however does not apply to the inkjet polymer inks.

2.4.4 Aging of polymers

All polymers are susceptible to aging when exposed to environmental conditions, such as light, humidity, presence of oxygen, heat, etc. More severe the environmental conditions, more pronounced will be the effect of aging. Aging mechanism can be physical or chemical depending on the factor that induces aging and the response of the polymer to that change. Aging, which can be defined as '*the effect of time on the intrinsic properties of the material*', often leads to

degradation of the material, which can be physical or chemical, again, depending on the mechanism and aging factor. Most of the physical degradation factors inducing aging phenomena can be reversed and only involve structural changes. However, such structural changes also have a detrimental impact on the behavior of the polymer, especially its mechanical behavior. Physical degradation, which in case of glassy polymers, can be induced through interactions with liquids or environmental stress crazing. For dispersed polymer solutions aging can also cause agglomeration of molecules, as has been demonstrated in literature, depicted in Figure 2.18 [30]. Often such changes can be reverted by simply reversing the environment to initial conditions, or by thermal treatment of glassy polymers, provided dimensional stability is maintained. However, thermal treatment does not remain an option for polymer solution inks considering high probability of detrimental impact high temperature can have on the inks. One common effect on thermoplastic and cross-linked polymers due to interaction with liquids is the increase in the free volume due to disentanglement of the chains and consequent transformation of a complex structure into a simple one. This can lead to induction of shear thinning behavior in liquids, to reduction of the glass transition temperature (T_g), to lowering the yield stress and to the increase in the overall volume of the polymer. Sorption of water (whether in the form of sea-water, portable water or humidity) is a very common liquid-interaction based physical degradation of polymers. Another common mechanism of physical aging pertains to the thermal history of the polymer and occurs due to the tendency of the polymer to attain structural stability and reach the equilibrium volume. Physical aging can be recovered by thermal treatment.

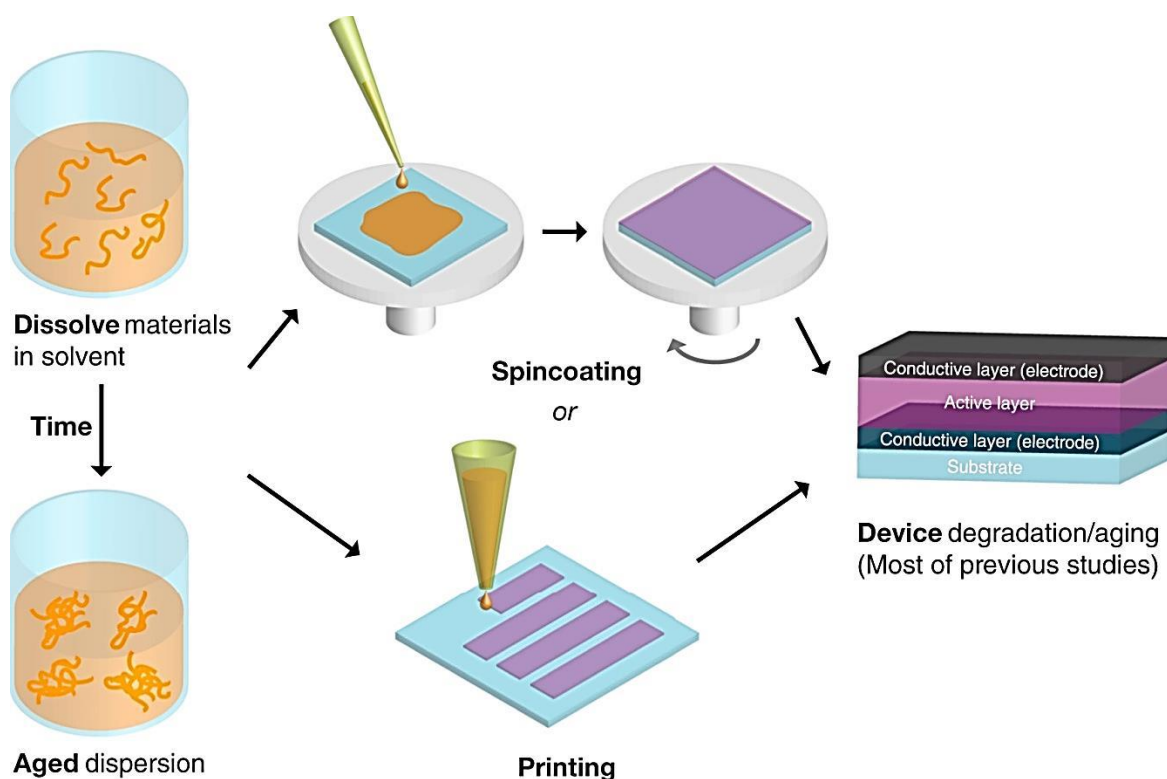


Figure 2.18: Schematic of solution process and dispersion degradation/aging [30].

Chemical degradation

Chemical degradation is irreversible in nature and is caused by four major factors:

- a) High temperatures
- b) Oxidation
- c) Interaction with liquids
- d) High energy radiations/photolytic degradation

Temperature increase above a certain limit induces chemical changes in the polymer owing to the energy increase and the subsequent tendency of the intramolecular bonds' scission. Temperature effect is associated with specific reaction mechanisms (de-polymerization and elimination). However, at ambient temperatures this effect is not very effective and can be neglected.

Oxidative reactions, especially thermo- and photo-oxidative degradations are the most common forms of chemical degradation. A trace amount of oxygen or ozone atom or a radical can initiate a reaction sequence leading to polymer degradation resulting in formation of oxygenated functional groups in the polymer backbone, chain scission leading to lower chain size and occasional cross-linking and emission of small molecules. The presence of metallic elements in the polymer accelerates oxidative degeneration due to catalytic reaction caused by homolysis of hydro-peroxide molecules into reactive radicals. Oxidative degeneration is further enhanced due to the presence of UV radiation.

Hydrolysis is another common source of chemical degradation. When hydrolysis-sensitive bonds are part of the polymer backbone chain, hydrolysis will result in de-polymerization and release the hydrolyzed monomers from the polymer. When functional groups are attached to sides of the backbone chain, the polymer remains intact but small molecules are released. Some hydrolyses require acid or base catalysis and often these catalysts can be supplied by external agents, such as atmospheric SO_3 , or oxidation products of the polymer [31].

2.4.5 Model fitting

Maxwells model

Materials with more than one phase, such as solid particles dispersed in a liquid are known as structured fluids. Their rheological behavior depends on interactions of the constituents. Such fluids, which include but are not limited to, polymer solutions, have a minimum equilibrium energy associated with them in the absence of an external stimulus, attributable to the entanglements between chains of polymer solution. On application of an external stress, the equilibrium is shifted, generating an elastic force, which tries to bring the system back to its equilibrium and to restore the microstructural state. This is analogous to a stretched spring obeying Hooke's law. The spring thus represents a linear elastic body in which the applied stress

is proportional to the resultant strain up to its elastic limit and which returns to its initial state on removal of stress as shown in Figure 2.19. As the elastic limit is exceeded, the deformation becomes permanent. Same principles apply in case of simple shear deformation of polymer solutions. Following the analogy of Hooke's law, herein the constant of proportionality is the elastic modulus (G'), which is a measure of resistance to deformation or stiffness. Since a purely elastic material does not show time dependence, strain appears and disappears at the same instant of application and removal of stress, respectively.

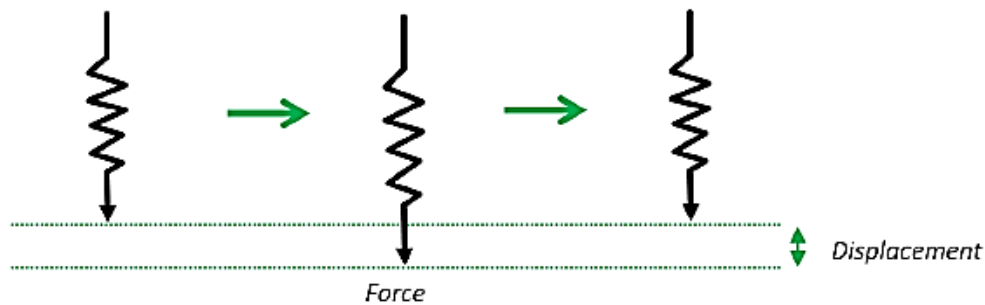


Figure 2.19: The response of an ideal solid (spring) to the application and subsequent removal of a strain inducing force [28].

The energy stored in the spring element can be stored in three possible ways:

- by bond deformation (stretching and bending)
- by twist around the bonds against the hindering potential, which interferes with free rotation
- by decrease in entropy when the extension restricts the chain to less probable configurations,

the last two being mutually exclusive.

Similarly, for viscous behavior we have an analogy of a dashpot obeying Newton's law. A dashpot is a mechanical device consisting of a plunger moving through a viscous Newtonian fluid. On application of stress, the deformation of the dashpot begins instantaneously and goes on at a constant rate, known as the strain rate, until stress is removed. The strain is permanent as the energy of deformation is dissipated (as heat) within the fluid and hence cannot be restored back. A schematic is shown in Figure 2.20.

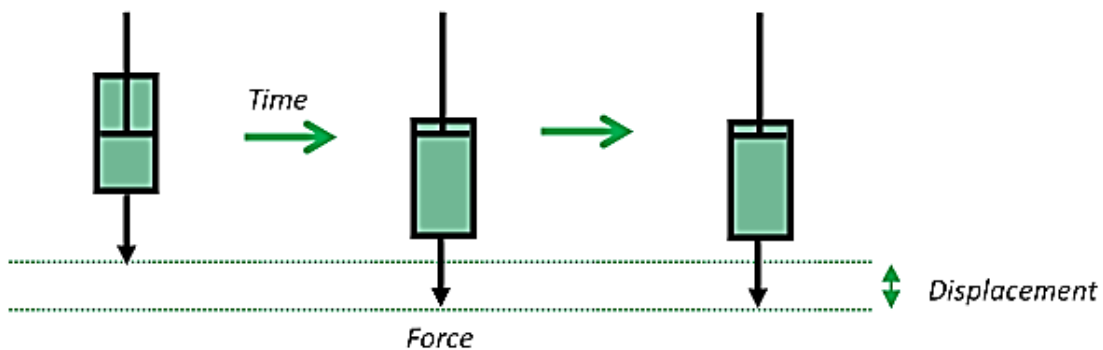


Figure 2.20: Response of an ideal liquid (dashpot) to the application and subsequent removal of a strain inducing force [28].

The polymer solutions utilized for inkjet printing fall in neither of the categories and rather lie in between the region of elastic solids and viscous liquids, thus forming the category of ‘Visco-elastic’ materials. Therefore, to represent their behavior, we combine springs and dashpots, connected in series and parallel, generating various models such as Maxwell’s model, Maxwell’s retarded model, Kevin-Voigt’s model, Zener’s model, Burger’s model, etc.

The simplest of the before mentioned models is the Maxwell model, which is a two-element model consisting of a linear spring element and a linear viscous dashpot element connected in series, as shown in Figure 2.21.

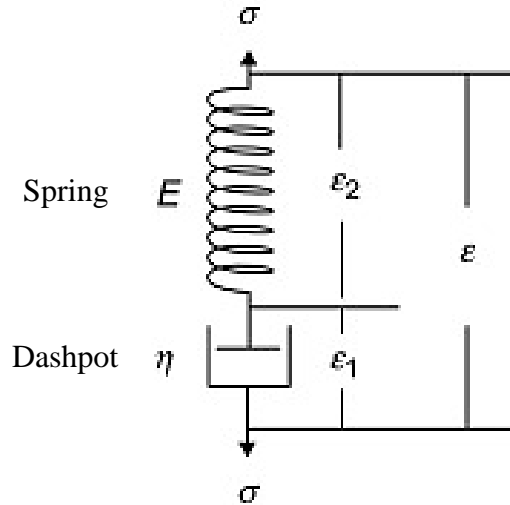


Figure 2.21: The Maxwell model [32].

The stress-strain relations of spring and dashpot respectively are:

$$\sigma = E \cdot \epsilon_2 \tag{2.28}$$

$$\sigma = \eta \left(\frac{d\epsilon}{dt} \right) \tag{2.29}$$

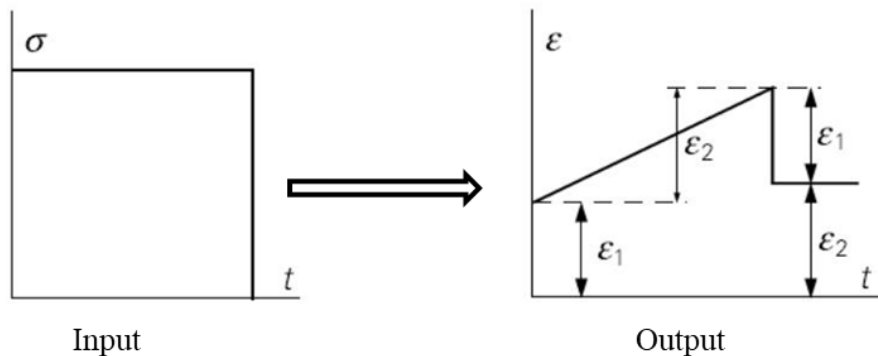


Figure 2.22: Stress-strain correlations according to Maxwell’s model [33].

The total output in Maxwell model is given by:

$$\varepsilon = \varepsilon_1 + \varepsilon_2 = \sigma/E + (\sigma/\eta)t = \sigma [1/E + t/\eta] \quad (2.30)$$

Thus the initial strain at time, $t = 0$ s, will be given by the purely elastic part.

The characteristics of a Maxwell fluid follow the classical form of the single mode Maxwell equations as given below:

$$\begin{aligned} G'' &= \eta_s \omega + \frac{g\omega\tau}{1+(\omega\tau)^2} \approx \omega (\eta_s + g\tau), \quad (\text{for small } \omega) \\ G' &= \frac{g(\omega\tau)^2}{1+(\omega\tau)^2} \approx g(\omega\tau)^2, \\ \eta^* &= \frac{\sqrt{G'^2 + G''^2}}{\omega} \end{aligned} \quad (2.31)$$

where, η_s is the solvent viscosity, 'g' is the elastic modulus of the Maxwell element, and τ is the relaxation time of the Maxwell element ($\tau = \eta/g$). Consistent with the equations, the low frequency limit of a single mode Maxwell fluid should give the slope of $\log(G''(\log(\omega)))$ curve close to 1 and the $\log(G'(\log(\omega)))$ curve close to 2 [34]. As has been observed, ideal inkjet printing fluids follow Maxwell's model, however, that does not limit the printability to Maxwell fluids only.

Maxwells retarded model

The rheological response of a fluid, besides its primary structure and intrinsic properties, is equally determined by the secondary interactions, called entanglements. Entanglements, which are stochastic in nature result in a transient network structure produced by association of the long chains along part of their lengths. Due to these entanglements, a fluid behaves like a solid in response to sudden short periods of stress, as there is not enough time left for the molecules to move out of each other's way [35]. The concentration of the polymer plays a very important role in determining the number of entanglements, higher concentration implying more entanglements. Therefore, the presence of solvent particles, additives, dopants or any other material, which tends to break the polymer chains and restrict their secondary interactions can bring down the effect of entanglements to a great extent.

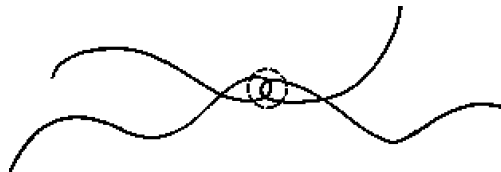


Figure 2.23: Point of entanglement [35].

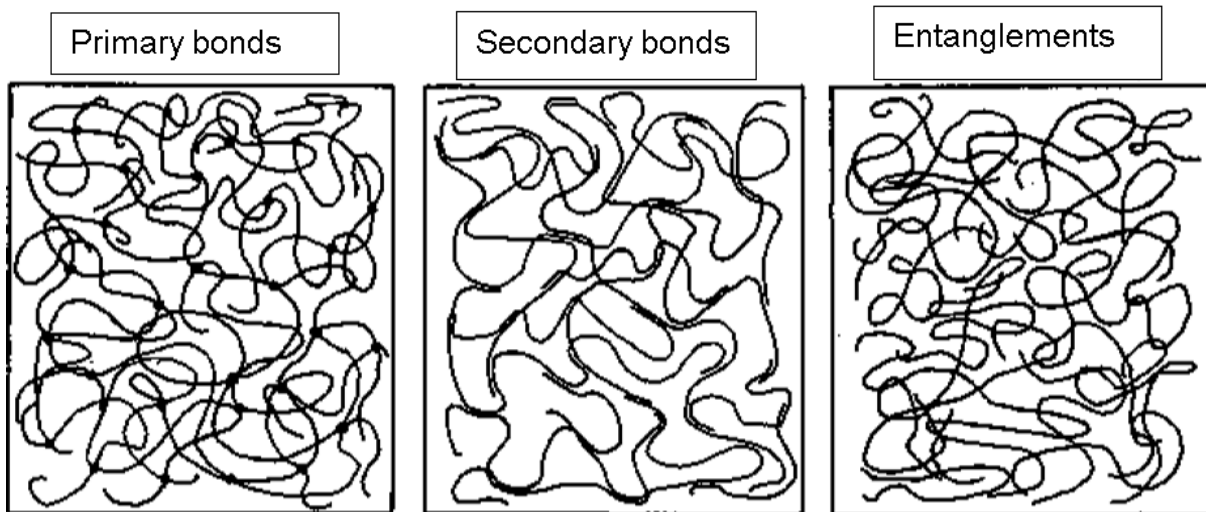


Figure 2.24: Schematic presentation of types of networks in concentrated polymer solutions involving primary bonds, secondary bonds, and entanglements [35].

The simplest model for representing a concentrated polymer solution with strong role of entanglements is through Maxwell's retarded model. This is different from the Maxwell's model, given that it has two dashpots, one in parallel (representing polymer viscosity) with a spring, which delays the response of the spring and the other in series (representing solvent viscosity) with the assembly of other two, which allows relaxation, as shown in the following Figure:

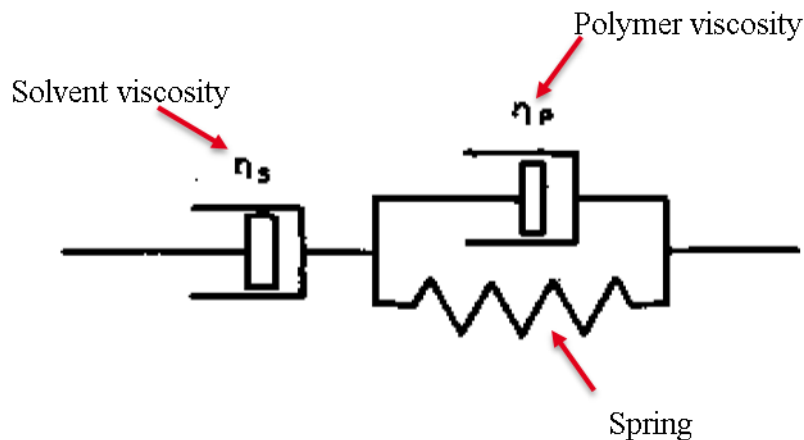


Figure 2.25: Maxwell's Retarded Model [35].

The energy storage mechanism is the same as explained under Maxwell's model, while the role of the parallel dashpot element is the provision of frictional resistance to rearrangement of chain segments involved in extending the spring, due to both the viscosity of the solvent and the interference of neighboring chains.

The dashpot in series permits stress relaxation by three processes:

- a) rotation around bonds into new positions of minimum potential energy,
- b) slippage of strand ends by disentanglement and
- c) chemical decomposition resulting in breakage of strands,

the last being negligibly effective due to its slow progress, compared to the time of experiment.

For the retarded Maxwell's model, the frequency dependence of G' , η' , and $|G|$, is given by the following set of equations:

$$\begin{aligned}
 G' &= G\omega^2\tau_s^2/[1+\omega^2(\tau_s+\tau_p)^2] \\
 \eta' &= \eta_s[1+\omega^2\tau_p(\tau_s+\tau_p)]/[1+\omega^2(\tau_s+\tau_p)^2] \\
 |G| &= G\omega\tau_s(1+\omega^2\tau_p^2)^{1/2}/[1+\omega^2(\tau_s+\tau_p)^2]^{1/2}
 \end{aligned}
 \tag{2.32}$$

where, ω is 2π times the frequency, and the characteristic time constants τ_s and τ_p are defined as η_s/G and η_p/G , respectively, where η_s and η_p are the series and parallel viscosities.

Reptation model

Reptation model draws the analogy of macromolecular motion in concentrated polymers to that of a snake moving in a contorted "tunnel" formed by surrounding polymer molecules. The main idea that lies behind it is the possibility of movement of a monomer fluid in one direction on application of stress or due to Brownian motion. In this model, the probability P of finding a segment at some position s (measured along the chain axis) at time t , satisfies the simple, one-dimensional diffusion equation:

$$\frac{\partial P}{\partial t} = D_0 \frac{\partial^2 P}{\partial s^2}
 \tag{2.33}$$

with the boundary conditions

$$P(s, 0) = \delta(0)$$

$$P(s, t) = 0 \text{ as } s \rightarrow \pm\infty$$

with δ being the delta function (i.e. first segment is at the origin), and D_0 is the diffusion coefficient for the motion along the chain.

The concept is explained in Figure 2.26. A given polymer chain C entangled with other chains C_1 - C_4 (top) may be regarded as enclosed within a virtual pipe bottom, defined by the locus of the constraints imposed on its motion by the other chains. ξ is the mean permitted displacement of a segment of C in a direction normal to the “pipe axis.” The symbols in the middle figure represent cross sections through C_1 - C_4 in a plane parallel to the paper. Since each of the chains C , - C_4 may itself be regarded as being in a similar pipe, the mean separation of the cross sections is also ξ .

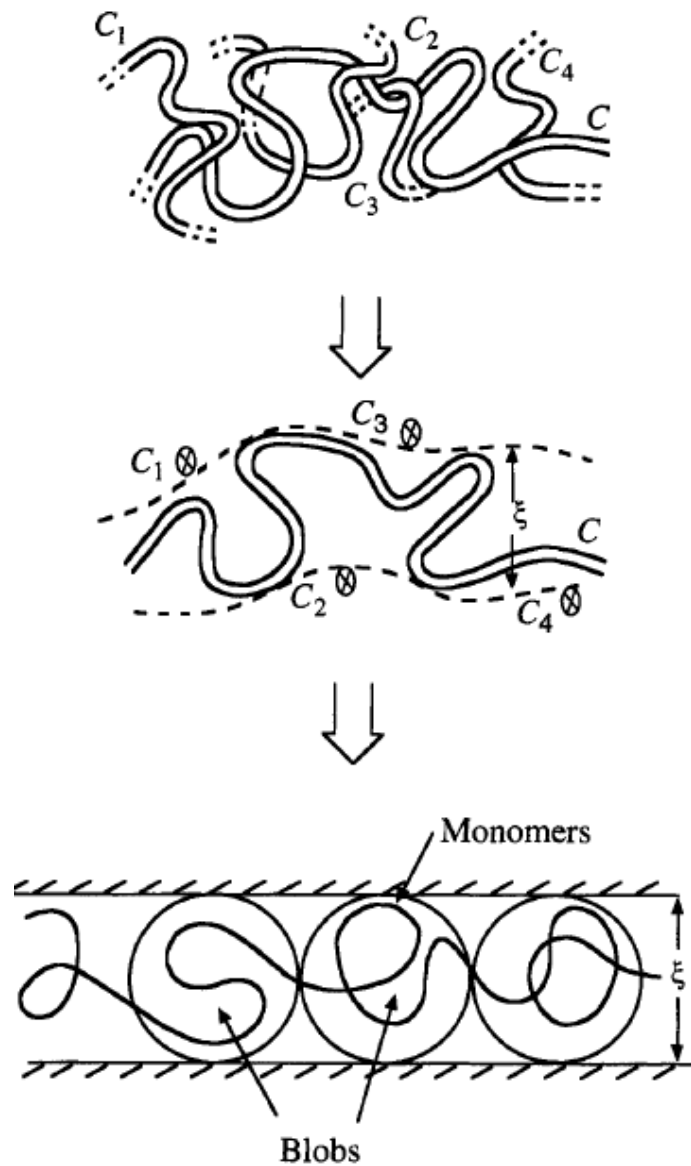


Figure 2.26: The idea of reptation in polymer solutions (taken from articles by Klein, 1978, and de Gennes, 1979). [29].

2.5 Inkjet Printing Technology

The printing industry has changed drastically with the growth of digital printing technologies particularly inkjet-printing, which offers the flexibility of adjusting or changing the software implementation for defined patterns according to user requirements. Besides the traditional application in graphics sector, inkjet-printing has been widely investigated in recent years as a valuable tool in others fields such as printed electronics and photovoltaic (PV) industry due to the following advantages [36]:

- Non-contact printing which is crucial for mechanically sensitive substrates
- Additive patterning and maskless approach
- Low cost
- Scalability to large area manufacturing
- Efficient material utilization
- Precise control of the deposited ink volume

However, there are some disadvantages associated with inkjet technology at industrial as well as research level:

- Interaction between the ink and the substrate is critical
- Ink viscosity limitation (should be below 20 mPa.s)
- Nozzle clogging

2.5.1 Inkjet mechanism

In general, Inkjet systems fall under two categories, continuous inkjet (CIJ) and drop-on-demand (DOD) inkjet, with variants within each category as shown in Figure 2.27.

2.5.1.1 Continuous Inkjet (CIJ) Technology

In CIJ, a continuous stream of droplets is ejected from the nozzles (Figure 2.27 (a)). The droplets are formed by a piezo crystal that produces high frequency vibrations (in the range of roughly 50 kHz to 175 kHz). As the drops fall, they are subjected to an electrostatic field, which induces a charge on their surface. The charged drops then pass through a deflector plate, which determines the landing positions of drops [37].

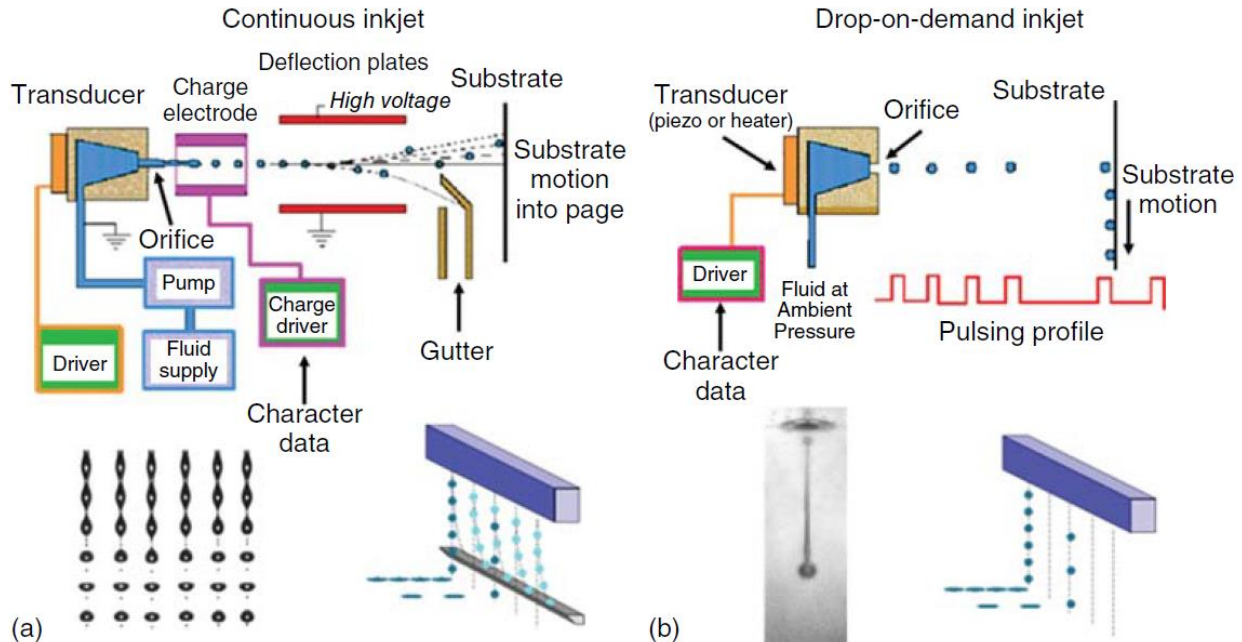


Figure 2.27: Inkjet printing systems: (a) continuous inkjet and (b) drop-on-demand inkjet [38].

2.5.1.2 Drop-on-Demand (DOD) Inkjet Technology

In DOD inkjet technology, drops are generated as needed (on demand) to form a desired pattern. The mechanism for generating droplets is by applying pressure pulses inside the ink chamber, which is connected to a nozzle as shown in Figure 2.27 (b).

Based on the mechanism used for droplet ejection, there are two subcategories for DOD print-heads: piezo DOD and thermal DOD. In thermal DOD print-head, the pressure needed to eject a droplet is provided by heating a resistive element in a small chamber containing the ink. This technology is mostly used in consumer desktop printers. In Piezo DOD print-head, a piezoelectric transducer is used, which produces a pressure pulse on application of a voltage signal, required to eject droplets [38].

Although the manufacturing of piezo DOD print-head is more complicated and costly as it requires a piezo material, it is favorable for material deposition purposes, because of following reasons [39]:

- Precise and variable droplet size through selection of different waveforms
- Wide range of inks due to its low temperature operation (e.g. solvent, UV, pigment, dye)
- Droplet sizes in the range of picolitres
- Long-standing application due to lower temperature

In the light of these considerations, piezo DOD inkjet printer ‘PiXDRO LP50’ by Meyer Burger Technology AG is used for this thesis. In addition, the disposable Fujifilm Dimatix

Cartridge (DMC) consisting of 16 nozzles with a drop size of 10 pl is used for high-resolution, non-contact jetting of functional fluids.

In a piezoelectric inkjet device, a piezoelectric material e.g. lead zirconate titanate (PZT) ceramic is used as an actuator to produce the force necessary to eject a droplet. The effect of applying voltage to a piezoelectric material is that the crystal deforms. The deformation is used to develop force to squeeze the ink chamber for droplet ejection. Based on the piezo transducer (electrode) deformation mode, DOD printheads can be categorized into four main types as shown in Figure. 2.28: squeeze, bend, push, and shear.

In squeeze mode, a radially polarized piezo transducer surrounds the ink chamber and squeezes it when voltage is applied. In shear mode, the applied voltage is perpendicular to the direction of polarization of the piezo transducer. By contrary, the applied voltage is parallel to the polarization of the piezo transducer in both bend and push modes.

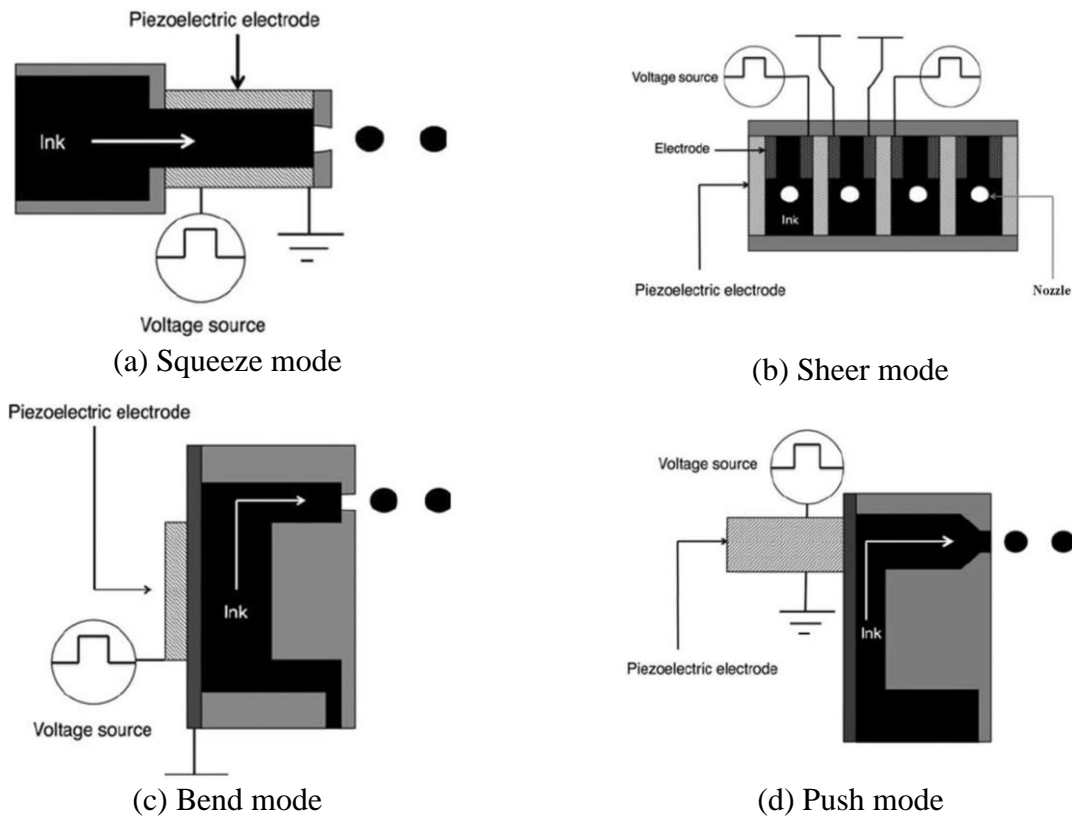


Figure 2.28: Four categories of piezo DOD print-head designs, (a) squeeze mode, (b) shear mode, (c) bend mode, (d) push mode [40].

Inkjet process development

In order to develop a new inkjet process, it is crucial to consider the following aspects of an inkjet system: (1) print-head, (2) ink requirements, and (3) droplet behavior on substrate. These factors are interconnected and have a huge impact on the viability of inkjet process.

2.5.1.3 Print-head

The inkjet printer used in this work consists of cartridge-based print-head, substrate alignment and print inspection and vision systems for drop inspection as shown in Figure 2.40. The other features of PiXDRO LP50 printer, which are important for this thesis are:

- Substrate chuck heating
- Ink tank heating
- Glovebox integration for inert environment

The DMC print-head module enables cost-efficient process development, since it allows the use of said disposable cartridges with 1pL and 10 pL droplet volume.

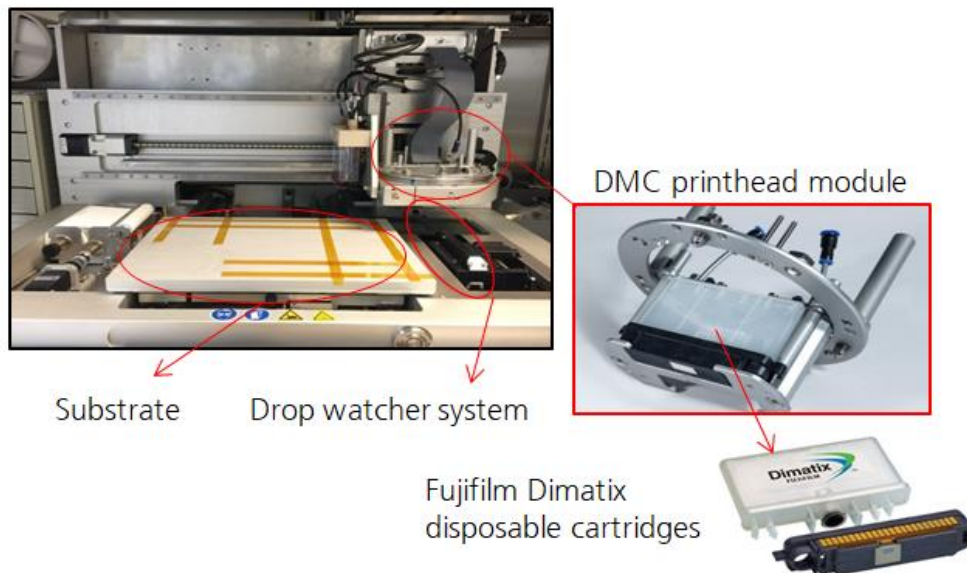


Figure 2.29: PiXDRO LP50 inkjet printer (Meyer Burger Technology AG) with different parts.

The DMC print-head module operates in bend mode, where the applied voltage bends the piezo transducer to push the fluid along the ink chamber and ejects it out of the nozzles (Figure 2.28 (c)). Besides fluid properties, the driving pulse of the printhead module also plays an important role in determining the jetting quality. It consists of:

- Jetting voltage, responsible for amplitude of the piezo driving pulse
- Jetting waveform, which deals with the shape and width of the piezo driving pulse
- Jetting frequency, which deals with the number of cycles of the piezo driving pulse per second

A schematic of the different phases of a driving pulse designed for the DMC printhead is shown in Figure 2.30.

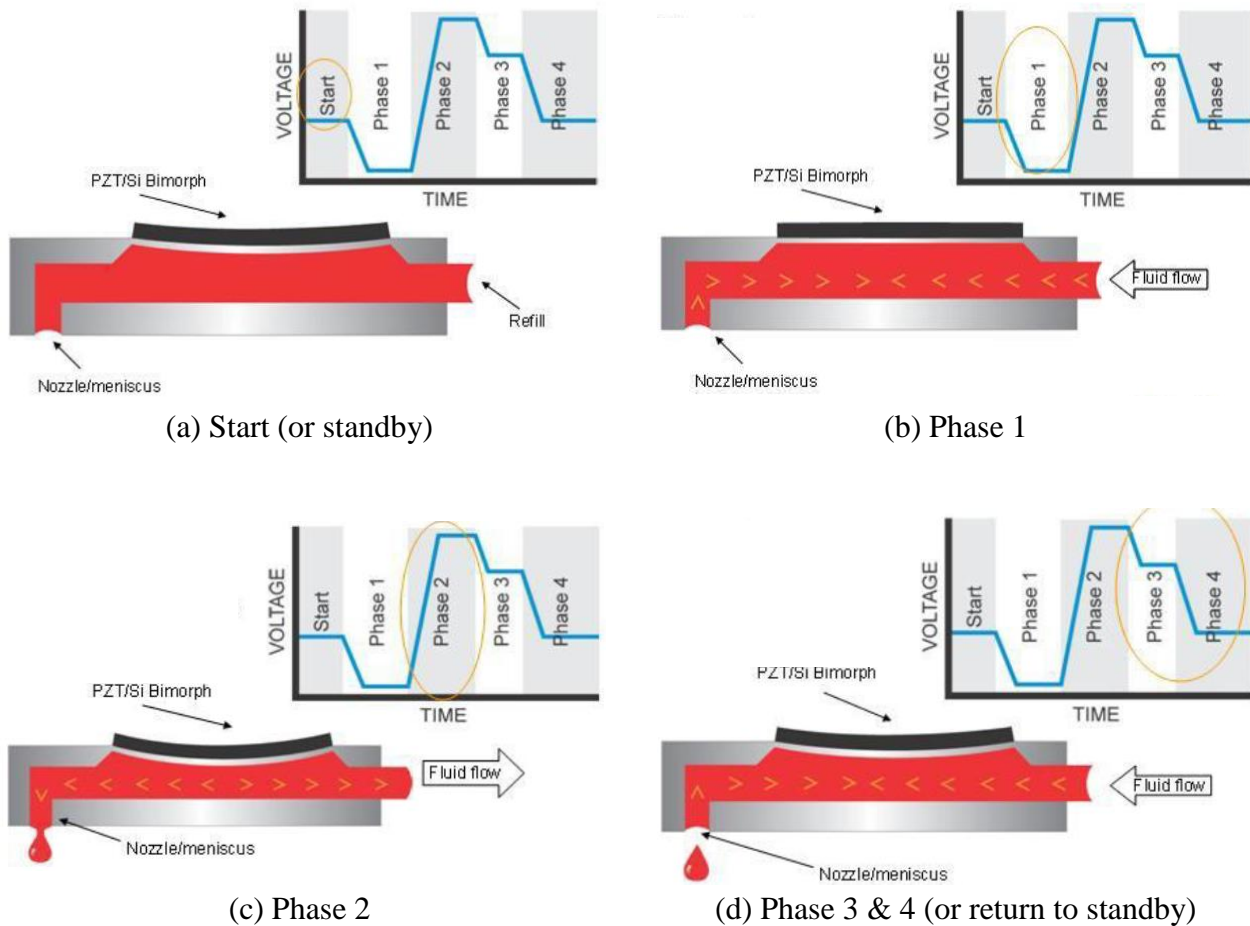


Figure 2.30: Schematic of different phases of driving pulse for DMC print-head [41].

Jetting voltage determines the droplet ‘jettability’ at a certain operating temperature. Temperature influences the deformation of piezo transducer. Jetting waveform is responsible for the quality of the jetted droplets. As shown in Fig 2.30, the waveform can be divided into four phases. By adjusting and optimizing the slew rate and duration of each phase, it is possible to get a better jetting quality. The slew rate controls how fast the piezo transducer bends and the duration dictates how long it stays in that position. In standby mode, the piezo transducer is slightly bended inwards prior to the main drive pulse. In phase 1, a negative pressure is created in the pumping chamber due to a decrease in voltage, which causes the ink to flow towards the piezo plate. In phase 2, the piezo transducer is bended inwards again due to a voltage increase, creating a force on the ink inside the pumping chamber to initiate drop formation. In phases 3 and 4, by decreasing the voltage in a controlled fashion, it is possible to break off the ejected fluid streams into individual droplets.

The last part of the drive pulse, is the jetting frequency, which determines how fast the jetting cycle is repeated. Usually there is a trade-off between jetting frequency and jetting quality, because by increasing the jetting frequency, we can obtain a faster printing speed, but on the other hand it can result in a poor jetting quality.

2.5.1.4 Ink requirements

The compatibility of an ink with the cartridge and print-head is the first thing to be considered. In this regard, two types of disposable Fujifilm Dimatix cartridges, DMC-11610, and DMC-LCP-11610, were examined.

For piezo DOD inkjet printing the desired viscosity range is 2-20 mPa.s or centipoise (cP) [42]. On one hand, fluid with a high viscosity may not be ejected out of nozzles, but on the other hand fluid with a too low viscosity may drip from the nozzles during idle time of the device. Viscosity is usually adjustable by changing ink’s temperature or adding solvents or other additives to the ink. Here, it is better to use a solvent with a high boiling point in order to avoid excessive evaporation, which might also lead to clogging of nozzles later on.

Besides rheology, surface tension also plays an important role, as it reflects the cohesive internal molecular forces within the ink (this aspect is not investigated in this thesis). In general, as has been established in literature, a lower surface tension is more favorable for surface wetting, but at the same time this can lead to satellite formation during the flight of droplets. Pictorial understanding can be obtained from Figure 2.31.

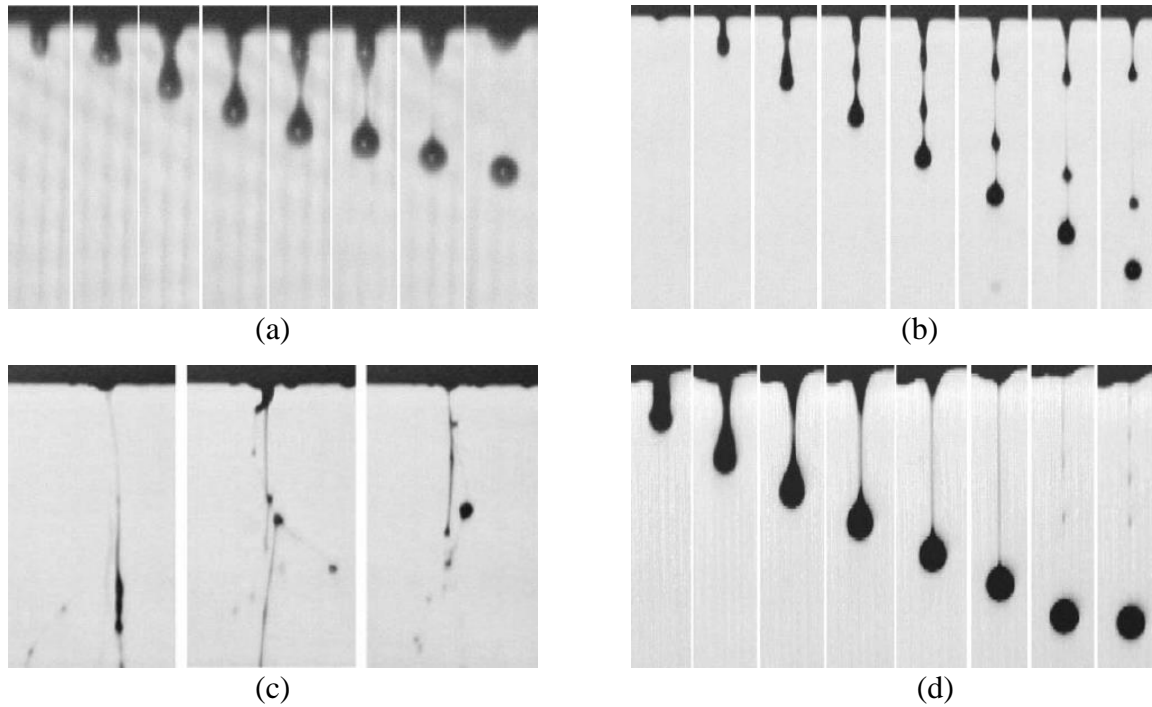


Figure 2.31: Jetting behavior of droplets from printer drop watcher, (a) favorable droplet formation, (b) formation of satellite droplets due to low surface tension, (c) random fluid spray, (d) long tail formation due to high jetting voltage or low surface tension [43].

2.5.1.5 Droplet behavior on substrate

The impact of droplets on substrate creates different flow patterns according to the properties of the ink and the substrate. Behavior of a droplet on the substrate depends on factors like the ink viscosity, surface tension, velocity and size of the droplet, and certain substrate characteristics like its roughness and its interaction with water (hydrophobic or hydrophilic). In Figure 2.33 the possible behaviors of a droplet falling on to a substrate are shown. The wetting behavior of a droplet on a substrate is usually described by its equilibrium contact angle (θ_{eq}), shown in Figure 2.32.

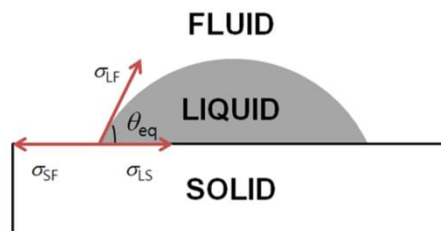
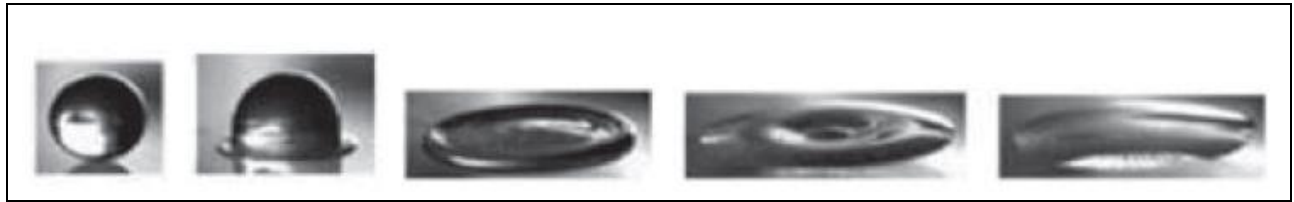


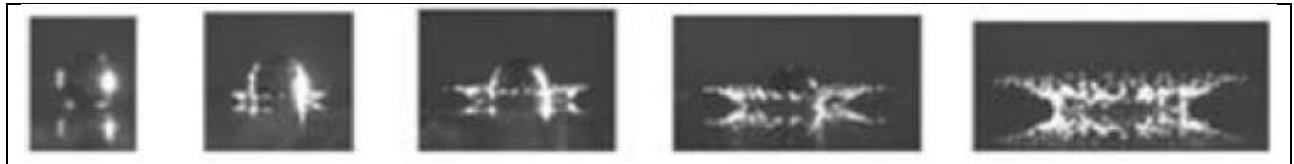
Figure 2.32: Equilibrium contact angle (θ_{eq}) of a droplet on a substrate [38]



(a) Deposition



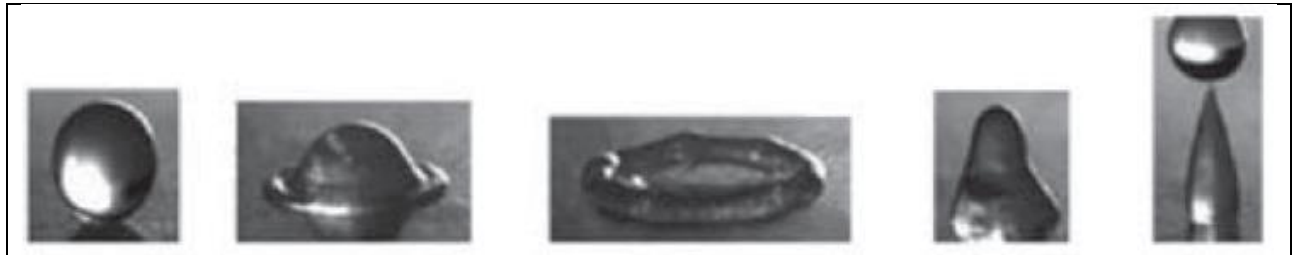
(b) Prompt splash



(c) Corona splash



(d) Receding breakup



(e) Partial rebound



(f) Complete rebound

Figure 2.33: Different behaviors of liquid drops upon impact with a substrate [44].

Where σ_{LF} , σ_{SL} , and σ_{SF} represent surface tension at the liquid–fluid, solid–liquid, and solid–fluid interfaces, respectively. For a plane substrate, the equilibrium contact angle is calculated using Eq. 2.34, which is known as Young’s equation.

$$\cos \theta_{eq} = \frac{\sigma_{SF} - \sigma_{SL}}{\sigma_{LF}} \tag{2.34}$$

The wetting behavior of a droplet with regard to the contact angle is shown in Figure 2.34.

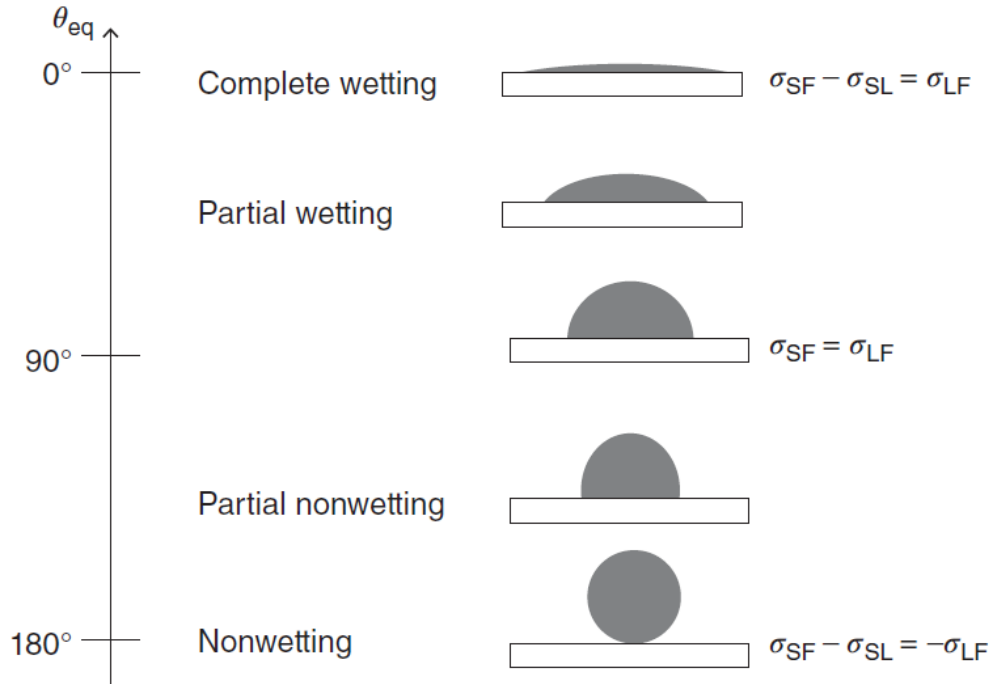


Figure 2.34: Wetting behavior of a droplet on a substrate [51]

In inkjet printing, wetting behavior of the droplets on the substrate is critical to obtain the desired feature size. The wetting behavior can be controlled by viscosity and surface tension of the ink, as well as the surface energy of the substrate. Contrary to the ink surface tension, a higher surface energy of the substrate leads to higher wettability and stronger adhesion.

Chapter 3

Experimental setup and Tools

This chapter is divided into several sections. The first section describes the experimental scheme followed during research conducted in this thesis, starting from lifetime sample development to final characterization techniques. It is followed by sections explaining the characterization techniques and working principle of the tools utilized at different stages of experimentation. Main characterization techniques used are Piezo Axial Vibrator (PAV) rheometer, optical microscope, quasi steady state photoconductance (QSSPC) and electrochemical capacitance-voltage (ECV). A section is also dedicated to Inkjet printing technique.

3.1 Experimental Design

Figure 3.1 illustrates the experimental scheme of this thesis, followed chronologically.

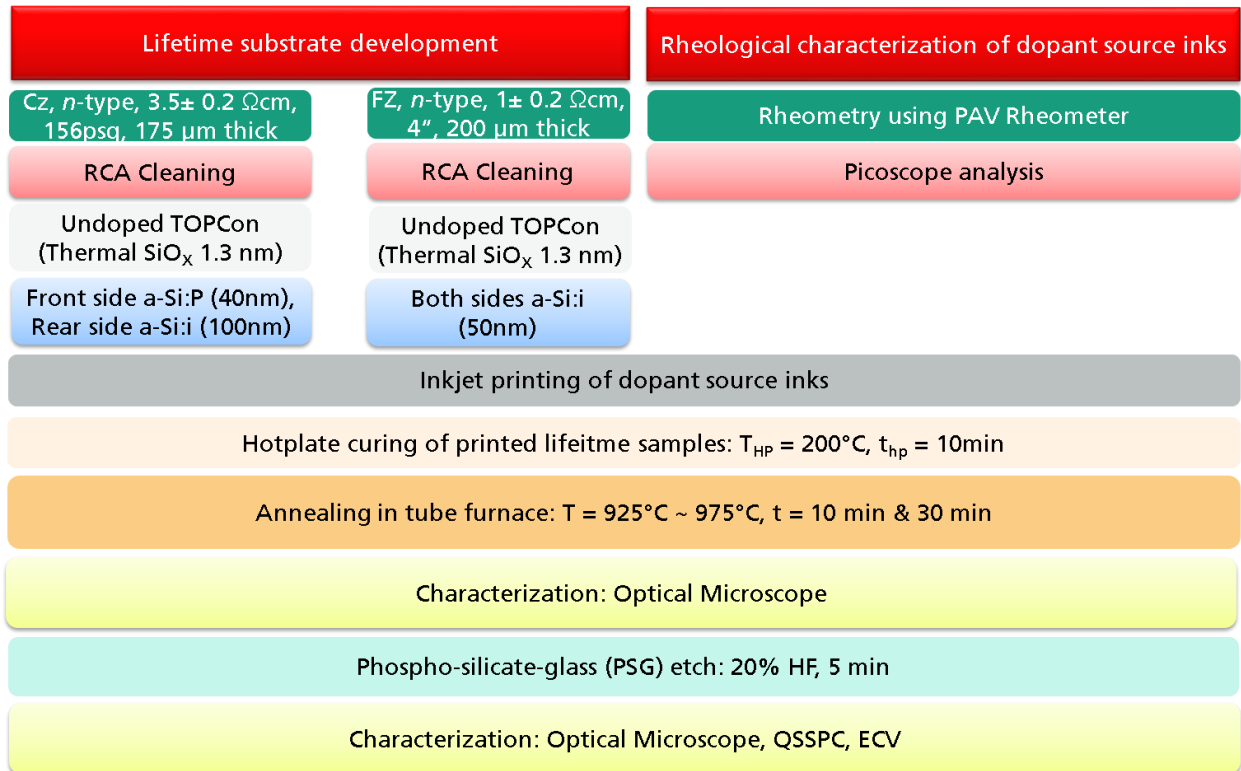


Figure 3.1: Schematic of experimental design of this thesis explaining steps chronologically.

Before printing, inks are assessed for their rheological behavior, in order to anticipate their printing behavior and to figure out the required steps to be taken while printing to produce desired results. This is done using Piezo Axial Vibratory (PAV) rheometer and Picoscope.

Following rheological analysis, inks with desirable characteristics were printed over different substrates using LP50 Inkjet printer. After printing the substrates with these dopant source inks, printed samples were cured on hotplate to remove organic solvents from the dopant source inks. This was followed by annealing at high temperatures to enable diffusion of dopants from the dopant source ink into the a-Si layer and simultaneously transform the a-Si layer into poly-Si. Poly-Si contact is a viable option for conventional solar cells due to its higher tolerance for high temperature processes. Following these steps we obtain c-Si/SiO_x/poly-Si junction, as shown for Cz samples, in Figure 3.2. In order to improve the electrical properties across this junction, the printed wafers were treated with H₂ plasma (Remote Hydrogen Plasma Treatment – RPHP), which improved the passivation quality significantly, as explained in detail in Chapter 4. Passivation quality was assessed through photoconductance evaluation while the concentration of active charge carriers available for charge transport was analyzed through electrochemical capacitance-voltage profiling.

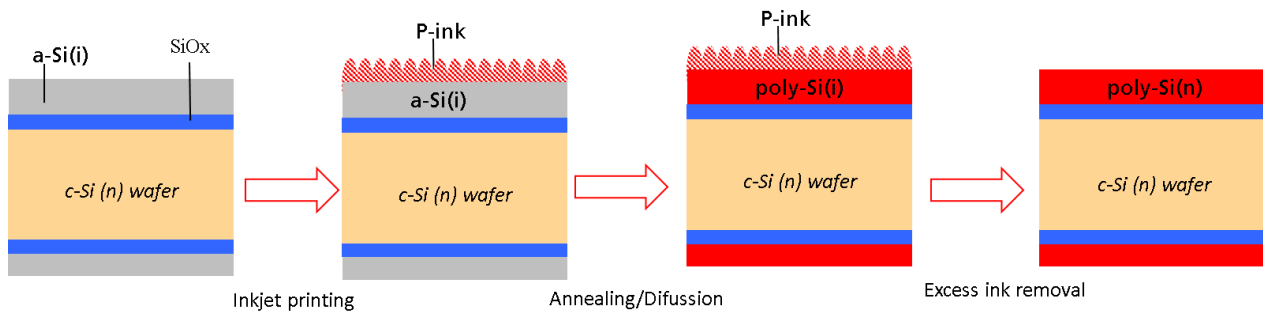


Figure 3.2: Schematic illustration of lifetime sample.

3.1.1 Lifetime sample development

To study the role of thickness of a-Si layer on lifetime of minority carriers, two samples with different a-Si thicknesses were used. As has been explained in Chapter 2, lifetime of minority carriers plays a fundamental role in determining the electrical characteristics of a solar cell. Besides the thickness of a-Si layer, the samples also differ in their manufacturing process, as has been explained in detail in the following subsections.

3.1.1.1 Czochralski (Cz) wafers

One type of wafer used in this thesis is monocrystalline silicon wafer, manufactured by the Czochralski process[45]. These wafers inhibit higher bulk charge carrier lifetime than multi-crystalline silicon wafers. A higher lifetime is of prime importance for high-efficiency solar cells like IBC because most of the charge carriers are generated at the illuminated front side of solar cell. For the collection of charge carriers by the emitter region, the minority charge carriers have to diffuse through the whole bulk to reach the rear side. To enable long diffusion lengths, a material with a high bulk carrier lifetime is mandatory.

Cz-Si wafers are fabricated by the Czochralski process that follows a technique of crystal pulling using a seed crystal, which is dipped into molten silicon. By constantly rotating and pulling the

crystal seed upwards, a big cylindrical ingot is extracted from the melt, typically 200 mm in diameter. Next, four slices are sawn off the ingot resulting in a “pseudo-square” (psq) ingot with a side length of 156 mm. The pseudo-square ingot is converted to pseudo-square wafers by sawing techniques, such as, slurry-based wire sawing or diamond-wire based sawing. A schematic of pseudo-square (monocrystalline) wafer used in this thesis is presented in Figure 3.3. By dissolving phosphorus or boron into the Si melt, *n*- or *p*-doped wafers are produced.

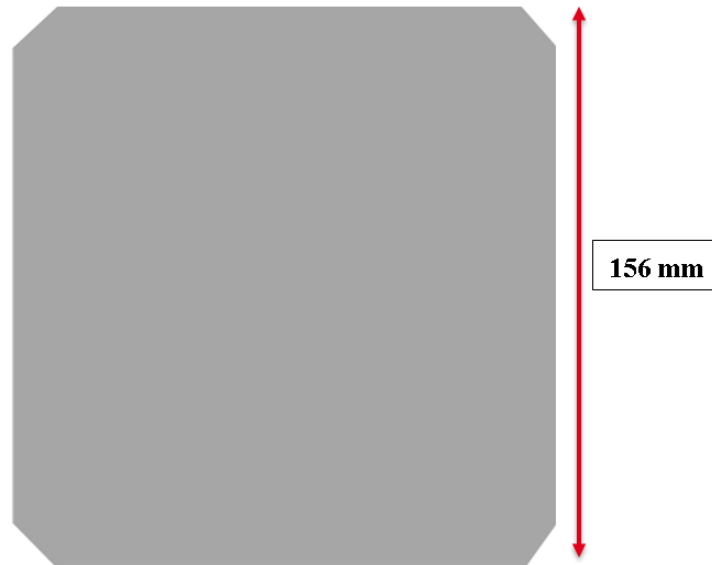


Figure 3.3: A 156 mm edge length pseudo-square wafer with SiO_x passivation.

Thermal Growth of Tunnel Oxide (SiO_x)

A SiO_x layer naturally grows on a silicon surface at room temperature up to 15Å. However, this native oxide layer is not stable. Therefore, other methods are used in PV community to grow ultrathin tunnel oxide layer (~1.3 nm SiO_x), such as:

- Wet chemical growth in 68 wt% nitric acid at 110°C for 10 min [46, 47]
- Wet chemical growth in ozonized DI-water at 30°C with a constant ozone concentration of 30 ppm and various exposure time (t = 3, 5, 10, 15 min)
- Photo-oxidation with UV/Ozone Sources [48, 49]
- Thermal oxidation

In this thesis, 1.3 nm thick SiO_x is grown over the c-Si substrate by thermal oxidation. To this end, wafers were cured in a furnace with O₂-rich atmosphere at 600°C for 10 min.

3.1.1.2 Float Zone (FZ) wafers

Besides Cz, another type of wafers used in this work are monocrystalline silicon wafers, manufactured by Float Zone (FZ) process [50]. In this process, a molten region is formed around a rod of silicon, using a heating coil (RF coil). Impurities like Oxygen, which reduce the minority carrier lifetime in the solar cell tend to stay in the molten region, which offers a zone of high mobility, instead of diffusing into the solidified region. As the heating coil moves, the molten region travels along with it, aggregating all the impurities contained in the Si ingot. After the molten area has passed, a very pure single crystal is left behind.

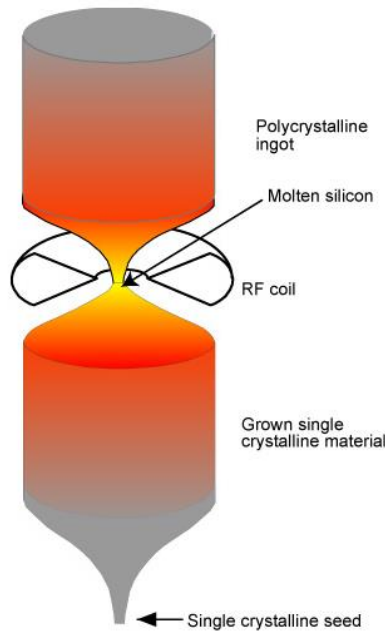


Figure 3.4: Schematic of Float Zone (FZ) wafer growth [51]

FZ wafers used for this research are n-type with resistivity of $1 \pm 0.2 \Omega\text{cm}$, diameter of 4 inches and a thickness of $200 \mu\text{m}$. FZ wafers are usually used for high efficiency solar cells or laboratory cells and not for commercial production because of the difficulty and cost of the process [52]. The schematic of FZ technique is illustrated in Figure 3.4. The FZ wafers used in this thesis are shiny etched, thus having smooth reflective surfaces and a different texture than the Cz wafers used. Kind of texture plays a crucial role in determining wetting behavior of inks. Poor surface-ink interactions can lead to de-wetting and undesirable structural flaws in the printed layers.

3.1.1.3 Lifetime samples used for printing

In this thesis, the lifetime samples used, contain a layer of thermally grown 1.3 nm thick SiO_x for tunnel oxide passivating contact (TOPCon), on both sides. Lifetime samples were prepared with different thickness of amorphous silicon (a-Si) layers deposited by means of Plasma Enhanced Chemical Vapor Deposition (PECVD) and Low-Pressure Chemical Vapor Deposition (PLCVD), as mentioned below. Lifetime samples enable characterization of charge carrier lifetime at different injection levels through photoconductance measurements.

a) Lifetime samples with 100nm PECVD (a-Si) TOPCon

These wafers are n-type Czochralski (Cz), 175μm thick, 156psq with a saw damaged etched surface and base resistivity of $3.5 \pm 0.2 \Omega\text{cm}$. Using these samples, doping and electrical performance of inks are evaluated for TOPCon with relatively thick, 100 nm a-Si layers deposited with PECVD. Due to overall lesser costs incurred by PECVD, aided by low temperature (200°C-300°C), high deposition rates (1000Å/min) and smaller post cleaning times (<15min), the technique is used for industrial production. PECVD enables single side deposition of large areas. Hence, lifetime samples of this group are compatible with industrial TOPCon (i-TOPCon) precursors. In the later processing stages, these wafers undergo screen-printing for metallization and subsequent high temperature firing. Such high temperatures can produce metal spikes, which can damage the thin tunnel oxide. Thick a-Si layer prevents such damages and aids maintenance of solar cell efficiency. On one side of this substrate, a-Si isn-doped using P-ink. The other side has n-type PECVD a-si, which offers a very high passivation quality. Since the performance of PECVD in-situ doped side is already known, this combination allows investigation of performance P-ink alone. With both sides PECVD doped, ~735-740mV iVoc and 84-85% iFF is obtained. Therefore, any change from these established values indicates the performance of dopant source ink, positive or negative. A schematic of the samples used is shown in Figure 3.5.

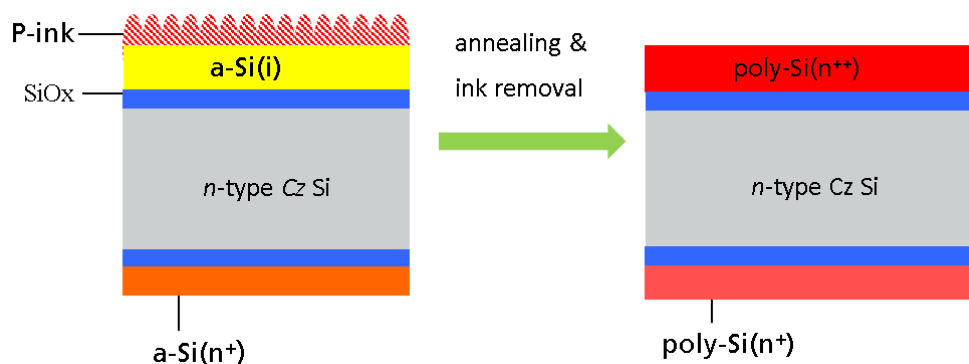


Figure 3.5: Schematic of lifetime samples with saw damage etched surface with 100nm a-Si layer on front side. SiO_x between a-Si and c-Si substrate is the tunneling layer.

b) Lifetime samples with 50nm LPCVD (a-Si) TOPCon

These wafers are n-type Float Zone (FZ), 200 μ m thick, 4in. in diameter, shiny etched surface with a base resistivity of $1\pm 0.2 \Omega\text{cm}$. These wafers have a thin layer of a-Si deposited using LPCVD technique at 485°C. Owing to the expensive requirements of LPCVD, like high operating temperature (600°C-800°C), low deposition rates ($\sim 20\text{\AA}/\text{min}$), large post cleaning times (4h), etc. the wafers produced by this process are used for research purposes. The wafers later undergo clean room processes and low temperature metallization processes which are further required for development of electrical contacts. On one side of these sample we have Boron-ion implanted p-type dopants while P-ink is printed on other side for n-type dopants. This resulted in development of a complete p-n junction, later to be used for solar cells. A schematic is shown in Figure 3.6.

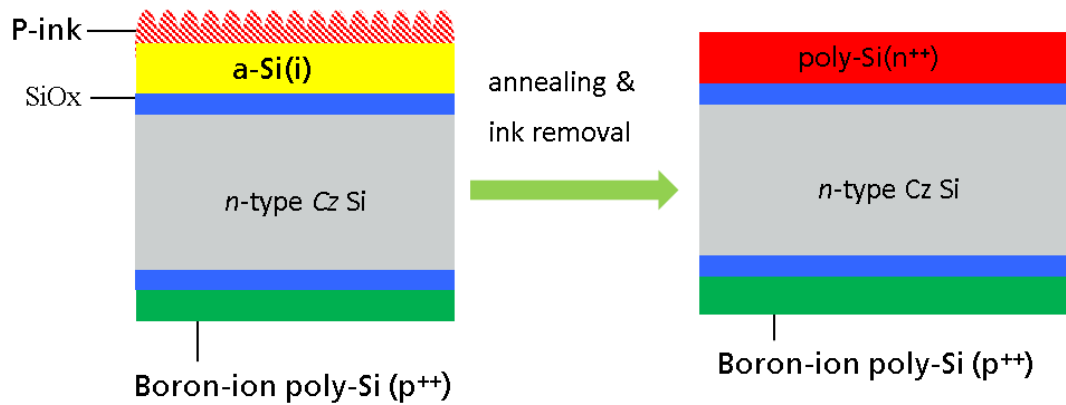


Figure 3.6: Schematic of lifetime samples with shiny etched surfaces with 50nm a-Si layer on both sides. Front side is B-ion doped and the rear side is printed n-doped.

Different thickness of a-Si layer has been used in order to ensure minimal damage caused during metallization process in the later stages of solar cell development from the same lifetime samples. Through PVD metallization, the deposition temperature is below 100 °C. At such temperatures lesser free carrier absorption (FCA) is experienced and therefore using 50 nm thick layer is feasible.

However, screen-printing metallization followed by a high temperature firing step creates metal spikes which can degrade passivation quality of TOPCon by penetrating in to the tunnel oxide. In order to avoid such degradation, we use a thicker a-Si layer – 100 nm.

Therefore, depending on metallization technique and making a compromise between parasitic absorption and degraded passivation, thickness of the a-Si layer is chosen accordingly.

3.2 Ink Characterizations

Before inkjet printing, it is crucial to characterize the ink behavior. To do so, viscoelasticity and waveform simulation measurements were conducted, to get a better understanding of rheological and printing behavior of the ink.

3.2.1 Dopant source inks

Based on composition, inks have been classified into three batches, as shown in Table 3.1. Each batch consists of both Phosphorus (P) and Boron (B) dopant source inks (proprietary). All the inks used in this thesis were outsourced due to which their exact composition is unknown. Due to different proprietary formulations, we have categorized inks based on their composition.

Batch 1 consists of two inks; one P-ink and one B-ink. Both the inks are ‘spin-on glass’ and belong to chemical family of ‘Organometallic Solution’. Phosphorus *silicate polymer* and boron silicate polymer are the dopant sources for P and B inks, respectively. The polymer accounts for < 20% of the solution and the solvent comprises of ethanol, isopropyl alcohol, glycerol, cyclohexanol, methanol and ethyl acetate. Inks have been stored under recommended dry refrigerating condition (< 5°C).

Batch 2 consists of four inks; two P-inks and two B-inks. Dopant source for these inks is also P/B-*silicate polymer*. P-inks differ only in the concentration of their P atoms, P-ink 2 having higher concentration than P-ink 1. The solvent for P- inks is primarily aqueous ethanol. Storage conditions are the same for both of them- dry and cold (< 5°C). For B-inks, difference lies in their solvent composition and storage conditions. B-ink 1 is cold temperature ink with solvent composed of alkoxy-alcohols while B-ink 2 is room temperature ink with solvent made up of aqueous propylene glycol methyl ether.

Batch 3 also consists of four inks; two P-inks and two B-inks. Dopant source for this batch are *resins* containing phosphorus and boron, which account for 1- 10% of the solution. All the inks of this batch are stored under dry atmosphere at room temperature. For P-ink 1 and B-ink2, the solvent is composed of 1-pentanol, while for P-ink 2 and B-ink 1, the solvent is glycol ether. Solvent comprises < 80% of the solution.

Table 3.1: Classification of Polymer based dopant source inks in alcoholic solvents.

Batch Number	Batch 1	Batch 2	Batch 3
Composition	Organometallic (silicate polymer) solutions	Polymer in alcohols	Resinous inks
No. of P inks	1	2	2
Age of P-inks	1 month	Ink 1- 4months Ink 2- 2months	Ink 1- 4months Ink 2- 6months
% polymer	< 20%	-	1-10%
Solvent	Ethanol+Glycerol	Ethanol (Aqueous)	Pentanol/ Glycol ether
Storage condition	Cool/Dry	Cool/Dry	Room temperature/Dry
No. of B-inks	1	2	2
Age of B-inks	1 month	4 monthss	Ink 1- 4months Ink 2- 7months
Storage condition	Cool/Dry	Ink 1- Cool/Dry Ink 2- Room temperature/Dry	Room temperature/Dry
% polymer	< 20%	-	1-10%
Solvent	Ethanol+Glycerol	Ethanol (Aqueous)	Glycol ether/ Pentanol

*Aging time- time elapsed from the time of fill of inks to their first use.

3.2.2 Rheological Measurements

Complex viscosity (η^*), elastic (G') and viscous (G'') components of the complex modulus (G^*) of dopant source inks are measured using Piezo Axial Vibrator (PAV) rheometer. The PAV is a squeeze-flow rheometer working at frequencies between 1 and 10,000 Hz. This is an advantage offered by Piezo Axial Vibrator (PAV) Rheometer over others such as rotational rheometers which offer results for $< 10^2$ Hz. The enhanced features offered by the device, as mentioned below, enabled characterizing inks for a wide frequency range and at different temperatures (25°C and 45°C in our case). Using this robust instrument, we could generate reliable data, which very well anticipated the changes that could be required during printing operation. The sample holder of the rheometer is highly sensitive and can detect small changes. Moreover, it minimizes the volume of sample needed to carry out complete characterization to only 2-3 drops (< 0.1 ml). The device being well-jacketed (white colored jacket in the Figure 3.5) ensures minimal heat loss. Therefore, much time is not to spent while changing samples at higher temperatures and stabilization is achieved quickly. The data obtained from the device is supported by and equally robust software. The whole set up enables rheological analysis of the samples in finer details.

Instrument

PAV rheometer used in this work has the following specifications:

- Frequency range: 1 Hz to 10,000 Hz
- Temperature range: -5°C to 80°C
- Viscosity range: 0.5 mPa.s onwards
- Test duration: 1 Hz to 10,000 Hz sweep < 5 min



Figure 3.7: PAV rheometer setup at Fraunhofer ISE.

PAV setup consists of PAV rheometer, lock-in amplifier (SR860, Stanford Research Systems, Inc.), thermobath (CORIO C-BT5, Fisher Scientific GmbH), and a thermometer (GMH 3700, GHM Group – Greisinger) as shown in Figure 3.7.

The device is based on micro-rheological techniques of assessing fluid properties. It consists of a dynamic press with a thin gap in which the liquid is confined. A squeeze-flow is generated by a piezoelectric drive and the response of the system, which is measured by piezo-sensors leads us to evaluation of G' and G'' in the given frequency range. By covering rheological properties over a wide range, the device gives us low frequency data, which is necessary to attain the first Newtonian region as well as high frequency data, which provides an insight into the inter-particle forces and hydrodynamic interactions. Thus the device offers a great advantage of PAV compared to other rheometers, that is closes the gap between conventional mechanical rheometers, which produces results for < 50 Hz and torsional resonators which operate only in the kHz range [53]. This frequency range provides comprehensive data required to understand the nature of complex fluids.

Working Principle

Zero shear rate viscosity at their jetting temperature usually characterizes Inkjet fluids. The zero viscosity (η_0) is measured at very low shear rate and displays viscosity of a material at rest, which is one of the most important rheological parameters used in polymer industry. However, fluids containing polymer solutions and solid particles may show *viscoelastic* behavior. Typical laboratory low-shear rate viscometers which carry out viscosity measurement in low frequencies (<100 Hz) are unable to characterize viscoelastic behavior of piezo DOD inkjet fluids because these fluids usually experience much higher frequencies (up to 100 times greater) in inkjet technology, during jetting process. The rheological behavior of viscoelastic fluids is usually presented in terms of complex viscosity (η^*), as explained through following equations:

$$\eta^* = \frac{G^*}{i\omega} \quad (3.1)$$

$$G^* = G' + iG'' \quad (3.2)$$

Where G^* is complex modulus at angular frequency ω ($=2\pi f$ at frequency f). G' , represents the elastic (storage) modulus, and G'' the viscous (loss) modulus [54, 55].

Schematic of the PAV is shown in Figure 3.9. The lower plate of the device oscillates with constant force amplitude F . Upon unloading, the dynamic displacement of the lower plate, x_0 is measured, leading to the compliance x_0/F . On repeating the same measurements with the material to be evaluated, filling the gap between two plates, we obtain modulated compliance x/F . Using the complex ratio x_0/x and an appropriate mechanical equivalent circuit (shown in Figure 3.9 (b)), its equations of motion produce the complex squeeze stiffness K^* , as given by equation 3.3

$$K^* = \frac{\frac{3\pi}{2}R \left(\frac{R}{d}\right)^3 G^*}{\left(1 + \frac{\rho\omega^2 d^2}{10G^*} + \dots\right)} \quad (3.3)$$

where, R is the radius of the plate (which is 10 mm in our case), $d \ll R$ is the gap width, ρ is the density of the squeezed sample, and G^* is the complex shear modulus. The first term in the denominator, represents the slit approximation. It takes into account the inertia of the material in the gap, which plays a significant role at high frequencies. However, the above equation assumes the material under evaluation to be incompressible. To make the measurements more accurate, dynamic compressibility factor, κ^* must be taken into consideration. As has been found by Kirschenman et al [56], in the limit of small amplitudes, for squeeze flow, we obtain;

$$\frac{1}{K^*} = \frac{2}{3\pi} \frac{d^3}{R^4} \left(\frac{1}{G^*} + \frac{3R^2}{2d^2} \kappa^* \right) \quad (3.4)$$

Equation 3.4 takes into account the correction due to a finite compressibility, which strongly depends on ratio R/d and can be measured using different d values. Repetition of experiments enables achieving reliable values for the G^* with values as low as 0.1 Pa. Measurements done for different gap thicknesses can be done using shims of different thicknesses. Shims are stainless steel ring micro-foils, which hermetically seal the two plates by adjusting the gap in between.

Depending on the viscosity of the material to be characterized, we use shims of different size; higher viscosity samples requiring thicker shims. Shims of thickness varying from $10\ \mu\text{m}$ to $500\ \mu\text{m}$ are available for the PAV rheometer at Fraunhofer ISE. This allows characterization of samples in a wide range of viscosities, from $\sim 1\ \text{mPa}\cdot\text{s}$ to $> 1500\ \text{mPa}\cdot\text{s}$. With its high sensitivity and precision, the device produces results (G' , G'' , G^*) with accuracy p to the sixth decimal place.

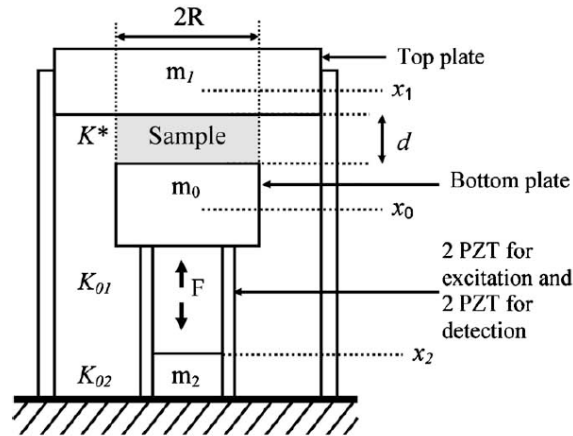


Figure 3.8: Geometric analog of PAV (Kirschenmann, L., Ph.D. thesis, University of Ulm, 2003) [57].

Device details (while operating)

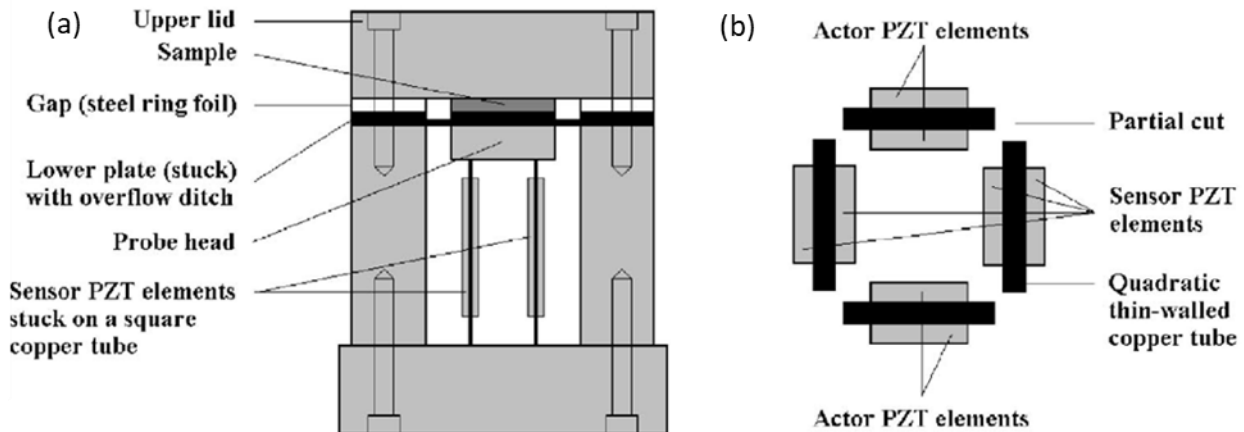


Figure 3.9: (a) Longitudinal cut view of Piezoelectric Axial Vibrator (PAV) rheometer used in this thesis. (b) Transverse cut view of the PAV, with top late removed. Quadratic tube contains the actor and the four piezo-elements stuck on both sides of two opposite tube walls. Remaining two walls contain four more sensors [53].

The actor/sensor contained in the dynamic press PAV, as shown in Figure 3.9, is a quadratic copper tube. Two piezo-elements attached to the two opposite walls of the copper tube exert vibrations on the material and the remaining four receive the response signal. Four lengthwise cuts in the tube, as shown in Figure 3.10 (b) ensure that there is no direct coupling between excitation and detection. The lower part of the device is held in a water-jacketed cylinder, which enables circulation of water (cold/hot) around the whole assembly. This provision allows temperature dependent rheological characterization of the material. Lock-in amplifier, showed in Figure 3.7, operates the rheometer with the voltage input proportional to the axial force of the exciting piezo-elements. The rigidity of the sample should be lower than 10^9 Nm^{-1} . This is required because the rigidity of the cylinder must be at least $1 \times 10^8 \text{ Nm}^{-1}$, in order to ensure a high resonance frequency for the head of the probe and the body of the cylinder. To find the rigidity K^* of the material, we use the voltage signal received from the piezo-elements, which monitors the deformation, and the width d i.e. the gap of the squeeze flow rheometer, dictated by the shim number used - Sh30 ($30 \mu\text{m}$) in this thesis. In order to determine the exact width d between the two rheometer plates for a given shim size, the device must be calibrated. The PAV rheometer in the present work was calibrated using ISO certified ‘general purpose viscosity standard’ S20, for shim Sh30.

PAV rheometer uses a small volume of the material (ink) used for characterization ($\sim 0.1 \text{ ml}$) and exhibits high signal sensitivity of the device (which lies between 1.0001 – 0.2 for most inkjet inks). As a result, the response can get easily corrupted in presence of unwanted agents such as fibers, from the wipes of tissue or due to air bubbles trapped in fluid while sealing the plates after sample loading. This can produce false results. Therefore, care must be taken to use fiber free wipes and to artistically place the covering plate on top avoiding air bubbles. To ensure completely clean surface for new sample, cleaning with IPA/ethanol/acetone is recommended.

Each measurement, at a given temperature, must be preceded by a blank measurement, without any sample, to create a reference for correct evaluation of data obtained for samples. Signal sensitivity for blank measurement is 1, sans sample. If working at the same temperature for long time, the blank measurement must be repeated after a couple of hours. This ensures nullification of the noise that can creep over repetitive usage. A blank measurement made at one temperature must not be used for other temperatures. Although the device offers temperature sensitivity of 0.1°C , we used external thermometer with a resolution between 0.01°C and 0.01°C .

Limitations and artifacts

Certain negative outcomes were recorded during experimentation, which invalidated some parts of our results. Although some of them can be taken care of, the others get too trivial depending on behavior to fluid, especially if the chemistry is unknown. Some of them are as listed:

- Data for small frequency ranges

The results are not always obtained for the entire range of 1-10,000 Hz. As was witnessed during the work included in this thesis, some results, especially for aged inks and for measurements at high temperatures, rheological results ended at frequency as low as 500 Hz. This is related to the reduced viscosity of the inks due to high temperatures or due to aging. In order to obtain results over complete range a shim producing smaller width may be used.

- Negative G' values

This can be related to two results:

- Signal sensitivity outside the prescribed limit.

When the sensitivity is below the lower limit, i.e. 0.2, the received signal is very weak, close to the damping within the noise error of the instruments, producing negative G' .

When the sensitivity is above the upper limit, i.e., 1, the results produced are again unreliable as this implies a higher response from the sample than from blank measurement itself. For such cases the negative values of G' must be discarded and treated as instrument error. In this case we can try using shims of different thicknesses in order to maintain sensitivity within prescribed limits (1-0.2).

- Phase angle more than 90°

This can occur for some Newtonian inks, while calculating squeeze flow rheological properties from mechanical spring/fluid stiffness, as described in the sections above. In this case, the negative G' values should be treated equal to 0 i.e. complete Newtonian response. However, we can also make phase corrections through the PAV software.

- Invalid data points

Sometimes, the device produces invalid data points for some frequencies in case the sensitivity of the device becomes greater than the upper limit, i.e. 1, since the response signal of the sample should not be greater than blank. In case the sensitivity goes above 1, it implies resonance of sample at that sample gap size and frequency. Using smaller gap size by using a smaller shim can be of help in such cases.

It is also important to note that the lower limit of signal sensitivity may need to be changed manually to 0.1 for very low viscosity fluids and 0.3-0.4 for high viscosity fluids (> 1000 mPa.s). Ideally the signal sensitivity should be flat (~ 1) at lower frequencies, reducing with frequency.

3.2.3 Picoscope-Oscilloscope Measurements

In order to anticipate the behavior of ink in response to the voltage waveform of Inkjet printer, we simulate the electrical conditions produced at the printer nozzle, using a Picoscope.

Instrument

Picoscope is computer software for real-time signal acquisition of Pico Technology oscilloscopes. Also referred to as PC Oscilloscope, it is a measuring instrument consisting of a hardware scope device and an oscilloscope. Oscilloscopes were originally stand-alone instruments with no signal processing or measuring abilities, and with storage only available as an expensive extra. A Picoscope, which operates with Window/Linux, etc. operating systems is thus very user friendly and in addition has minimum laboratory requirements. PicoScope 2000 Series can be used as an advanced oscilloscope, spectrum analyzer, function generator, arbitrary waveform generator and protocol decoder out of the box. The device used in our work is shown in Figure 3.10. The sample holder for Picoscope is the same as that for PAV Rheometer, shown in Figure 3.7.



Figure 3.10: Picoscope 2000 series used for waveform simulation for dopant source inks[58].

The device comes with the following specifications:

- Bandwidth: 10MHz to 100MHz
- Input sensitivity: 10 mV/div to 4 V/div
- Input coupling: AC/DC
- Input connector: BNC(f)
- Vertical resolution: up to 12 bits

Working Principle

An oscilloscope is a laboratory instrument commonly used to display and analyze the waveform of electronic signals through a graph plotting instantaneous signal voltage as a function of time, as shown in Figure 3.11, drawn by the device.

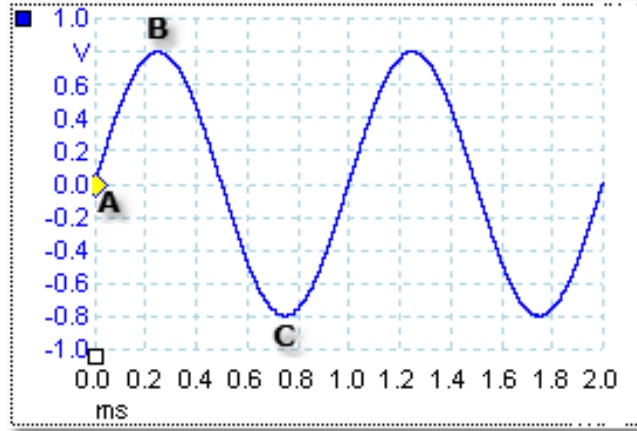


Figure 3.11: Sinusoidal voltage as a function of time, generated by Picoscope [59].

In Figure above, going from left to right, we observe the sinusoidal characteristic of the signal, or waveform obtained from an oscilloscope, drawn as a line called the ‘trace’ (marked in blue). Points B and C represent positive and negative peaks of the signal and A is the starting point (0V, 0s).

A typical oscilloscope can display alternating current (AC) or pulsating direct current (DC) waveforms having a frequency as low as approximately 1 Hertz (Hz) or as high as several megahertz (MHz). High-end oscilloscopes can display signals having frequencies up to several hundred GigaHertz (GHz). The display is broken up into so-called horizontal divisions (hor div) and vertical divisions (vert div). Time is displayed from left to right on the horizontal scale, called ‘collection time’. The *horizontal sweep* is measured in seconds per division (s/div), milliseconds per division (ms/div), microseconds per division ($\mu\text{s}/\text{div}$), or nanoseconds per division (ns/div). Instantaneous voltage or the ‘input range’, appears on the vertical scale, with positive values going upward and negative values going downward. The *vertical deflection* is measured in volts per division (V/div), millivolts per division (mV/div), or microvolts per division ($\mu\text{V}/\text{div}$). Virtually all oscilloscopes have adjustable horizontal sweep and vertical deflection settings.

During ink characterization, rectangular wave was used for simulating the printer waveform. A rectangular wave consists of all the other waveforms, including sinusoidal inputs. Since we use Picoscope in ‘Scope view’ mode, the output obtained is sinusoidal. A typical example of input/output curves is shown in Figure 3.12.

We can relate the peak of the output sinusoid to timescale of the peak of the voltage pulse in printer waveform. Using the timescale of different steps of waveform, used to print reference ink, we can establish a quantitative relation between Picoscope output and pulse waveform. A comparative analysis can then be drawn for other inks using the quantitative relation set up for reference ink. Accordingly, we can determine the shift in the time scale of pulse waveform required by each ink. Detailed explanations of quantifying Picoscope results, along with examples and details of voltage waveforms of Inkjet printer are explained in section 4.2.

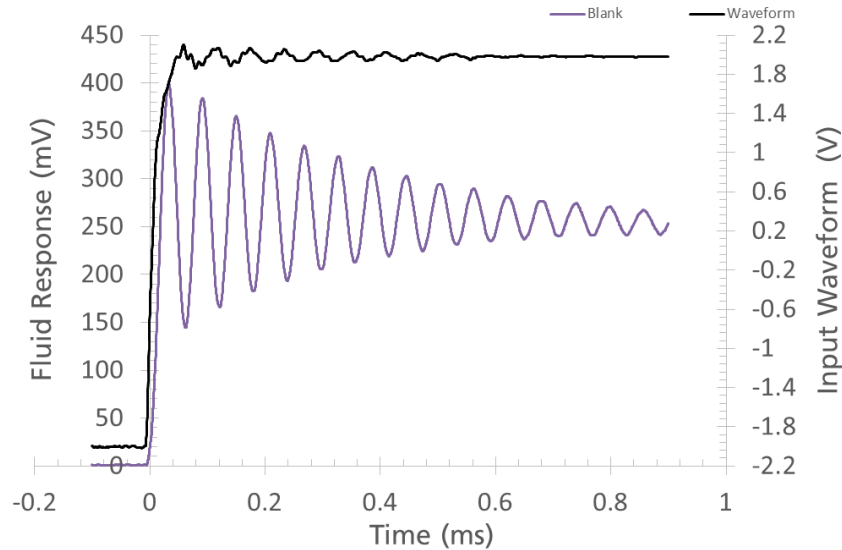


Figure 3.12: Sinusoidal voltage (marked in purple) as a function of time- output generated by Picoscope. Over time, the output signal gets attenuated. Curve in black represents input rectangular wave, distorted due to device noise (adapted from sample tests conducted by Tri Tuladhar).

3.3 Inkjet Printing

The printer used in this work is PiXDRO LP50, manufactured by Meyer Burger is shown in Figure 3.13. The printer, specifically designed for the research and development of inkjet printing processes, was customized at Fraunhofer ISE to be compatible with Fujifilm’s “Dimatix Materials Cartridges” (DMC). There are various print-heads with nozzle range of 1-1000, having a drop volume in range of 4-200 pL with an accuracy of up to 5 μm enabling printing of high resolution patterns. They carry their own reservoirs and are designed especially for functional fluids. The printer is capable of 5-axis motion including motion of substrate table with printing area of 210x300 mm. By varying voltage and other parameters of applied wave, such as the angle of print head and the droplet size, volume and speed, the drop spacing can also be controlled. Besides temperature control, the printer is also equipped with *printview* camera, which allows observation of printed structure and a *dropview* camera which allows real-time imaging of drop ejection. Moreover, we can also monitor drop formation through Advanced Drop Analysis (ADA) software inbuilt with the printer.

The LP50 printer used in this work is inside glovebox (GS GLOVEBOX Systemtechnik GmbH) with ambient pressure of 0.8 mbar, and O_2 and H_2O levels of 3 and 0.7 ppm, respectively as shown in Figure 3.14.

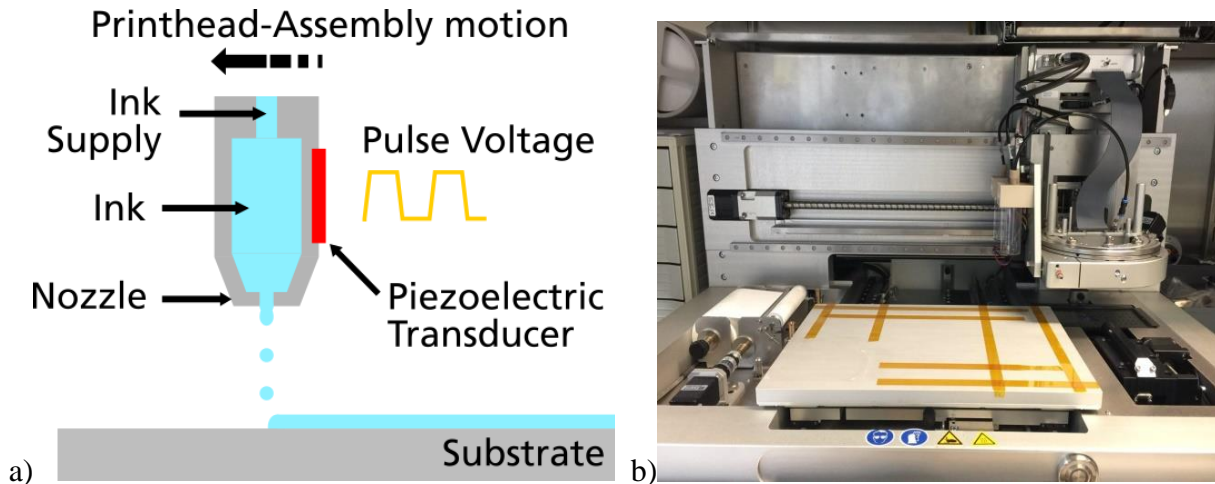


Figure 3.13: a) Schematic representation of working principle of inkjet printing, b) MeyerBurger LP50 inkjet printer.

Using Inkjet printer, we can define the printing resolution in terms of drops per inch (dpi). Full printed areas, however, can have variations between drop densities (cm^{-2}) which renders the quantity 'dpi', less accurate for defining the homogeneity of the printed structures. Similarly, in case we have to print lines, we can observe variations in terms of pitch (μm). In this thesis, we use only 600x600 dpi, optimized for printing full areas.

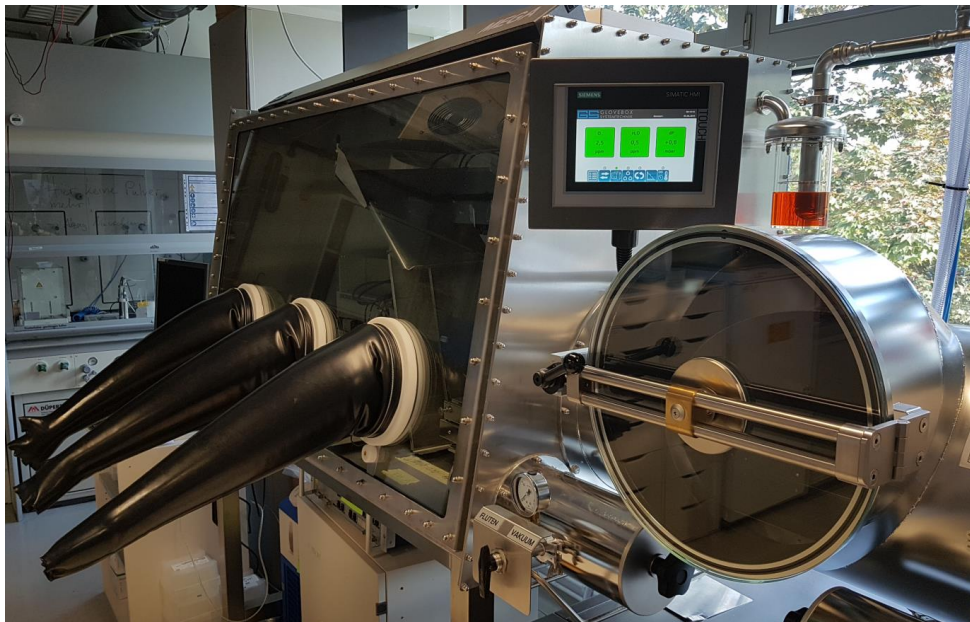


Figure 3.14: GS glovebox with gas purifier system at Fraunhofer ISE.

3.4 Printed Sample Characterization

3.4.1 Optical Microscope

Annealed printed samples were characterized using an optical microscope. It was used to acquire images of the samples following HF treatment after annealing/diffusion to assess the homogeneity of the printed dopant layers and the changes that occur during the diffusion process. The images were analyzed and compared for both inks, mostly qualitatively, featuring distribution of ink over the substrate surface. Quantitatively this has an impact on the distribution of dopants inside the substrate the distribution of charge carriers. For this inspection, a microscope that is called as ZEISS Axio Imager Vario (Carl Zeiss Microscopy GmbH; Jena, Germany) was used. The image of the used Carl Zeiss microscope is shown in Figure 3.15.

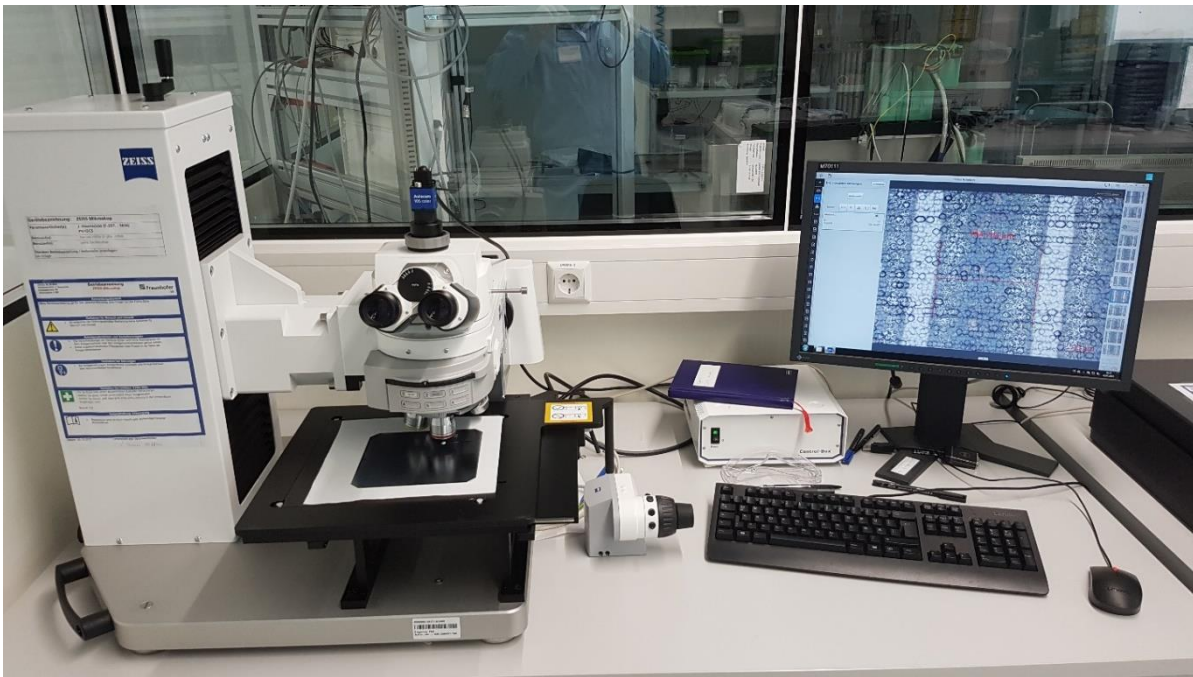


Figure 3.15: Carl Zeiss Microscope at Fraunhofer ISE.

The microscope is connected to a PC which enables viewing the substrate surface on desktop and user no more needs to use eyepiece. Wafers are laid over the table which can be moved in X and Y direction by rotating knobs.

3.4.2 Electrochemical Capacitance Voltage (ECV)

Various techniques can be used to measure concentration of charge carriers, such as, spreading resistance profiling (SRP), secondary ion mass spectroscopy (SIMS), and capacitance-voltage (CV). Traditional capacitance-voltage (CV) technique has a limitation in depth of profiling due to reverse bias breakdown voltage and reverse leakage current of the Schottky diodes [60]. SIMS gives an account of total charge carrier concentration in a doped sample unlike electrochemical capacitance-voltage (ECV), which provides only active charge carrier concentration by developing doping profiles at any necessary depth in semiconductor layers. More details on ECV can be found in literature [61, 62].

Instrument

The Wafer Profiler CVP21 from WEP was used for doping profiles measurement in this thesis work as shown in Figure 3.16.

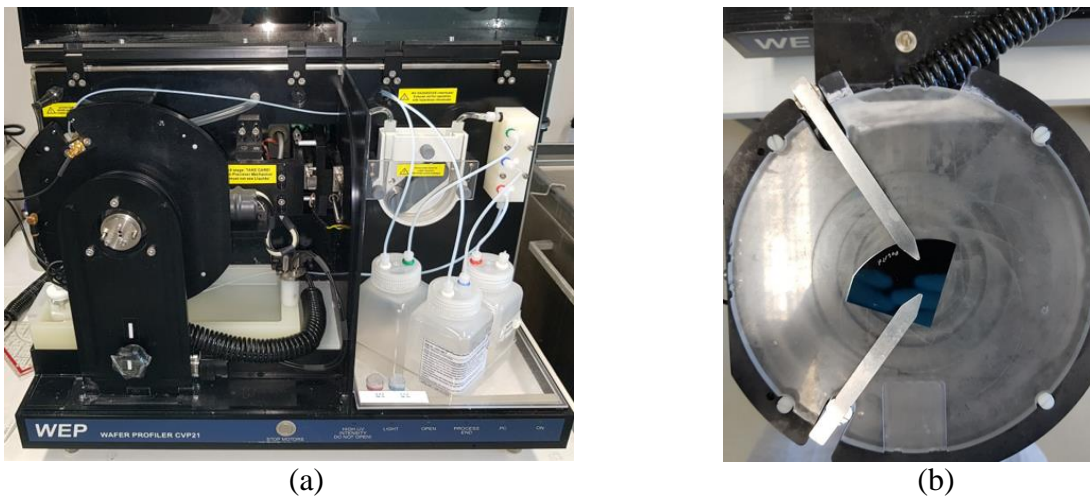


Figure 3.16: Wafer Profiler CVP21 setup at Fraunhofer ISE: (a) wafer profiler, (b) sample holder

Working Principle

The ECV profiler uses an electrolyte-semiconductor Schottky contact to generate a depletion region. The depletion region has no conducting electrons and holes but contains electrically active defects or traps, and ionized donors. The depletion region acts like a capacitor due to its ionized charges. The measurement of capacitance at a constant dc bias voltage provides information of doping and electrically active defect densities. Depth profiling is achieved by electrolytically etching the sample between the capacitance measurements with no depth restriction. The electrochemical cell is schematically illustrated in Figure 3.17. The sample is fixed against a sealing ring which contains an electrolyte and defines the contact area.

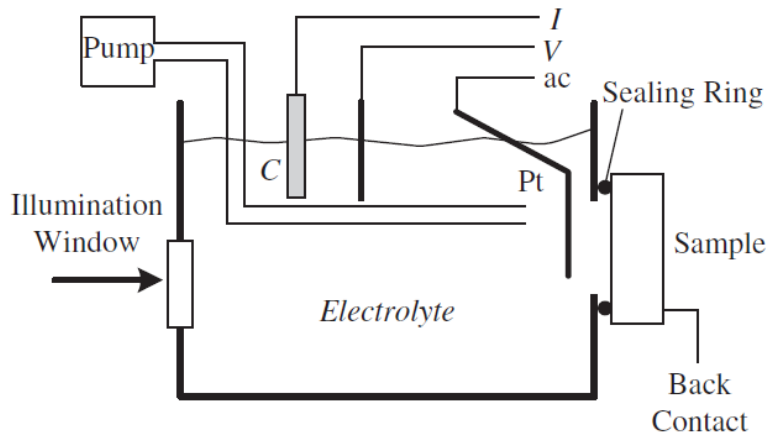


Figure 3.17: Basic setup of electrochemical cell [63]

ECV profiling features two essential and fundamental steps: (I) determination of carrier concentration by measuring the differential capacitance of the Schottky barrier produced at electrolyte/semiconductor interface, (II) controlled removal of material via electrochemical anodic dissolution. These two steps are repeated to obtain variations in the carrier concentration with depth. In case of p -type semiconductor, flow of holes due to forward biased barrier affects the dissolution reaction, whereas the holes in the reverse bias promote dissolution process in an n -type semiconductor. Electrons are absorbed near the surface of the semiconductor, thereby improving dissolution. Typical dissolution rates are $\sim 1 \mu\text{m/h}$. Thickness of the removed material is calculated by integrating dissolution current and applying Faraday's law. Actual depth can be determined by adding this thickness to the local depletion depth [64].

3.4.3 Quasi-Steady-State Photo-Conductance (QSSPC)

Sinton and Cuevas [65, 66] investigated the quasi-steady state photo-conductance method for the first time and has since then been widely used in the photovoltaic industry for solar cell characterization. In this technique, an inductive coil is used to measure the conductivity of a sample from the extra charge carriers, which are generated by illuminating the sample, as shown in Figure 3.18.

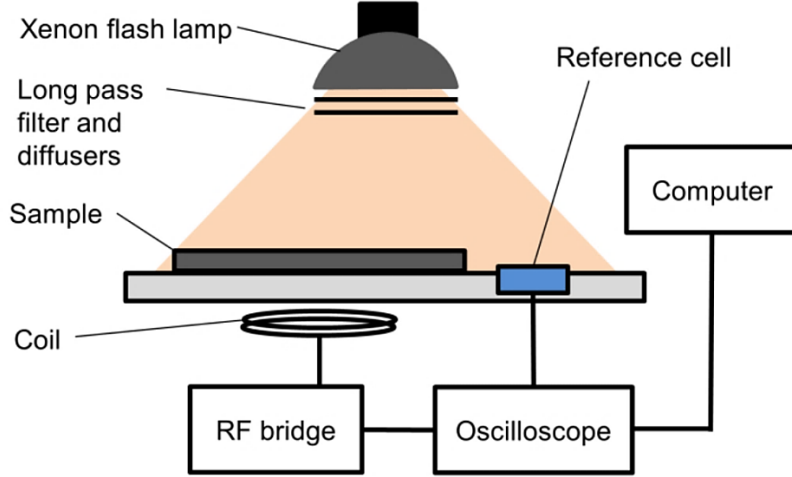


Figure 3.18: Schematics illustration of Sinton WCT-120 inductively coupled setup for QSSPC measurement [67].

The Sinton QSSPC setup uses a Xenon flash as an excitation source to ensure a homogeneous generation throughout the wafer. To measure τ , it is necessary to measure both the injection level and the generation rate of charge carriers in the wafer as a function of time.

The generation rate of charge carriers in Sinton WCT-120 lifetime tester is measured as:

$$G(t) = OC \cdot \frac{I_{\text{ref}}(t)}{qW_{\text{ref}}} \quad (3.5)$$

where I_{ref} is the generated photocurrent which is measured by a small reference cell placed on the sample stage, OC is the optical constant, and q is an elementary charge. Before measurement, the thickness of wafer, OC , and base resistivity values are added to the QSSPC software. The injection level is determined simultaneously from the measured excess conductivity in the sample $\Delta\sigma$ as:

$$\Delta n(t) = \frac{\Delta\sigma(t)}{q(\mu_n + \mu_p)W} \quad (3.6)$$

where μ_n and μ_p are electron and hole mobility, and W is the wafer thickness. Finally, the effective lifetime is at each injection level is calculated by:

$$\tau_{\text{eff}} = \frac{\Delta n(t)}{G(t) - \frac{d\Delta n(t)}{dt}} \quad (3.7)$$

In this thesis, the Sinton WCT-120 equipment is used for the lifetime and recombination parameter measurement of j_0 wafers.

Chapter 4

Results and Discussion

This chapter contains in depth analysis of the results obtained from rheological, optical and electrical characterization techniques. Results obtained from each technique bring us closer to understanding the underlying principles that govern the behavior of different materials utilized during experimentation, such as polymer solution based inks, substrates, etc. The sections presented in this chapter are inter-related with each other as findings of one chapter explain the one following it. The section on 'Rheometry' helps understand the behavior of inks through their response to various stimuli. Analyzing the behavior of inks enables selection of favorable environment, in order to obtain specific behavior needed for good printing. Such environment is created through various external parameters such as temperature, pressure, pulse-voltage, frequency, etc., which are used to develop printing schemes for each ink as explained in the following section on 'Inkjet Printing Process Development'. Tailoring printing schemes enables successful printing of dopant source inks according to our applications. A pre-requisite for improving the overall performance of solar cell structures, developed through printing, is their high electrical performance. Section three on 'Electrical characterization' focuses on electrical properties of the printed structures, subject to different heat treatments.

Through each result in each section we delve more into the finer details of all the processes involved, in order to better engineer the strategies and tailor make the procedures for improving the efficiency of solar cells in general and its constitutive structures in particular.

4.1 Rheometry

4.1.1 Rheological analysis with respect to frequency

To understand the complex nature of dopant source inks used during printing, and their behavior under changing conditions, rheological characterization with respect to frequency, in the wide range of 1-10,000 Hz was carried out at room temperature. However, due to evident dependence of polymer structure (and related intra-chain interactions) on temperature, the change in rheological properties was also analyzed with respect to temperature. Finally, to understand the structural modification inks undergo naturally during storage, properties were analyzed with respect to their aging time as well, explaining the impact of aging on ink behavior. This section explains the results obtained, followed by brief discussions.

4.1.1.1 Reference ink

In order to anticipate the ease or difficulty we could face during printing, we compare the behavior of commercially obtained dopant source inks with a standard/reference ink custom made for LP50 Inkjet printer, which exhibits ideal printing and overall stable ink behavior.

The ideal parametric values for Ink jet printing as obtained using standard ink are as tabulated below.

Table 4.1: Standard (reference) ink rheological parameters.

Properties	Value
Complex viscosity (η^*)	2-20 mPa.s
Elastic modulus (G')	≤ 10 Pa
Viscous modulus (G'')	≥ 1 Pa (linear growth)

The evolution of the above-mentioned parameters, which are further described below, with respect to frequency is shown in Figure 4.1.

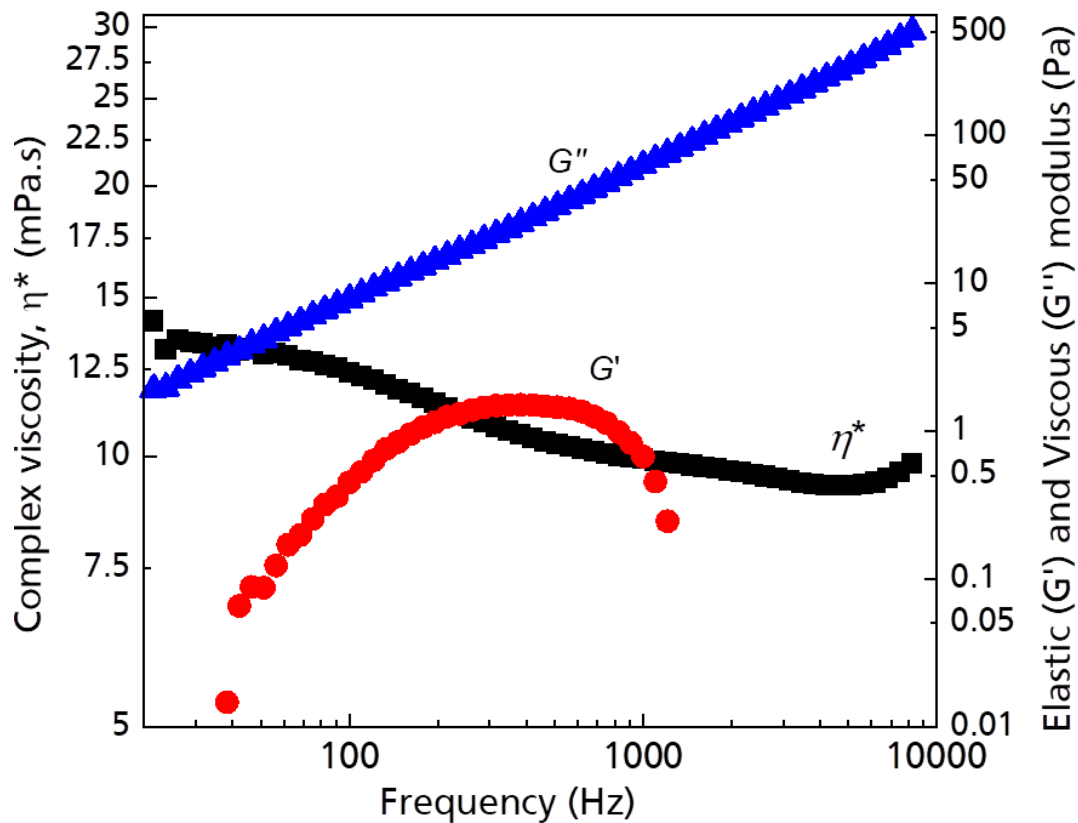


Figure 4.1: Evolution of complex viscosity, viscous and elastic components of complex modulus with respect to frequency, for the reference ink.

Complex viscosity (η^*)

The viscosity value lies within 2-20 mPa.s range throughout the entire frequency range. The values do not remain constant as is evident from the curve but such slight variations do not demand any drastic measure to be taken externally during printing. The ink behavior is apparently mostly Newtonian overall with slight non-Newtonian nature exhibited over ~200 Hz - 400 Hz. The curves produced were smooth, due to tailored composition of the ink, implying its stability over wide ranges of external parameters. There are two transitions visible near ~300 Hz and ~ 800 Hz, the second being less prominent. Possible reasons for such transitions are explained later in the section.

Elastic component of complex modulus (G')

At lower frequencies we do not witness presence of elastic modulus which starts to appear only after ~ 50 Hz, then increases up to a maximum at ~ 400 Hz and again reduces as frequency keeps on increasing. It thus signifies the presence of a lower limit-threshold frequency to establish an elastic response and an upper limit, beyond which, the elasticity reduces to negligible values (not included in the figure). The Gaussian type curve of the elastic modulus coincides with the beginning and end of the non-Newtonian behavior (the transition phase) of the ink. However, the value of G' always remains less than 1.5 Pa.

Viscous component of complex modulus (G'')

The viscous modulus can be measured right from the beginning, due to the inherent fluid nature of the ink. On increasing the frequency, the viscous modulus increases linearly in a straight line fashion which is typical of a viscoelastic material. It doesn't show any peculiarity with the change in frequency, temperature or aging time as explained later.

Reference ink obeys Maxwell's model ideally, based on the slope of its modulus components in low frequency range:

- G' – slope – 2
- G'' – slope – 0.937 (~1)

4.1.1.2 Rheometry of Dopant source inks- Ink jet relevance

Rheological inspection of various inks, used as dopant sources over Silicon wafers or thin films, provided in depth knowledge about their rheology and its role in jetting performance/printability of inks. Understanding their varied behavior enabled anticipation of the relevant printing problems specific to each ink. According to their composition, we divided our inks into three batches, each containing Phosphorus based (P-inks) and Boron based (B-inks) explained in Chapter 3. Results explained in this section are for fresh inks, as received. It must be noted that the inks, as received, had already been aged for some time. The details of the number of P and B based inks and their age on their first use are mentioned in Table 3.1.

Complex Viscosity (η^* , mPa.s)

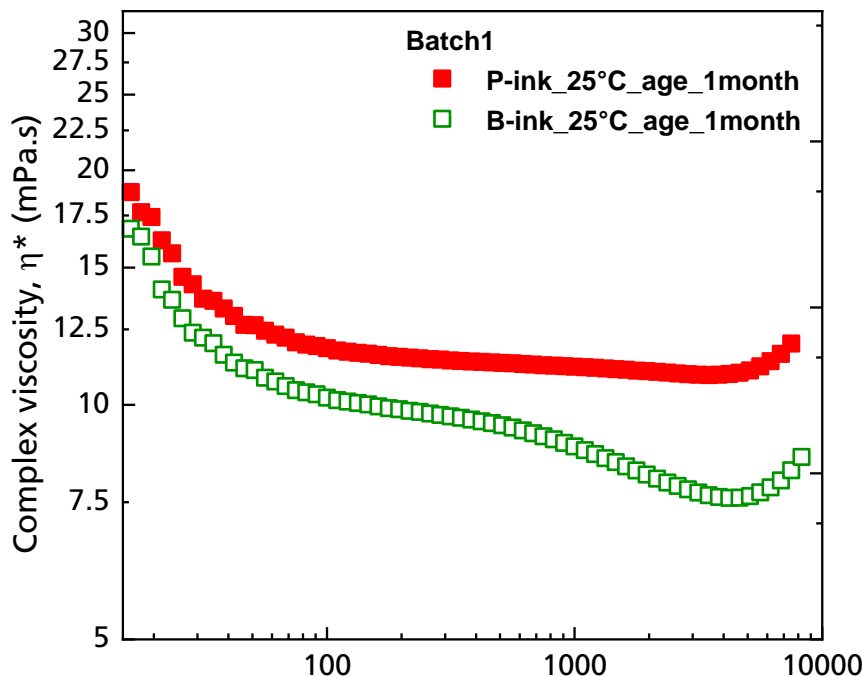
- **Batch 1**

From Figure 4.2 (a) we can observe that organometallic (Boro- and Phospho-silicate) solution based inks from Batch 1 exhibit mostly Newtonian and near ideal behavior over the inkjet printing frequency range of 1000 Hz – 10,000 Hz, with a degree of non-Newtonian behavior for B-ink at higher frequencies. The viscosity values of both the inks lie in the Ink jet required range of 2-20 mPa.s. More stable behavior was exhibited by P-ink than B-ink, as evident from viscosity curves. At lower frequencies, the viscosity of P-ink is high - ~18 mPa.s. It reduces continuously until attaining a constant value of 10 mPa.s - equilibrium viscosity at higher frequencies. B-ink exhibits a complex behavior and shows two transition phases. This represents the attainment of final flow behavior typical of a polymer.

- **Batch 2**

Viscosity ranges of Batch 2 (Figure 4.2 (b)) inks vary over a huge range, especially for P-inks. For P-ink 2, viscosity changes from 40 mPa.s to 1 mPa.s - highly non-Newtonian overall, while for P-ink 1, it changes from 25 to 4 mPa.s, show a plateau at higher frequencies (> 100 Hz). P-inks, although differing only in their age (as mentioned in Table 4.2) and 'P%' (concentration of Phosphorus atoms) have same formulation of the base polymer. P-ink 1 is two months older than P-ink 2.

(a)



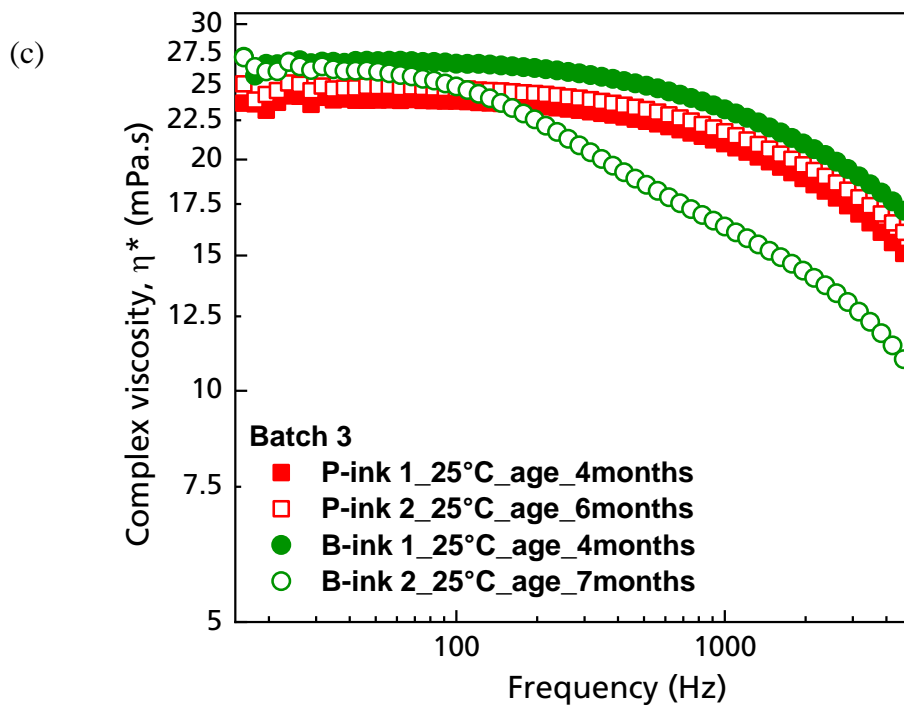
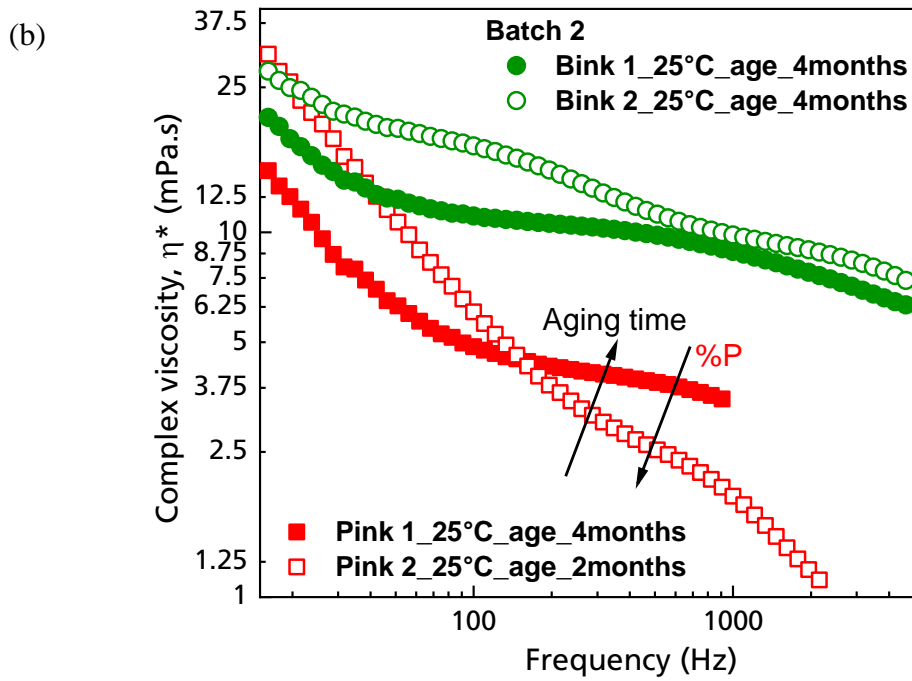


Figure 4.2: Complex viscosity measurement of fresh (as received) dopant source inks with respect to frequency for: a) Batch 1, b) Batch 2 and c) Batch 3 Phosphorus and Boron inks.

P-ink 1, initially showing a negative slope, attains constancy after ~100Hz. P-ink 2 shows a constant negative slope with a small plateau around 200-500 Hz. Further than 500 Hz, the viscosity again reduces tending towards zero. For Boron-inks (B-inks), the viscosity is highly unstable, especially for B-ink 2, varying from 40 to 5 mPa.s. B-ink 1 shows a prominent plateau up to ~1000 Hz followed by a reducing trend while B-ink 2 shows alternations between two plateaus (around 100 Hz and 1000 Hz respectively) and two transitions ensuing them. Both boron based inks of Batch 2 are aged for two months, however, their storage conditions are different (~5°C) and dry for B-ink 1 and room temperature and dry for B-ink 2).

- **Batch 3**

Batch 3 inks (Figure 4.2 (c)) exhibit relatively stable rheological parameters. All viscosity curves show negative slope - reduction at higher frequencies, implying the pre-dominant viscosity to be 'upper Newtonian'. Except for B-ink 2, which shows early transition from Newtonian to non-Newtonian behavior, all other inks follow uniform trend, exhibiting viscosity values higher than the desired ink jet range, implying requirement of higher actuation voltages. Since the workable ink jet frequency lies within 1000-10000 Hz range (usually above and around 2 kHz, [68]), it coincides with the viscosity transition phase from highly coiled structures, which allow to anticipate complex response during printing. P-ink 1 & 2 and B-ink 1 show overlap in their viscosity data and trend, with a small upward shift for B-ink 1. B-ink 2 shows change of slope two times near 100 Hz and 1000 Hz respectively.

Viscous component of modulus (G'' , Pa)

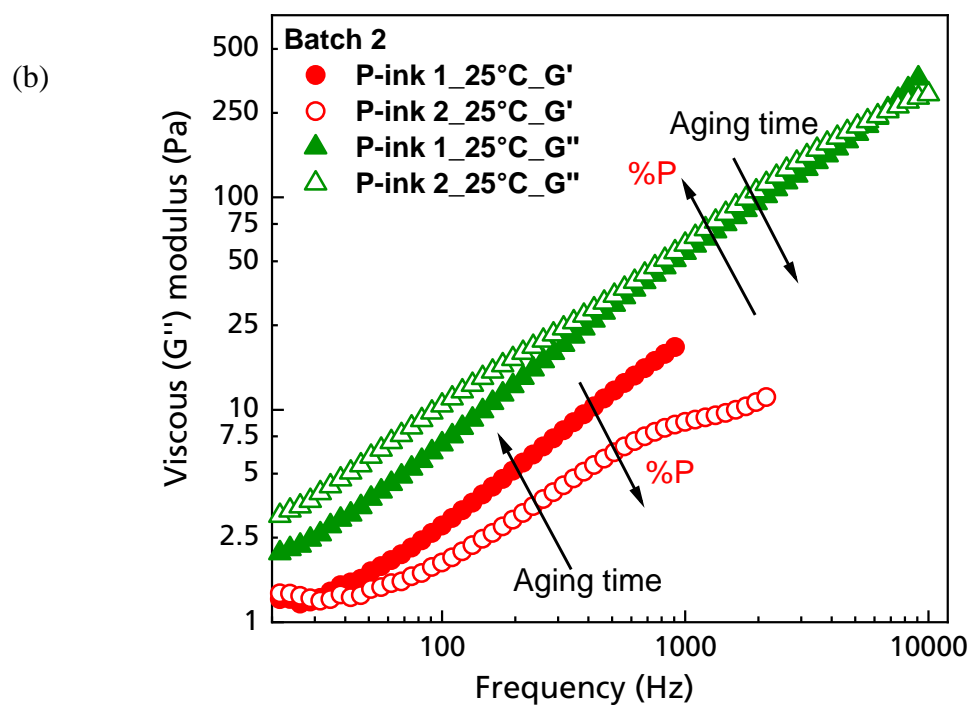
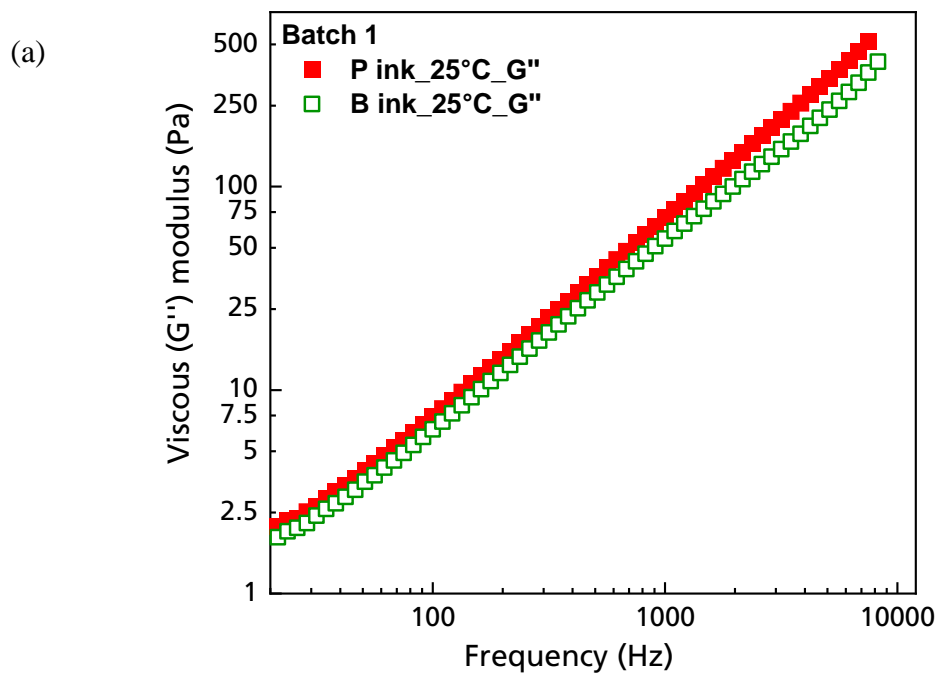
Viscous modulus, as can be observed from Figure 4.3, more or less remains same for all the inks, showing linear behavior with the curves appearing from least frequency values.

- **Batch 1**

Batch 1 inks, both Phosphorus and Boron based, show a stable viscous behavior, thus ideal fluid nature. The slope for P-ink 1 is 0.94 and that for B-ink is 0.89, which is very close to the ideal Maxwell fluid slope of 1 for G'' . Both the inks reach a maximum of ~500 Pa at 10,000 Hz, with B-ink showing slight deviation from straight line path after 1000Hz, which is also the onset of deviation of its viscosity curve, as mentioned in the preceding section.

- **Batch 2**

The viscous modulus for Phosphorus based inks, the curves show constancy for initial few decades and linear growth thereafter. The rise in viscous modulus is not as sharp as for other inks. The curve for P-ink 1 is 0.76 while that of P-ink 2 is 0.45 as against slope of 1 for Maxwellian fluids. P-ink 1 shows a constant increasing trend, while P-ink 2 with a smaller slope tends to even smaller change at higher frequencies (after 1000 Hz).



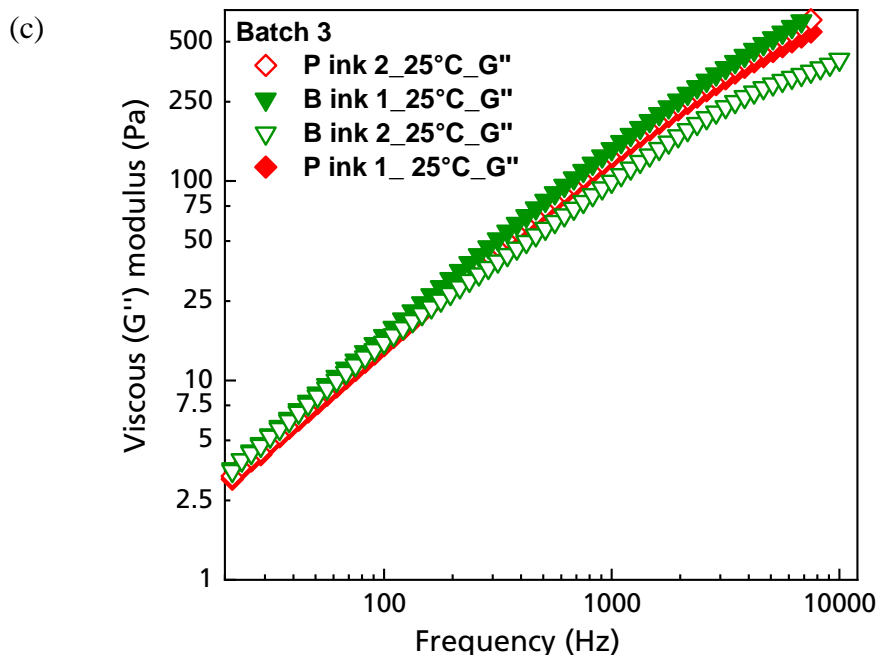


Figure 4.3: Evolution of viscous modulus with respect to frequency for fresh (as received) dopant source inks for a) Batch 1, b) Batch 2 and c) Batch 3.

B-ink 1, shows slight deviation from a slope of 0.94 (at lower frequencies) at 1000 Hz and along with presence of a small plateau while B-ink 2 with 0.79 slope at lower frequencies exhibits two plateaus after 100 Hz and 1000 Hz respectively, exactly where the trends change for viscosity.

- **Batch 3**

For Batch 3, the resinous inks show quite stable viscous modulus growth, increasing linearly with frequency, except for B-ink 2, which shows an early departure from the trend as it did for viscosity. However, all the inks attain a maximum of ~500 Pa at maximum frequency of 10,000 Hz.

Elastic component of complex modulus (G', Pa)

- **Batch 1**

Elastic modulus of all the inks, as received, exhibited diverse trends anticipating diverse response of the inks on application of shear stress (through nozzle, during printing), given the importance of elastic modulus for printing. Ideal characteristics were only exhibited by Batch 1, P-ink, with values ≤ 1 Pa resulting in smooth printing operations. The value of G' for P-ink maintains constancy of value ~ 0.5 Pa. The value reduces sharply after ~ 200 Hz, to negligible values. These characteristics are very similar to the reference ink in terms of its maximum values

and trend of evolution of curves, as can be seen in Figure 4.1. Characteristics were near ideal for viscosity of B-ink as well but the elastic component, which is constant initially shows an elevation after 200 Hz, reaching its peak of 1.3 Pa at ~1000 Hz followed by a sharp steep negative slope reaching negligible values.

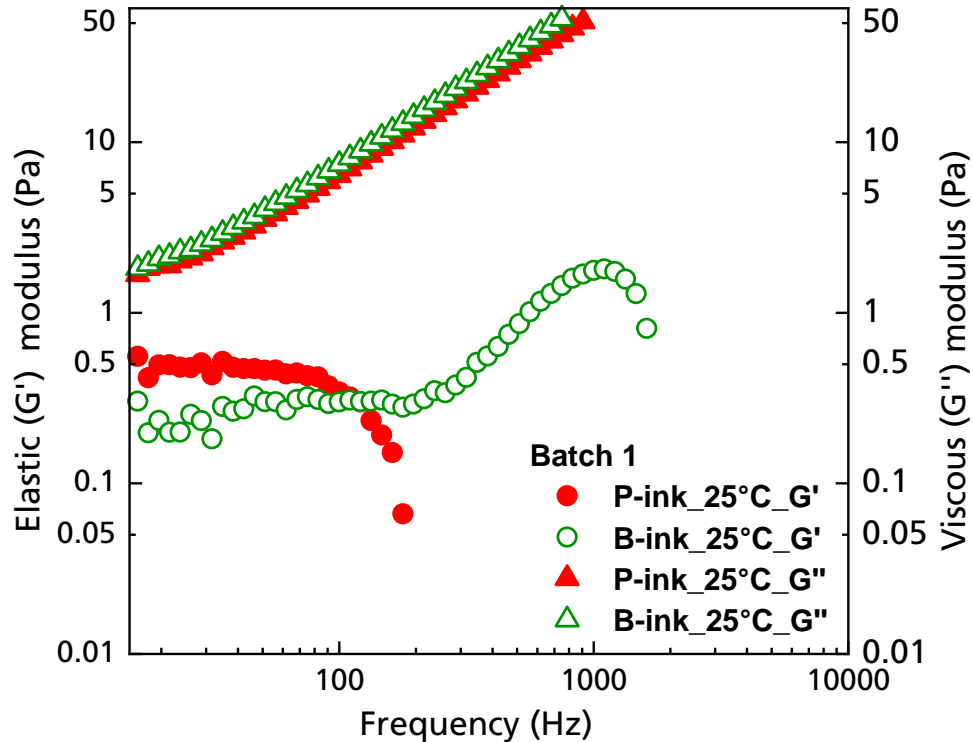


Figure 4.4: Evolution of Elastic (G') and Viscous (G'') components of complex modulus measurement with respect to frequency for Batch 1.

- **Batch 2**

Elastic modulus of Batch 2 inks exhibited peculiar behaviour. P-ink 1 and P-ink 2 exhibited different rheological behaviour similar to their widely different printing behaviour. Both the Phosphorus based inks show initial constant elastic modulus which increase for higher frequencies. P-ink 1 shows change in its elasticity from 1Pa after ~300 Hz and increases linearly thereafter. P-ink 2, however, starting from a constant value of 2.6 Pa, increases from 300Hz to 1200 Hz to attain a final value of ~10 Pa, which is maintained thereafter. The contrasting feature in case of P-ink 2 is the constancy of elasticity maintained while viscosity exhibits changing behaviour and a change in elasticity while viscosity shows plateau. The trends can be observed from Figure 4.5 and 4.2 (b).

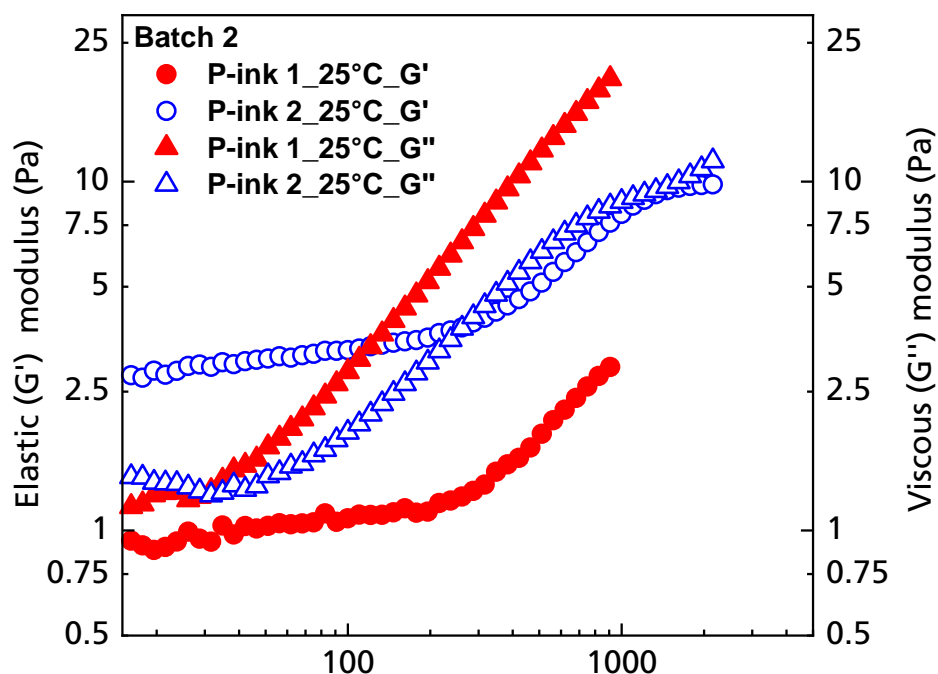


Figure 4.5: Evolution of Elastic (G') and Viscous (G'') components of complex modulus with respect to frequency for P-inks of Batch 2.

Boron inks of Batch 2, also exhibit strong polymer like interactions hence the strong transitions over frequency. B-ink 1, like P-ink 1, maintains its initial constant value for elastic modulus until ~ 200 Hz, after which it starts increasing (in this range viscosity starts decreasing), attains a peak value of 20 Pa at ~ 3000 Hz followed by a steep decline to negligible values. The onset of sharp decline of G' aligns with the second transition of viscosity towards final positive slope.

On the other hand, B-ink 2, like P-ink 2 deviates from constancy of G' as viscosity attains a plateau and shown by its flat curve. The differentiating feature in this case is its non-decreasing trend until 10,000 Hz.

During printing, B-ink 1, showed delayed nozzle response on purging. Similar to P-ink 1, on increasing the purging time to 5 s, we obtain a huge drop a few seconds after purging. On increasing the temperature of nozzle head to 40°C , there was again failure of purging (Impact of temperature on rheology has been discussed in the following section).

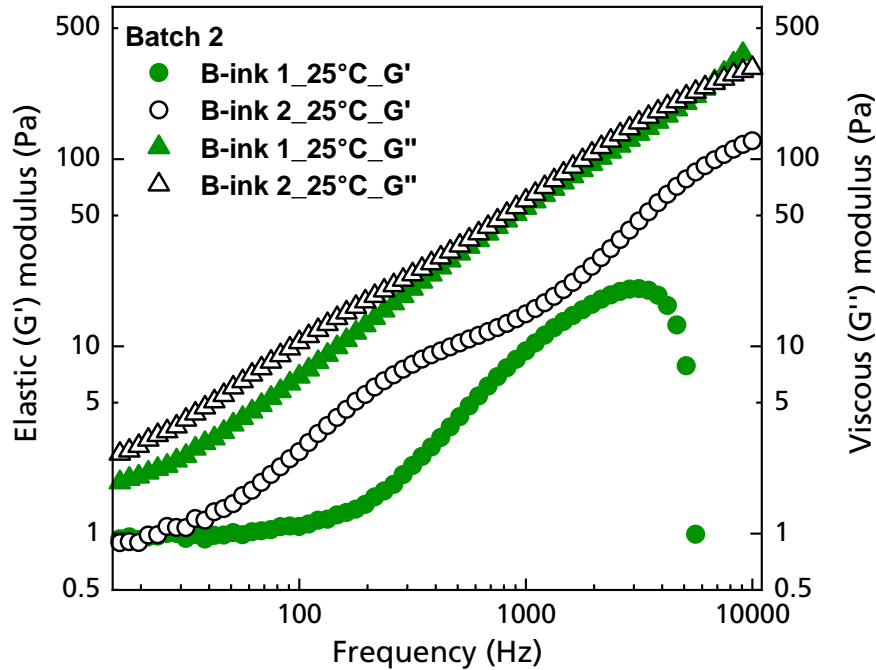


Figure 4.6: Evolution of Elastic (G') and Viscous (G'') components of complex modulus measurement with respect to frequency for B-inks of Batch 2.

- **Batch 3**

These inks, made up of viscous resin base, produced smooth rheological results obeying Maxwell's model in the frequency range 100 Hz – 5000 Hz, as was concluded from their moduli slopes for low frequencies.

- P ink-
 - G' – slope – 2.29
 - G'' – slope – 0.97
- B ink-
 - G' – slope – 2.34
 - G'' – slope – 0.93

G' values of both the inks are extremely high according to the requirements of inkjet printer. The values show a scatter below 100 Hz and then curve starts to appear with positive values starting from below 5 Pa, increasing at a decreasing rate and going up to a maximum of ~200 Pa at the upper end of frequency. The trends can be seen in Figure 4.7. All the inks from Batch 3, however, failed to form proper individual droplet at actuation voltages as high as 60V and with print-head temperatures taken to 55⁰C under pulsed waveform and no signs of jetting and firing. After a few seconds of purging, a large drop came out before retracing their way back into the cartridge. Same was the behavior of all inks belonging to Batch 3.

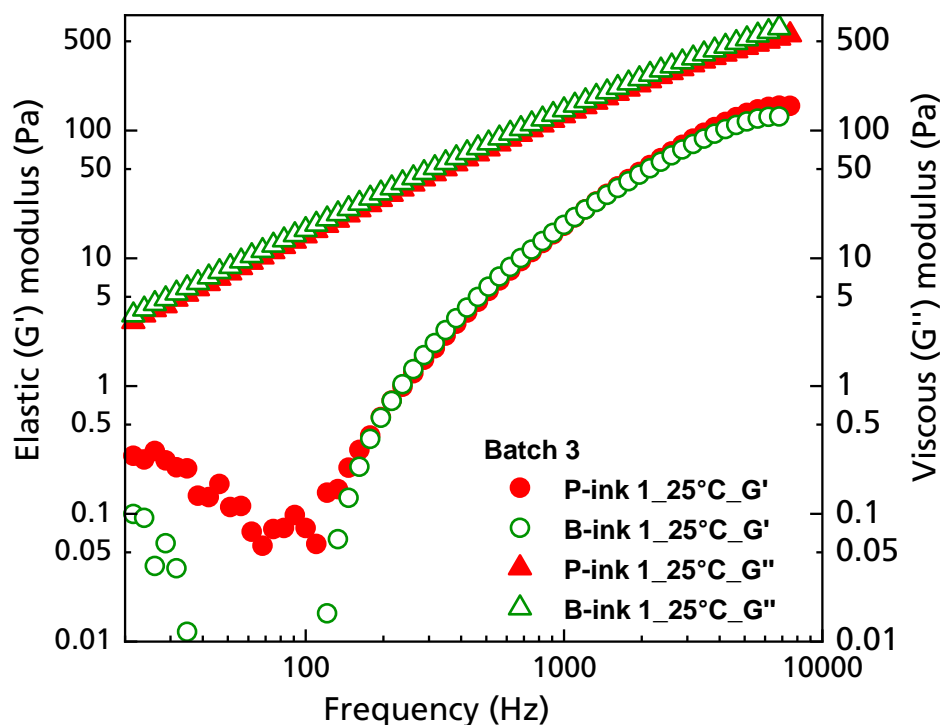


Figure 4.7: Evolution of Elastic (G') and Viscous (G'') components of complex modulus measurement with respect to frequency for highly resinous P and B-inks of Batch 3.

Discussion

Rheological properties, as discussed in Chapter 2, play fundamental role in determining printability of the inks. Polymer solutions, which inherently exhibit viscoelasticity, enable workability in a limited range of input (frequency/shear stress). The properties, although can be changed to a certain extent by adjusting the external parameters, mainly temperature and pressure (through actuation voltage), do not always show desired outcomes. The complex change often exhibited by the dopant source inks on changing external parameters is representative of their complex nature and structure and the ensuing complex interactions. In addition, nearness to critical values of the internal parameters (like molecular weight and cross-linking density) also determines the behavior of inks, which is thus highly susceptible to transitions. Criticality promotes further complex changes on changing the external parameters. Composition of the inks, therefore, dictates the stability of their properties and how smooth or complex their transition would be on changing the external parameters. For all the inks, which were analyzed, the concentration is above 5% on an average. A categorical distinction between ‘concentrated’ and ‘dilute’ solutions can be only found using critical concentration of a solution (c^*) and entanglement concentration (c_e), [69] which is out of scope of this thesis. However, above 5% solutions (solute concentration) fall into the category of concentrated solutions as has been

declared in literature [70]. Therefore, the dopant source inks used in this work are also treated as concentrated polymer solutions and all the dynamics of a concentrated solution (as described in Chapter 2) are considered to explain different results and inconsistencies as obtained in data. However, since exact composition of the inks remains unknown, some conclusions are based on comparative analysis with established literature. Moreover, although the data is for complex inks, the structures of which aren't defined, Cox-Merz rule is also in this thesis. Some results established in literature for steady state shear experiments have been extended to explain the results obtained for dopant source inks with respect to angular frequency. The printing experiences were convincing enough to consider that the complex data may possess similar trend as for steady state conditions.

4.1.1.3 Reference ink

Complex viscosity (η^*)

The viscosity value requirement for inkjet printing, as has been mentioned in Table 4.1 should lie within 2-20 mPa.s. However, presence of Newtonian nature of viscosity does not imply any particular printing behavior. Contrarily, as is proven in literature, presence of non-Newtonian nature enhances the printing efficiency due to the elasticity associated with it [71].

As observed in Figure 4.1, the viscosity does not remain constant for the reference ink, tailor made for LP50 inkjet printer. This confirms the established theory that viscosity alone does not play a direct role in determining the jettability/firing of the ink, but only in determining the actuation voltage and the quality of the prints obtained. The fluids showing low values of low-shear rate viscosity require low actuation voltages while at the same time their ligament extends almost linearly with time until its point of detachment. As opposed to this, the fluids, which require high actuation voltages, are the ones with higher viscosity values and show rapid deceleration of jet and later detachment [72]. For our applications, actuation voltage, however does affect the outcome as we aim to develop IBC, TOPCon solar cells, etc. which have fine structures with feature size in the range of micrometers. A higher actuation voltage implies a larger drop volume, which prevents the development of fine structures required for specific solar cell contact applications in this cases.

From the reference ink behavior, we can understand the response of a typical polymer towards stress, in terms of its viscosity. Reference ink is mostly Newtonian overall with slight non-Newtonian behavior exhibited over ~200 Hz - 400 Hz, which can be related to its transition from η_0 to η_∞ indicating transition from an initial highly coiled structure to a final equilibrium linear structure. The trend of change of viscosity of a polymer with respect to shear rate (or frequency) can be visualized from Figure 4.8. Due to the highly coiled structure of a polymer, resistance to shear stresses and hence its resistance to flow is higher. The viscosity in this range is known as upper Newtonian viscosity or Zero shear plateau, η_0 . As the stress, increases the polymer

branches are stretched and tend to align along the direction of flow, which reduces the viscosity continuously until the entire polymer chains are aligned and a constant, lower (or equilibrium) Newtonian viscosity or infinite shear plateau, η_{∞} , is attained. The phase, during which the chains, while aligning themselves show Non-Newtonian viscous behavior, represents the transition wherein shear stress and shear strain show power law obedience on viscosity.

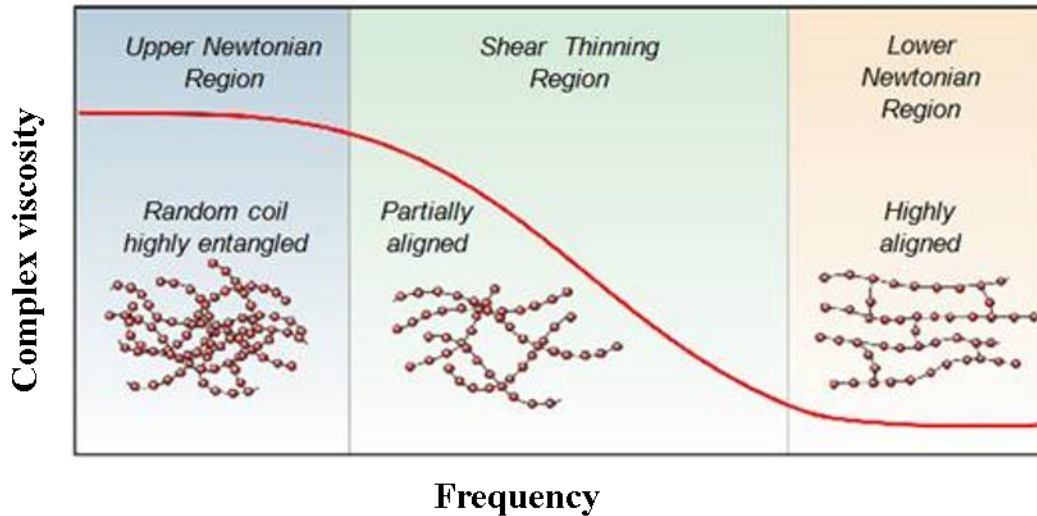


Figure 4.8: Transition of viscosity due to change in the structure of polymer [73].

Elastic and Viscous components of modulus (G' & G'')

The presence of elastic component of complex modulus confirms the viscoelastic nature of the ink, which plays a dominant role in determining the drop formation and ligament breakup [74]. As expected, at lower frequencies we do not witness the presence of elastic modulus, as apparent in Figure 4.1, only viscous modulus (G'') is produced. As frequency increases we witness presence of elastic modulus which increases up to a maximum and then again reduces at very high frequency. Elastic modulus is helpful in the drop formation but when present in an optimized range. Too high an elastic modulus results in failure of detachment of droplets and too low modulus results in the failure of drop formation at the first place, as was also experienced during printing of various dopant source inks, described in the subsequent sections. As has been observed, a value of ≤ 10 Pa supports good drop formation and printing with minimum nozzle cloggings, lesser tails and satellites. Typical trend of visco-elastic material behaviour in terms of their elastic and viscous modulus can be observed from Figure 4.9. The behaviour obeys Maxwell's model at low frequencies, with the slopes given in the figure, as was also observed in many dopant source inks. Overall, the model is a combination of Maxwell's model and Kelvin-Voigt's model (which is also a simple combination of spring and a dashpot but attached in parallel).

The viscous modulus exists from beginning, due to the inherent fluid nature of inks. On increasing the frequency, the viscous modulus increases linearly; a typical representation of the energy dissipative nature of a fluid. It doesn't show any peculiarity with the change in frequency, temperature, or even specific composition (in most cases), as is explained in further sections.

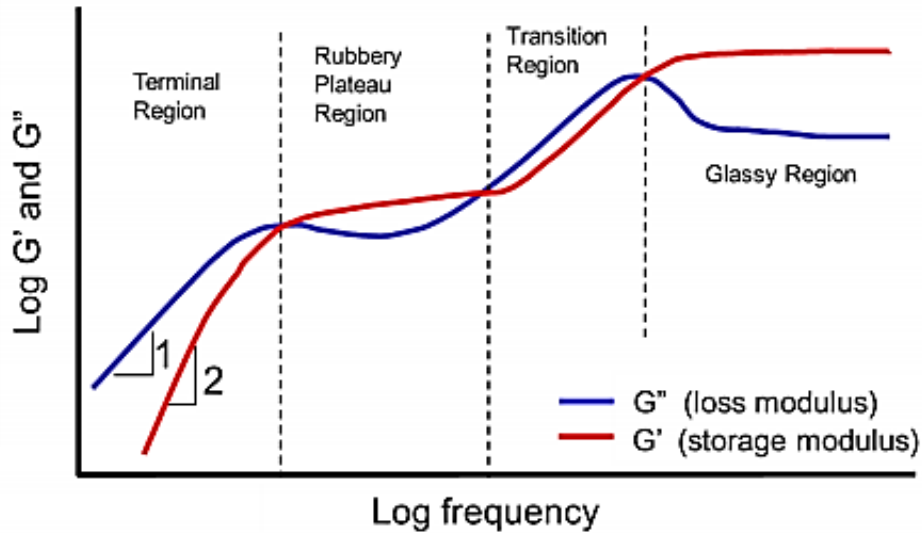


Figure 4.9: A typical viscoelastic spectrum for an entangled viscoelastic spectrum [28].

4.1.1.4 Rheometry of dopant source- Ink jet relevance

Complex Viscosity (η^* , mPa.s)

The nature of viscosity, as exhibited by dopant source inks, is very different from the reference ink thus anticipating requirement of different printing parameters. As discussed earlier, although the value of viscosity plays an important role in determining the actuation voltage required, it does not play as dominating role in controlling the jetting behavior or firing of the inks. Given the small nozzle orifice diameter (21.5 μm) diverse mechanisms become prevalent in determining ink dynamics. Besides rheological properties, the surface tension of the ink and interaction with nozzle surfaces also play an equally important role, thus making it hard to exactly predict the ink behavior solely based on rheology.

Viscosity behavior of Batch 1 inks, being similar to reference ink, holds the same reasoning. However, there are some peculiarities in all the curves obtained so far. The data, especially the scattered data obtained at low and high frequencies is highly likely possible due to the limitations of measurement through rheometer. At high frequencies, the unconventional data points can emerge due to inertia effect of the device or of the material (to take care of which the knowledge of density of material is important). This limits our range of data interpretation extends anonymity for the data obtained towards the higher end of the frequency ranges.

The higher viscosity values of Batch 3 inks and their subsequent failure to purge eventually is again implies the fact that only viscosity is not of much significance for better printability. The possible explanation in case of Batch 3 inks too lies in the possibility of high amount of entanglements given that the inks are resin based. As from Figure 4.2 (c) we are able to see a downward slope of η^* at higher frequencies, which can be representative of transition from upper Newtonian to a lower Newtonian viscosity value. However, the density effects of the resins might also be responsible for such change due to role of inertia effect during measurement at high frequencies, as explained in the preceding section.

Viscous component of complex modulus (G'' , Pa)

Viscous modulus, as can be observed from Figure 4.3, shows more or less same trend for all the inks, i.e. linear growth. This observation also makes clear the relatively limited importance of the role of G'' in printability. For example for both P- and B-inks of Batch 1, G'' show a stable viscous behaviour. However, P-ink exhibited smooth printing behaviour with minimal clogging, while B-ink exhibited a lot of nozzle clogging and unstable behaviour.

Similarly we observe for inks of Batch 2, of which we could obtain successful good print only for P-ink 2. The viscous modulus is almost linear for Boron based inks, while for Phosphorus based inks, the curves show initial constancy and later linearity of the curves. The limitation of data points upto 1000 Hz can be attributed to strain induced crystallization that was observed for both the inks (P-ink 1 & 2). As has been established by James et al [75], the induction of vortical flow (which can be due to sinusoidal input) at both the rheometer plate as well at the nozzle of printer, results in development of polymeric crystals with lengths of several millimeters. Although this effect is prevalent in concentrated polymer solutions, it has been found in case of polymers with concentration as low as 20 ppm. The strain induction as attributed to secondary motion can produce crystals in seconds and the crystals may be strong enough to block the flow completely. Flow induced crystallization is a fundamental non-equilibrium thermodynamical problem. As we observe from Figure 4.5, the range of data obtained is higher for P-ink 2 than for P-ink 1.

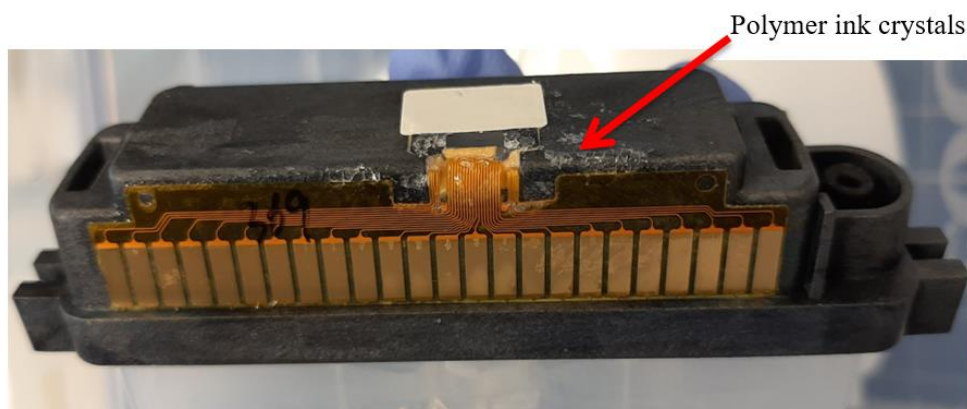


Figure 4.10: Polymer ink (P-ink 1 & 2, Batch 2) crystals around nozzle area of cartridge.

The deposition of crystals around the nozzle area as observed during printing sessions can be seen in Figure 4.13. Similar crystals were found on the rheometer plate after frequency sweep measurements. Therefore, generation of such crystals can highly likely hinder the propagation of dynamic input and hence fail to produce output signal. No such feature was observed for B-inks of same batch.

Elastic component of complex modulus (G' , Pa)

- **Batch 1**

Elastic component of complex modulus value always being close to ~ 1 Pa is an ideal characteristic that helps drop formation without tails and satellites thus enabling ideal prints. As from Figure 4.4, we observe zero slope for G' at low frequencies for both the inks which can be interpreted as an unchanged polymer structure maintained by the ink until frequency reaches a threshold value.

In case of B-ink the elastic component shows an increase at higher frequencies and achieves maximum at 1000 Hz. This can be related to resistance of the polymer to change its structure, which ends as frequency increases further. Implication might be drawn of either breakage of bonds at extremely high frequency or straightening of all the coiled structure to linear chains. Although the value of the elastic modulus does not exceed 1.3 Pa, the ink exhibited excessive clogging and dewetting over the silicon wafer (Cz and FZ) substrates implying high surface tension and poor substrate-ink adhesion. As a result although the rheology of B-ink was favourable, other molecular interactions rendered the ink highly unstable during printing.

- **Batch 2**

As can be seen in Figure 4.5, both P-inks show similar rheological characteristics at low frequencies. As the frequency increases and we reach the inkjet range (from 100 Hz to 10,000 Hz) the response of the inks gets different and so does the trend of their rheological parameters, particularly around and after 1000 Hz. Like P_ink 2, P-ink 1 also showed ideal droplet production without tails and satellites but excessive clogging during printing. P-ink 2, on the other hand produced smooth printing result with minimal clogging. The basic difference in two inks lies in their Phosphorus concentration, with P-ink 1 having one magnitude less concentration of P atoms. This can have many implications on the rheology and printability of the ink. Since, the base polymer (silicate) amount is the same for both inks, lower % P means a higher fraction of polymer base. The dynamic shearing conditions during printing and the small size of orifice of the nozzle are both conducive to the formation of secondary entanglements, rendering the molecules too big to leave the nozzles. As according to literature, at such dimensions, shear rate induced gelation can be observed, due to particle bridging, even if the

particle size is smaller than the nozzle diameter by a unit of magnitude [76]. However, particle bridging (which in case of P-ink 1 can be caused due to secondary entanglements) is only one of many possible reasons for nozzle clogging. Another reason can also be strain-induced crystallization, as explained under the section for viscous modulus. Moreover, as can be seen from Figure 4.6, the trend of change of elastic modulus for P-ink 1 does not show negative slope but instead continues to increase. This further endorses the possibility of role of secondary entanglements in elastic nature of polymers. The details regarding the role of secondary entanglements in concentrated polymeric solutions have been described in literature [35].

Given the presence of non-zero values of elastic modulus at low frequencies, the delayed response of the ink to purging (stress input), excessive clogged nozzles during printing (except for P-ink 2), it can be deduced that the inks from Batch 2 obey Maxwell's retarded model explained in Chapter 2.

Similar to Phosphorus inks, Boron based inks of Batch 2 also exhibit peculiarities, such as

- Unstable viscosity changes
- Curve of viscous modulus increasing with a slope less than unity
- Non-zero initial elastic modulus

These observations offer a fair reasoning to poor printing performance of the inks. Marked difference between the two Boron based inks was observed during purging. For B-ink 1, as can be seen in Figure 4.6, the elasticity shows a reducing trend, which implies straightening inclination of the polymer chains at higher shear strain values. This can be a possible explanation for delayed nozzle response at actuation voltages as high as 50 V. On the contrary, as for B-ink 2, the trend of the elastic modulus is non-decreasing which implies the tendency of formation of more entanglements. This implies high tendency of the polymeric ink towards entanglement formation, which thus resists flow of ink as explained by Maxwell's retarded model. Due to such behavior, possibly there was no response during purging to actuation voltages as high as 60V for purging time as high as 5s.

- **Batch 3**

Curves for elasticity show presence of scattered data at low frequencies while a prominent trend is visible after ~100 Hz as can be seen in Figure 4.7. This can be due to device noise. However, the high elasticity of both the inks offers a reasonable explanation for failure of drop production during jetting, at actuation voltages as high as 60 V and nozzle head temperatures to 55°C under pulsed waveform. Under such extreme conditions, droplets were produced only during purging, but not during jetting. On capturing the droplet formation through drop watcher, as shown in Figure 4.14, the dominant role played by elasticity of the ink was evident. After a delayed

response to strong purging conditions, a big droplet of ink was produced which, after a few seconds started to retrace its way back into the nozzle completely, as shown in Figure 4.11.

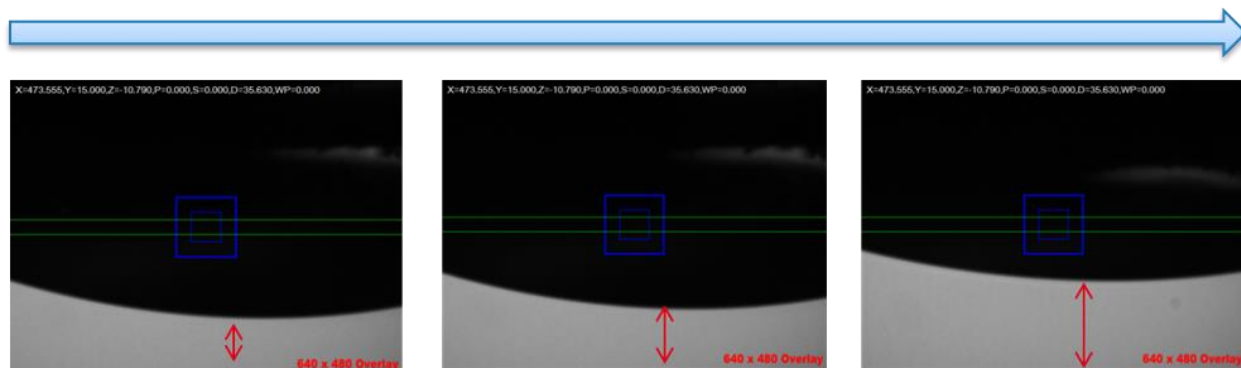


Figure 4.11: Resinous inks of Batch 3 retracing into the nozzle after being subjected to 60V, 5s for purging.

Another peculiar feature exhibited by the inks was the failure to purge subsequently, even when subject to extreme conditions. Thus, the only success was the first purge, after which the ink was resistant to come out of the nozzle. To ensure that the nozzles, with diameter of $20\mu\text{m}$ were not too small for seemingly large polymer molecules, filtration was carried out using filters of the same size ($20\mu\text{m}$), inside glovebox, as shown in Figure 4.12. During filtration, the movement of fluid did not show any resistance, thus ruling out the possibility of size of nozzles being a limitation. To rule out the possibility of purging pressure of LP50 Inkjet printer being a limitation to the printability, manual purging was also carried out. The ink showed similar behavior as during printing. After showing initial signs of purging, it failed to purge on further application of high manual pressure. A large drop (produced on first purge), more than half volume of which retraced back through the nozzles was followed by smears around the adhesive over the nozzle plate, as shown in Figure 4.13.

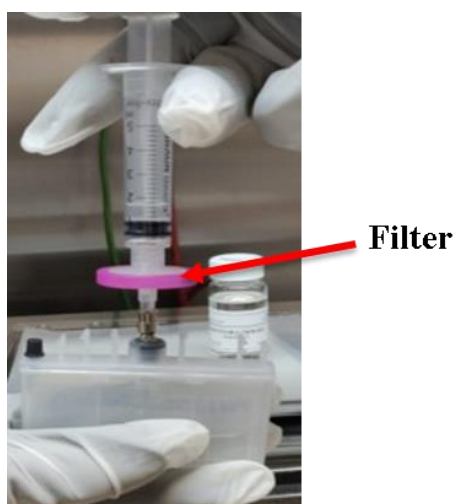


Figure 4.12: Filtration B-ink 1 of Batch 2, through a $20\mu\text{m}$ filter.

Therefore, despite subjecting the inks from Batch 3 to severe conditions, rheological characteristics, especially high elasticity together with surface interactions at the nozzles, the rheology of these inks was too unfavorable to enable successful droplet production.

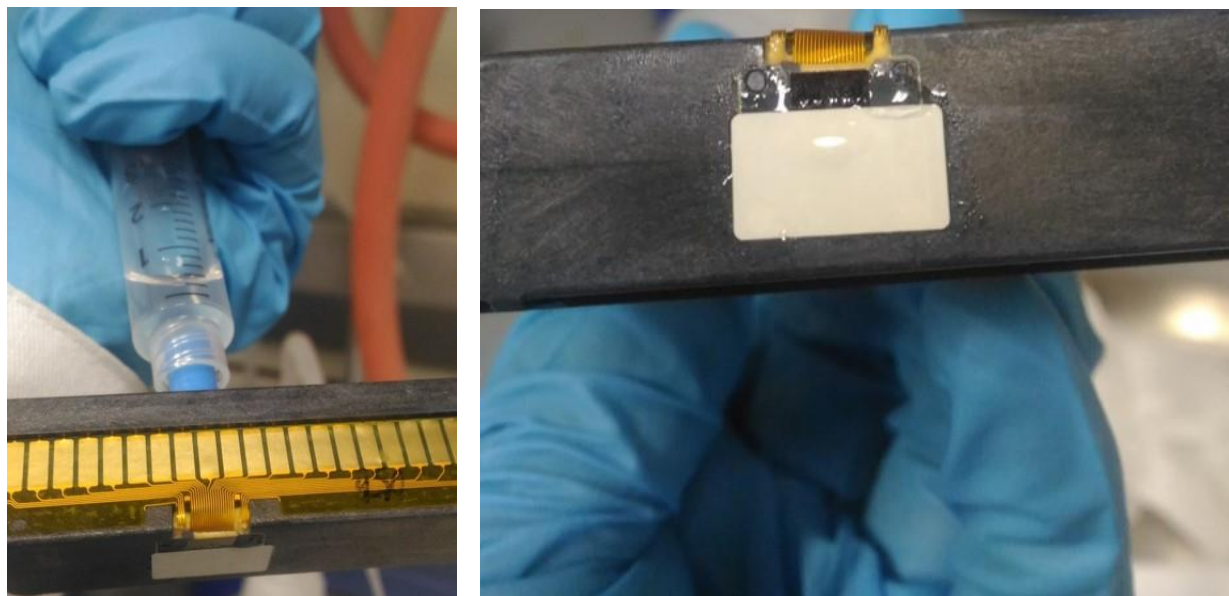


Figure 4.13: Manual pressure applied on Batch 3 ink to pass through DMC nozzle used in LP50 printer.

From the frequency based analysis of fresh (as received) inks, it can thus be concluded that G' and η^* values hold high relevance in desirable drop production, besides specific interactions occurring between the ink and the nozzle material. Quality of droplets produced determines the success of printability in terms of accuracy of printed structures. However, to some extent, these properties can be tuned using the parameters of the printer, such as timescales of pulse-Voltage waveform. Details and importance of timescale of waveform will be described in the following sections. In addition to rheological properties, surface interactions between the ink and the substrate surface also determine the success of printing in terms of development of structures on the substrate. Negative surface interactions lead to dewetting on the surface. Dewetting distorts the structural design of the prints, again rendering the printing unsuccessful (in this thesis the surface interactions have not been studied).

4.1.2 Rheological analysis with respect to temperature

4.1.2.1 Reference ink

Temperature dependence of rheology was analyzed by characterizing inks at 25°C and 45°C. On increasing the temperatures, shift of rheological parameters can be clearly observed, as shown in Figure 4.14. The ink shows expected shift of all three parameters to reduced values. Complex viscosity values halve from the range of 10-12 mPa.s at 25°C to ~ 6 mPa.s at 45°C. The viscous component of complex modulus also reduces from initial value of ~1 Pa to ~0.2 Pa at 10 Hz while maintaining its slope throughout and reaching final value of 14 Pa (at ~400 Hz) at 45°C compared to ~500 Pa (at 10,000 Hz) at 25°C. It is noteworthy to mention that the available data at 45°C ends at 500 Hz. The value of maximum elastic modulus also reduces from 1.5 Pa to 0.5 Pa. The value of G' at low frequencies, for 45°C remains constant until ~100 Hz, which is representative of resistance of the molecule to change its structure. Similar results were obtained for some dopant source inks. Thus, the attainment of maxima of all the parameters is seen at highly reduced frequency value for 45°C which could be well anticipated. However, the data is obtained only until ~500Hz. Possible reasons of this are explained in Chapter 3.

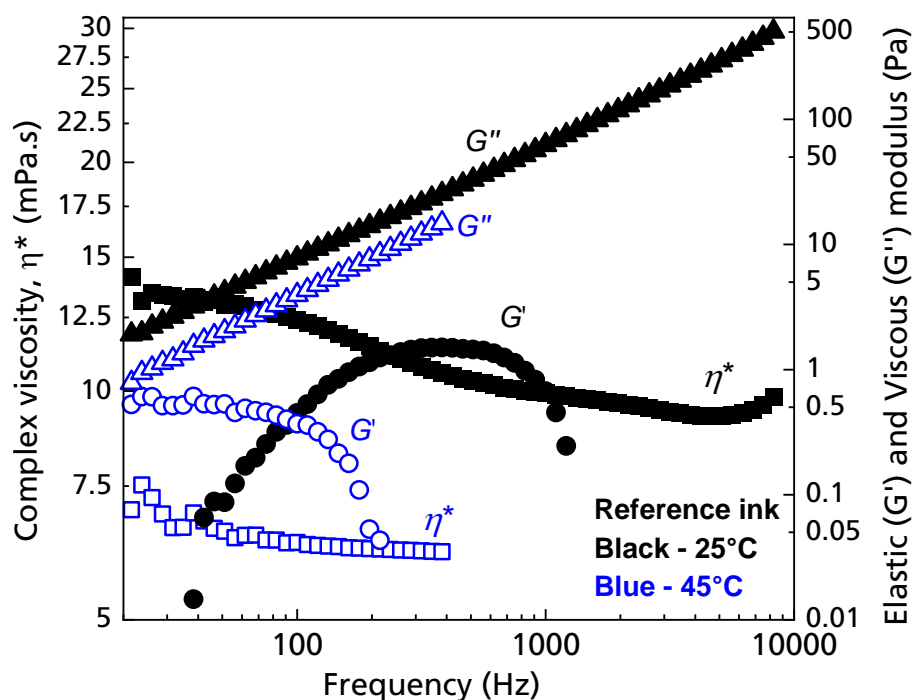


Figure 4.14: Change of rheological parameters of reference ink with respect to temperature and frequency.

4.1.2.2 Commercial inks

- **Batch 1**

The results obtained for P-ink of Batch 1 at higher temperatures, as shown in Figure 4.15, are similar to what was obtained for reference ink. Complex viscosity shows reduction from ~ 11 mPa.s at 25°C to ~ 5 mPa.s at 45°C . The Newtonian nature of the ink is retained at 45°C as well. Elastic modulus reduces drastically from a maximum of 0.5 Pa at 25°C to a scattered range below 0.1 Pa for very low frequency values. At higher frequencies, the values are negligibly low and thus not included in the graph. Similarly, viscous component of complex modulus also reduces from an initial value of 1.2 Pa at 25°C to ~ 0.2 Pa at 45°C maintaining almost the same slope.

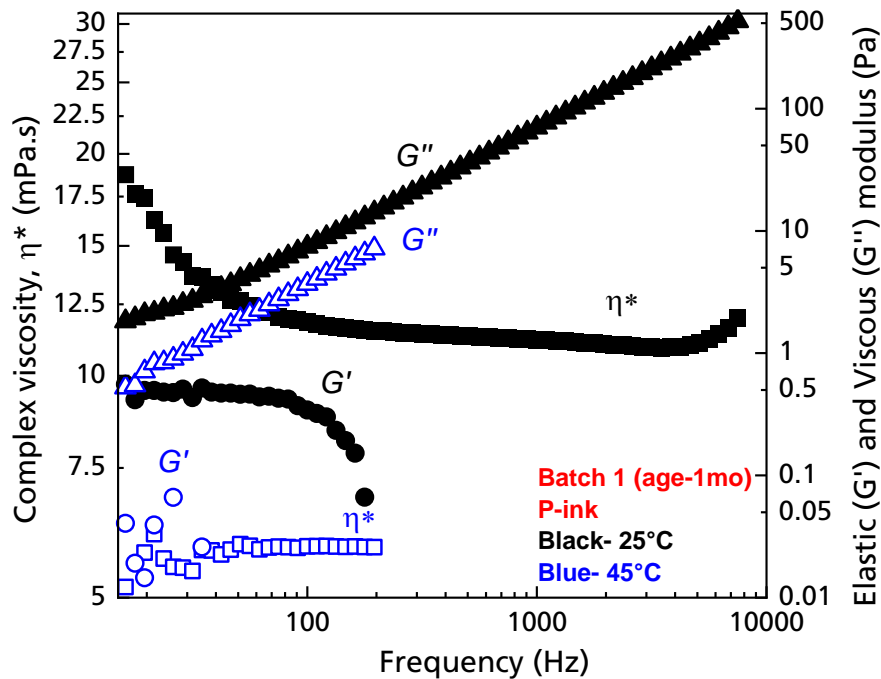


Figure 4.15: Change of rheological parameters of P-ink (Batch 1) with respect to temperature and frequency.

Contrary to P-ink, B-ink shows an increase in all its rheological parameters as the temperature is increased to 45°C . Complex viscosity increases from 7-12 mPa.s at 25°C to 28-38 mPa.s at 45°C , which is undesirable for inkjet printing. The higher viscosity values can be compensated for, by using high actuation voltage but the structural changes behind the process renders this solution less feasible. Viscous modulus also increases from 2 Pa at 25°C to 8 Pa at 45°C in low frequency range and from 500 Pa at 25°C to > 600 Pa at 10,000 Hz while maintaining the slope of the curve.

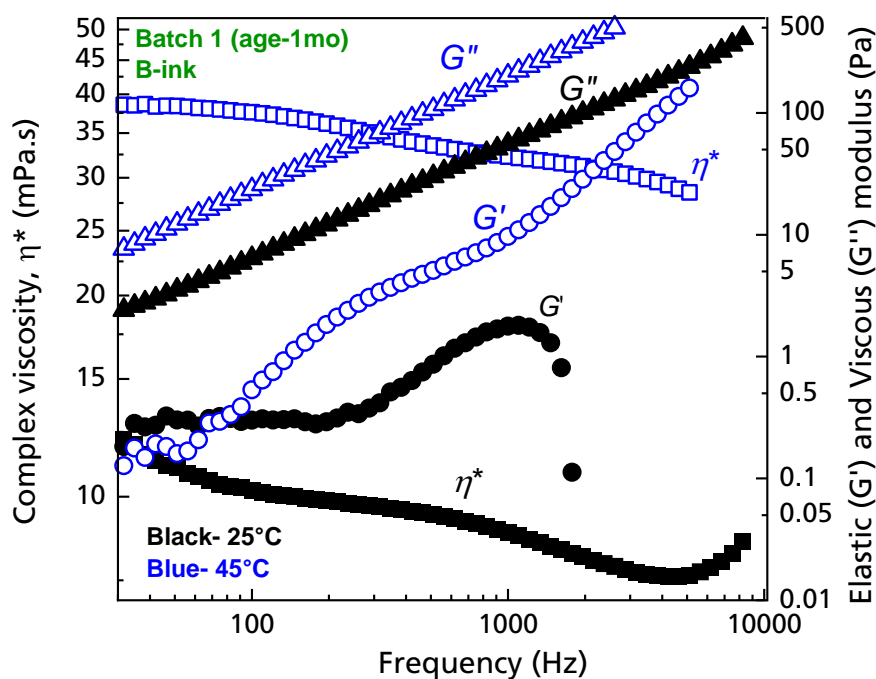


Figure 4.16: Change of rheological parameters of B-ink (Batch 1) with respect to temperature and frequency.

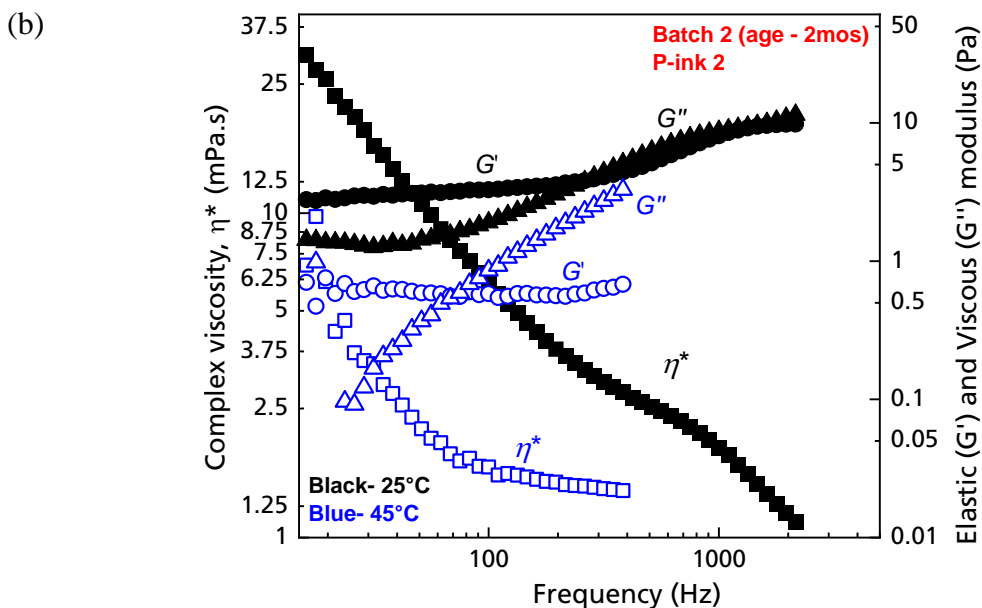
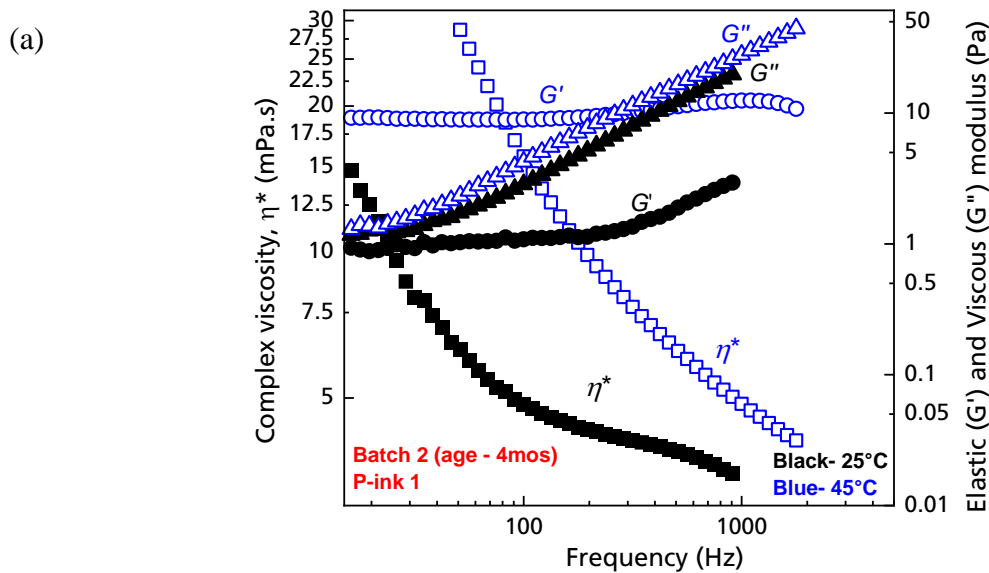
Elastic component of complex modulus at 45°C, beginning from the same point as for 25°C, i.e. ~0.2 Pa shows a higher slope than for G' at 25°C, as the frequency increases. As frequency nears 1000 Hz the slope tends towards a plateau development and at frequency >1000 Hz, the slope further increases attaining a maximum of 160 Pa at the 10,000 Hz.

- **Batch 2**

On increasing the temperature to 45°C, P-ink 1 exhibits increase in the value of its rheological parameters contrary to how polymers respond to temperature change conventionally. The slope and trend of evolution for all properties remain the same. Contrary to this, P-ink 2 exhibits conventional changes with the parameters reducing their values on increasing the temperature. The complex viscosity shows Newtonian behavior at frequencies higher than 100 Hz. The elastic modulus shows no change over frequency at 45°C while the viscous modulus increases linearly with a slope close to 1. Similarly, the two Boron based inks also show opposite behavior in response to temperature change. For B-ink 1, the viscosity values reduce by half on an average, throughout the entire frequency range while maintain its non-Newtonian behavior. The loss modulus also shows similar magnitude of change (G''). The elastic modulus (G') does not show a huge difference in values but a significant change in the trend of variation. At 25°C, G' was

constant initially and showed an increasing slope after ~300 Hz while for 45°C the slope continuously increases right from the beginning.

B-ink 2 on the other hand, like P-ink 1 shows an increase in its values as well as in its trend for complex viscosity and elastic modulus. Complex viscosity shows a typical shear thinning behavior for low frequencies and attains somewhat constant value as the frequency gets more than ~400 Hz. The elastic modulus shows a strong change in its trend from continuously increasing at 25°C to absolute constant at 45°C. The viscous modulus however remains almost unchanged.



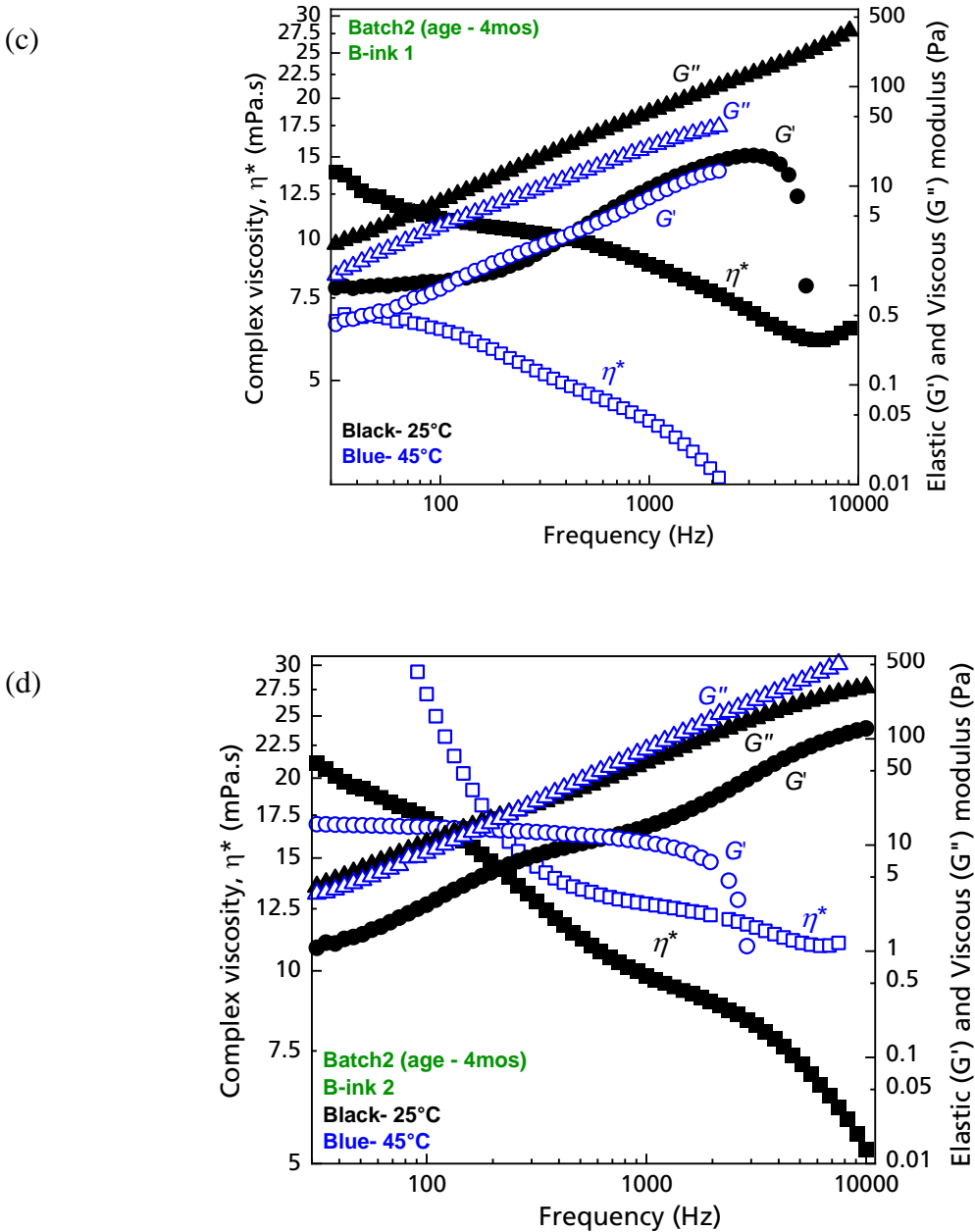


Figure 4.17: Change of rheological parameters of a) P-ink 1, b) P-ink 2, c) B-ink 1 and d) B-ink 2 (Batch 2) with respect to temperature and frequency.

- **Batch 3**

As observed from Figure 4.18, both P and B-inks from Batch 3 exhibited conventional polymer like nature with reduction in the values of all the properties for higher temperature. P-ink 1 shows a reduction by a value of 10 for complex viscosity while the trend remains the same. Similarly, elastic and viscous modulus reduce with no peculiar change in their curves, obeying the conventional temperature dependence rules.

B-ink 1 shows reduction in its complex viscosity initially by a value of 10. The trend however does not remain the same and ink shows non-Newtonian nature followed by a further reduction of slope similar to the trend at 25°C. Viscous and elastic components of the complex modulus also reduce considerably.

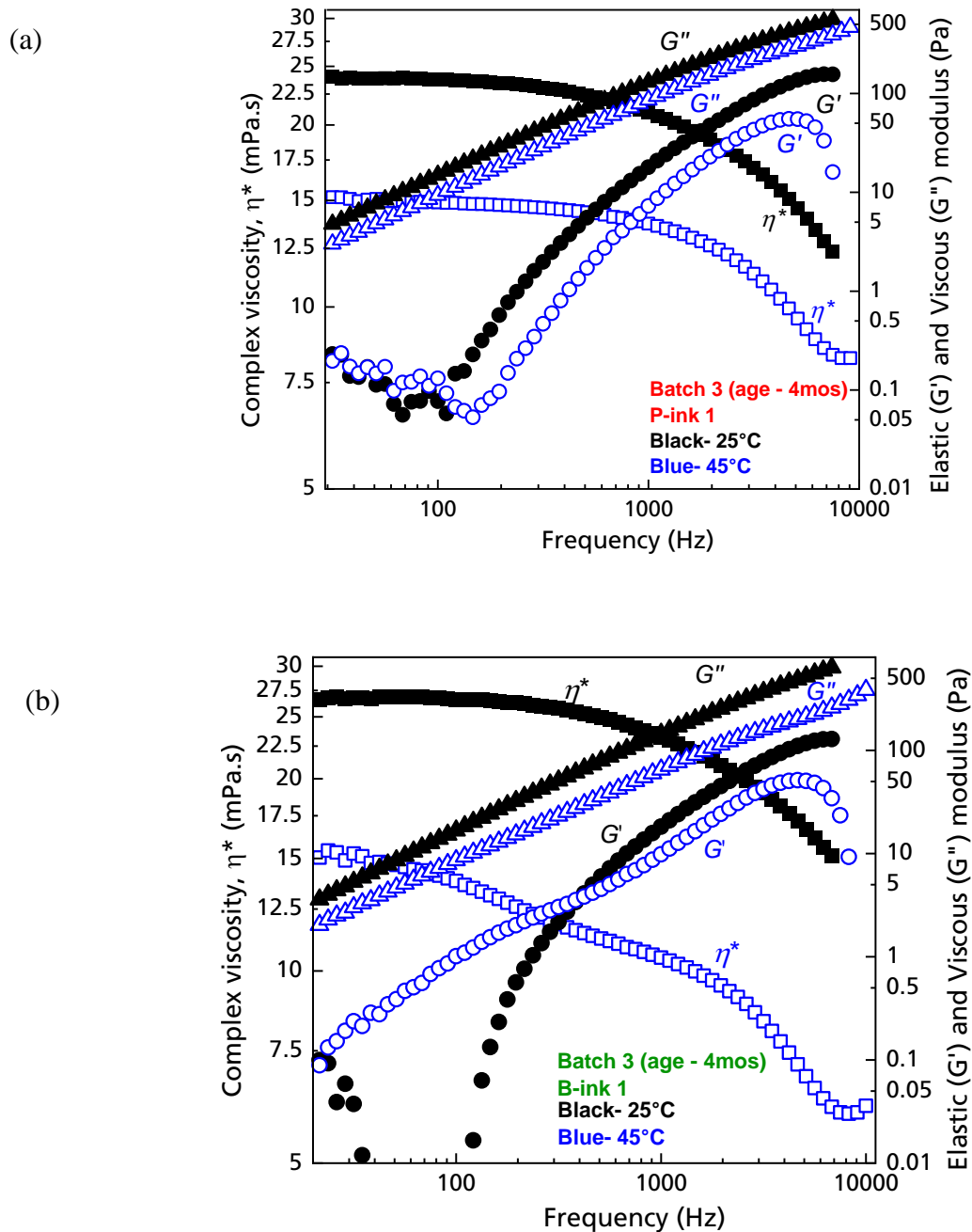


Figure 4.18: Change of rheological parameters of a)P-ink 1 and b)B-ink 1 (Batch 3) with respect to temperature.

Discussions

4.1.2.3 Reference ink

Ideally, the increase in temperature should result in lowering the complex viscosity, elastic as well as viscous components of complex modulus of the dopant source inks. As the temperature, increases, kinetic energy of the molecules (polymer chain molecules) increases thus enhancing their ability to flow. As viscosity represents the resistance to flow, higher temperatures offer to reduce this resistance and lower viscosity values. This effect can be used as an advantage in inkjet printing of viscous inks. To obtain viscosity in the desirable range of inkjet printing i.e. 2-20 mPa.s, theoretically by simply increasing the print-head temperature the parameters should favor printing or even drop formation at lower actuation voltages. However, on applying the same in practice, desirable results are not obtained as observed for dopant source inks, explained in further sections, since viscosity alone may not be sufficient to determine jettability/printability.

As the temperature increases, we require less external energy to deform the material to the same extent. At high temperatures thermal energy is supplied, which converts to kinetic energy and can be utilized to separate elements of any material, thus reducing the amount of other external forces needed for deformation, such as shear rate. Consequently, the modulus is lowered at high temperatures. Because of the same reason, viscosity also reduces; at higher temperatures lesser external energy is required to make the fluid flow at the same rate.

For reference ink, as can be observed from Figure 4.15, the values obtained are limited up to ~500 Hz. This feature may be attributed to the reduced viscosity, which might have caused spill of the ink at higher frequencies into the channel surrounding the plate of rheometer. As a result of insufficient ink being available for characterization, the sample might have failed to generate the output signal. Similar observation was also made for some commercial inks. Using shim of lesser thickness (shims are used to adjust the distance between the rheometer plates and thus to adapt to changing viscosity values) at higher temperatures can be a possible solution to avoid such results.

4.1.2.4 Dopant source inks

- **Batch 1**

P-ink

On increasing temperature, the rheological properties are still in the desirable printing range. Simple shift of data for all the curves represents simple temperature dependence of rheology like the one we observed for reference ink. The range of data over which the data is obtained at 45°C is again limited like for reference ink, in this case only to 200Hz. As of reference ink, the reason of too less viscosity can be attributed to this feature, which can lead to lesser volume retention in between the plates for longer times.

The differentiating feature at higher temperatures is that for elastic component. The value of G' reduces significantly and does not show any particular trend but only a few scattered points. Such reduced values can lead to failure of droplet formation and rather cause a spread of ink over the nozzle area.

B-ink

As opposed to the conventional temperature dependence of P-ink, B-ink shows quite complex response to higher temperature. At 45°C, for B-ink all the properties increase for the same frequency values. One possible reason of such behavior can be cross-linking of the polymer due to higher thermal energy at higher temperatures. Cross-linking will render higher rigidity to the polymer thus making it more resistant to any kind of deformation. Except for the values of elastic component at higher frequencies, the trend of change of parameters stays similar. For G' at higher frequency, shift to a higher slope signifies further rigidity of the polymer at higher strain values, thus further supporting the possibility of cross-linking of polymer. At higher temperatures polymerization itself can continue further, not necessarily leading to cross-linking or the inks may witness aggregation. Both the reasons will have similar impact on the rheological properties of the inks, leading to increase in their values.

Such behavior of the ink also implies the nearness of the cross-linking limit of the ink, to room temperature. Therefore, low operating temperatures will ensure optimum results during printing, provided no standard increase in viscosity occurs.

- **Batch 2**

The results obtained from P-ink 1 for higher temperatures (45°C) also indicate the possibility of nearness of critical conditions for cross-linking. The parameters show a shift towards higher values by significant amount signifying tougher response from the polymer. There are three possible explanations for the same. Firstly, considering the formation of crystals around the nozzles as described in section 4.1.2.2, temperature can also be another factor responsible for inducing crystallization besides high shear rate. Second possibility is that of cross-linking as for B-ink of Batch 1. It would imply requirement of a higher input to generate same output. After crossing the limit for cross-linking in terms of concentration and entanglement density of polymers, it is not possible to return to the initial state even on increasing the temperature. In fact, temperature further aids cross-linking and so does pressure. The printing conditions at the nozzle produce high pressure and strain rate thus increase the possibility of cross-linking. This holds for semi-dilute polymeric solutions as well as has been established in literature. Third possibility is that of evaporation of solvents. Some organic solvents like ethers and ethanol have low boiling points (~ 78°C for ethanol). Temperature of 45°C can heat the ink enough to cause some evaporation of solvents after some time and thus lead rise in the properties. Combining the

factors exhibited by P-ink 1 with the change in frequency (strain rate) and temperature, the possibly high entanglement density leading to high cross-linking explains the excessive clogging and hence poor printability. P-ink 2 does not show any such peculiar feature thus obeying theory without any drastic change in its rheology. However, the reduced range of data at 45°C might be due to temperature-induced crystallization.

The different behavior of B-inks also signifies similar changes as for P-inks. For B-ink 1, the change in viscosity and minimal change in G' can be due to easy orientation upon application of stress at elevated temperature of 45°C but no change in the structure of the polymer which results in same trends. On the other hand, B-ink 2, as evident by higher values of all its properties at higher temperatures, has probably cross-linked and thus witnessed a change in its structure. The dense cross-linked structure can be possible for the constant stiffness of the structure which results in constant G' .

- **Batch 3**

The resin based structure of both the inks, which is already dense and stiff shows no peculiar change on increasing the temperature suggesting simple shift towards easy flow regime at higher temperatures.

4.1.3 Rheological analysis with respect to aging time

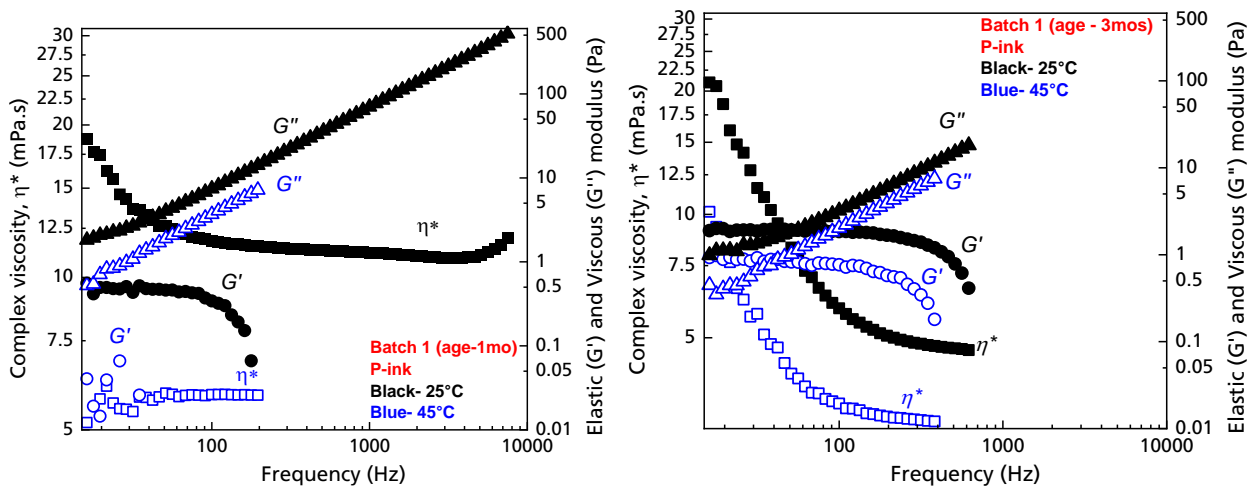
4.1.3.1 Results: Dopant source inks

- **Batch 1**

As can be observed from the Figure 4.19, both the inks show reduction in their rheological parameters due to aging. The data can be compared after aging of two months for 25°C as well as 45°C. The trend of the property change with respect to temperature although obeys conventional transitions but the shift of the trends of the properties after aging is significant as the ink has changed to non-Newtonian in nature with viscosity values at 25°C reduced from ~11 mPa.s to ~5 mPa.s. Albeit the values are still not too out of range, due to the expiration of the shelf life of ink the changed chemistry did not support printing results, neither would have yielded desirable electrical results, even if printable (which was observed for same inks bought earlier in other projects).

B-ink does not show as huge change in its rheology but the application was again limited owing to its shelf life. Contrary to the trends observed with fresh (as received) ink, aged B-ink shows conventional dependence on temperature with reduction of all its parameters with rising temperature. This suggests the change in the structure from dense, to lesser dense and lesser-coiled chains. As expected, the viscosity (after aging) reduces as the temperature increases from 25°C to 45°C. It is also worthwhile to notice that the change in the value of the elastic component of complex modulus has not changed much, especially for P-ink, which shows the same trend after aging as it did before aging. Therefore, it is reasonable to conclude that only the networking density has been reduced by breaking the backbone of the polymer due to natural aging factors.

P ink



B ink

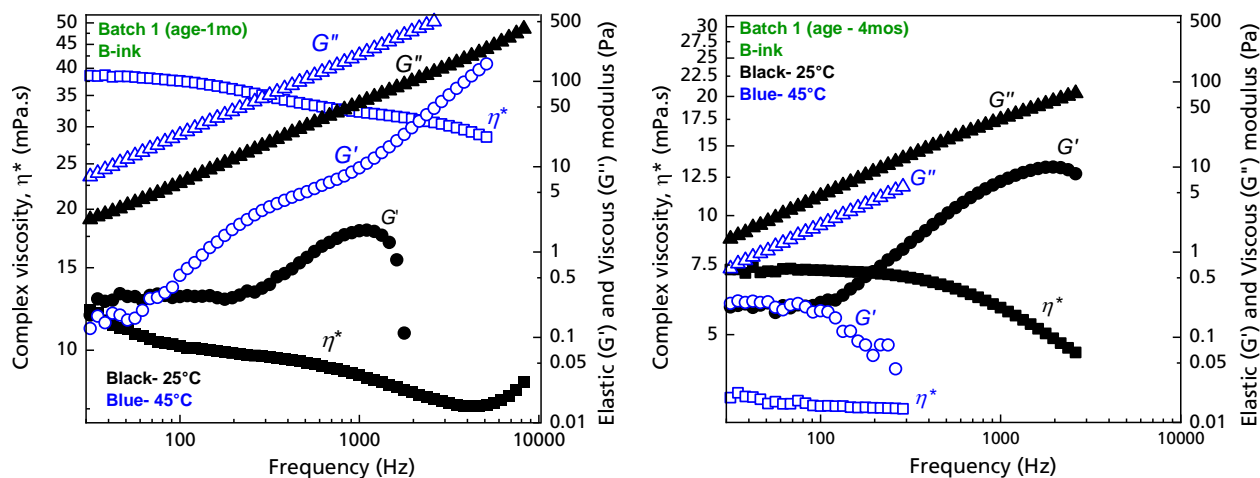
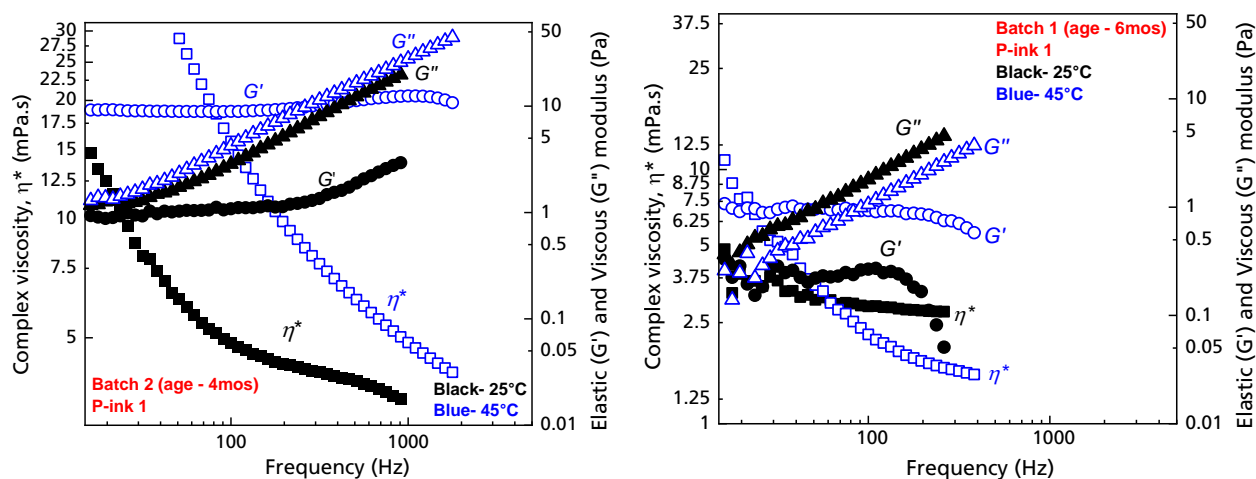


Figure 4.19: Change of rheological parameters of P-ink and B-ink (Batch 1) with respect to to aging time.

- **Batch 2**

From Figure 4.20, different aging effects on two P-inks can be observed. For P-ink 1, after aging, although elastic modulus rises with temperature as before aging, its complex viscosity reduces as frequency increases. However, the viscous modulus at 45°C is lesser than at 25°C throughout. This may suggest considerable change in the cross-linking of the structure, which might reduce further with time. Another important noticeable feature is the reduction of G' by one order of magnitude. On the other hand, P-ink 2 shows distinctively no change on increasing the temperature, suggesting complex structural changes.

Pink 1



Pink 2

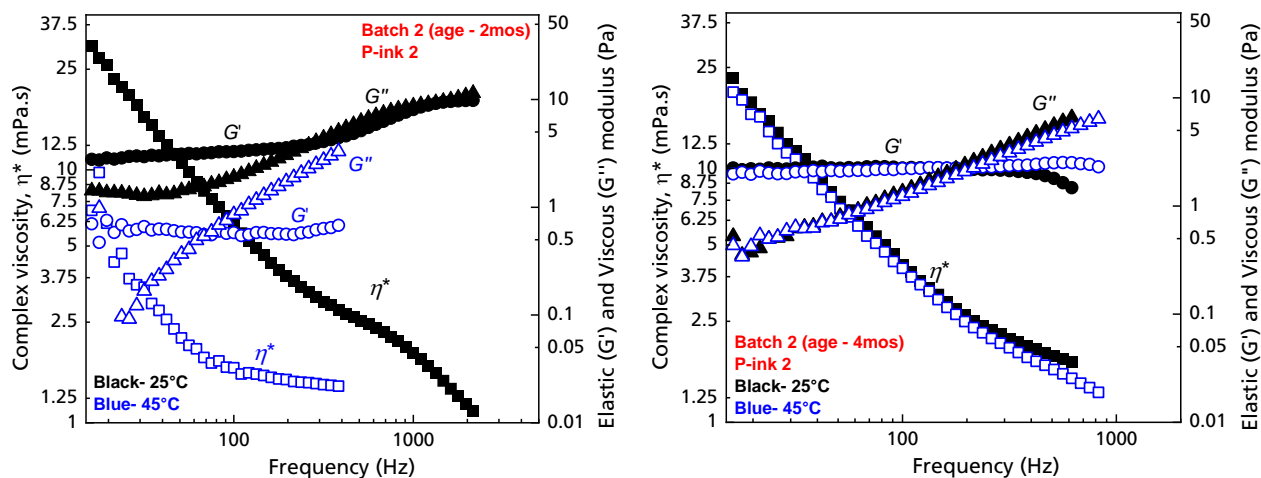
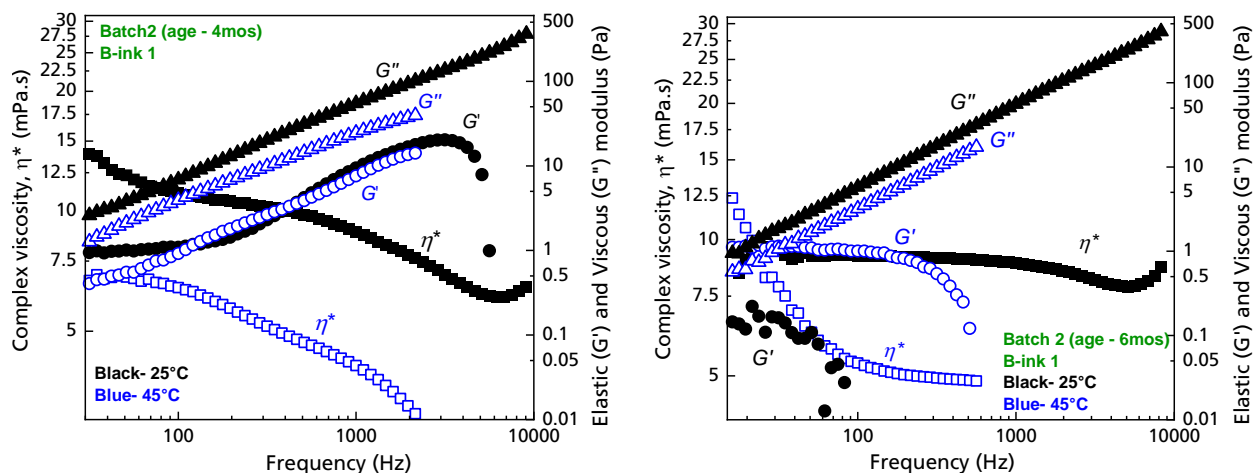


Figure 4.20: Change of rheological parameters of P-ink 1 and P-ink 2 (Batch 2) with respect to aging time.

As opposed to the differing nature of the properties of two P-inks, B-inks show similar aging effects, as can be shown in Figure 4.21. For B-ink 1, Newtonian behavior is induced by aging, which however changes to non-Newtonian on increasing the temperature. The increase of elasticity on increasing temperature suggests inability to reduce the cross-linking density substantially. Similar are the results for B-ink 2.

B-ink 1



B-ink 2

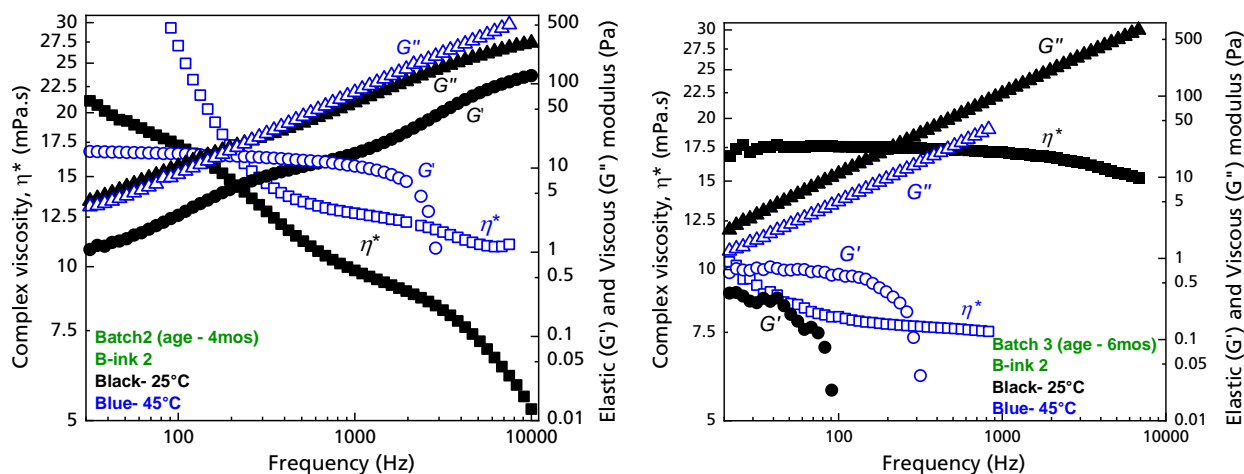
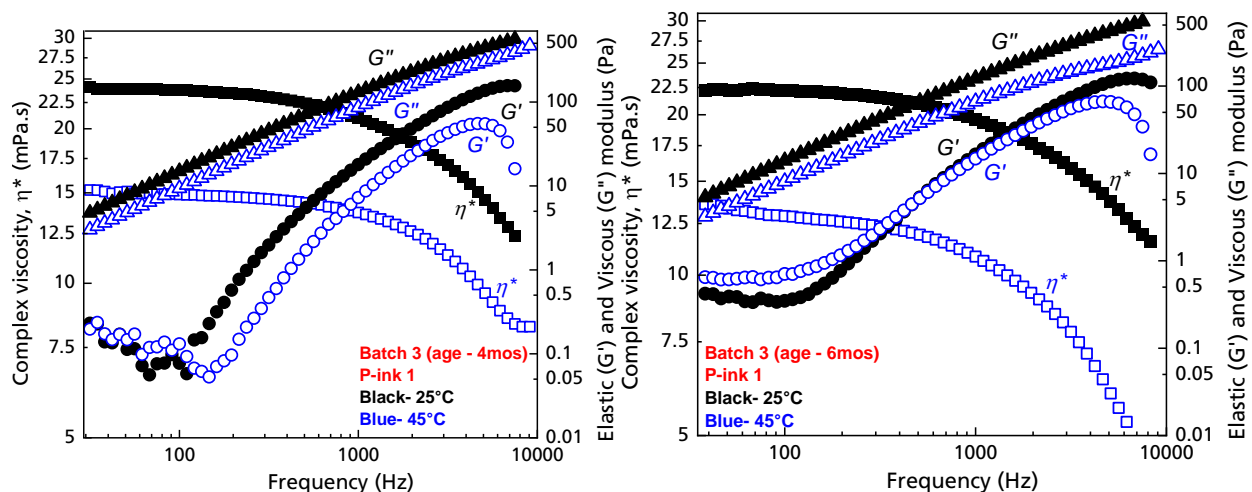


Figure 4.21: Change of rheological parameters of B-ink 1 and B-ink 2 (Batch 2) with respect to aging time.

- **Batch3**

As can be observed from Figure 4.22, P ink has maintained its rheology after two months of aging. There is no significant change in the behavior of the ink. Viscosity at 25°C for both fresh (as received) and aged inks are comparable and so are G' and G'' values. For B-ink also, the values are comparable except that the trend of change of properties has reversed. For aged ink, non-Newtonian nature is observed at 25°C whereas at 45°C it behaves as a Newtonian fluid. This stands opposite to the trend for fresh (as received) ink. Similar are the changes for G' while G'' stays more or less the same.

P ink



B ink

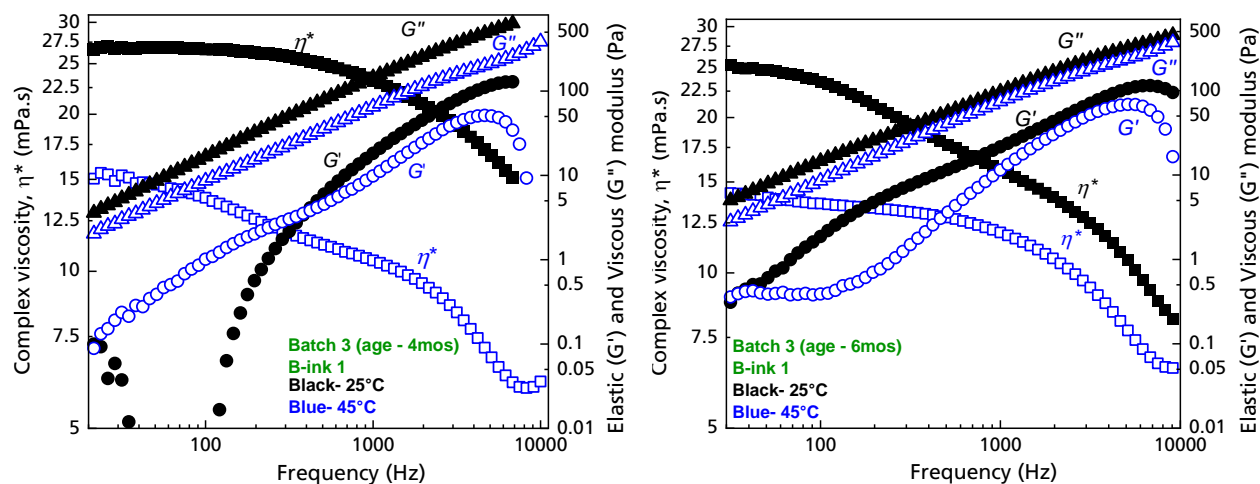


Figure 4.22: Change of rheological parameters of P-ink and B-ink (Batch 3) with respect to to aging time.

4.1.3.2 Discussion: Dopant source inks

The change of the properties after two months of storage suggests evident aging and hence degradation of the inks. Various factors could have played their roles in modifying the polymer structure, as described in detail in Chapter 2. The storage conditions of the inks were as recommended, in refrigeration with humidity absorbers, but some humidity is suspected to have interacted with the inks after their first opening. Given that the polymer inks are doped silicate polymers, they tend to react with water and undergo hydrolysis, which changes the structure and reorganize the molecules along the backbone. However, as explained in detail elsewhere [77] polymers with alcohol solvents, as may be in our case as well, can also witness re-esterification in presence of water molecules as the alcohols always have a possibility of forming azeotropes with water thus causing re-esterification of silicate gels. This phenomenon can leave a marked difference on their structure as well as the properties. In some cases of aging, we can only witness structural rearrangement, which may or may not involve dissolution of silicate framework. Nonetheless, this will also lead to change of the properties.

Besides these factors, the natural aging process, which leads to reduction of average length of molecular backbone, has a profound effect in reducing viscosity as well as elasticity of such degraded polymers. Similar effects have been observed in many dopant source inks as can be seen from Figures 4.19 – 4.22.

4.2 Inkjet Printing Process Development

To investigate printability, polymer based inks were printed using a PiXDRO LP50 piezo DOD inkjet printer (Meyer Burger Technology AG) equipped with a 10 pl Fujifilm Dimatix disposable cartridge. Printing was conducted under inert atmosphere inside glovebox (GS GLOVEBOX System technik GmbH) with the conditions set to - pressure of 0.8 mbar, and O₂ and H₂O levels of 3 and 0.7 ppm. Although printing of dopant sources can be conducted in open atmosphere without any pre-requisites, specific environment was maintained during the experimentation of this thesis, in order to achieve better control over various parameters such as humidity, temperature, pressure, etc. and to minimize the chances of contamination. One of the key features of PiXDRO LP50 printer, which makes it suitable for research and development of inkjet processes, is the tunability of voltage and time of the waveform, which determine the shear strain level applied on ink during printing. Default waveform of PiXDRO LP50 printer is shown in Figure 4.24.

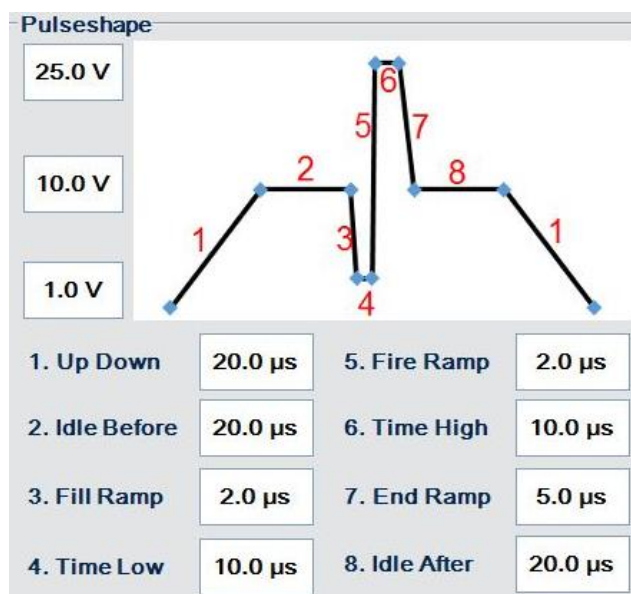


Figure 4.23: Default waveform of PiXDRO LP50 inkjet printer

The following subsections explain in detail, the optimization of printing parameters for different dopant source inks and the electrical properties obtained after printing the same over different lifetime samples. It is important to mention that based on rheological analysis of our inks, the print-head temperature was set between 20-25°C, for all successful printing processes and inks as most inks exhibited ideal behavior in this range. The temperature of glovebox was maintained at ~15°C in order to keep the service conditions as near to storage conditions as possible and provide ideal environment for the inks.

4.2.1 Waveform simulation

To simulate the piezo-driven printing conditions, an oscilloscope (here a ‘Picoscope’ by pico® Technologies) was used, in combination with the PAV rheometer sample holder. This allowed

analyzing the response of a sample liquid to a certain input signal - rectangular wave as input, in order to meet the signal of the pulse produced at the nozzles (represented cumulatively by step 5, 6 and 7 of Figure 4.23). The working principle has been explained in detail in Chapter 3. As is shown in Figure 4.24 the output - dampened oscillations are recorded as change in $V(t)$ which in case of dopant source inks, appear as sinusoidal waves, shown in red. The output produced here is in the absence of any sample, representing attenuation caused by air. As can be observed, the attenuation of the output is minimal and the wave maintains its sinusoidal nature until its significant decay at $\sim 1\text{ms}$. The time in microseconds (μs) inset in the image helps estimate the time needed for the pulse signal. Time under row '1' marks the beginning of signal, as indicated by the first dashed line while the one under row '2' marks the end of the peak of pulse (end of step 7 in Figure 4.23), indicated by the latter dashed line. ' Δ ' gives the difference between the two points thus giving the net time required for the pulse.

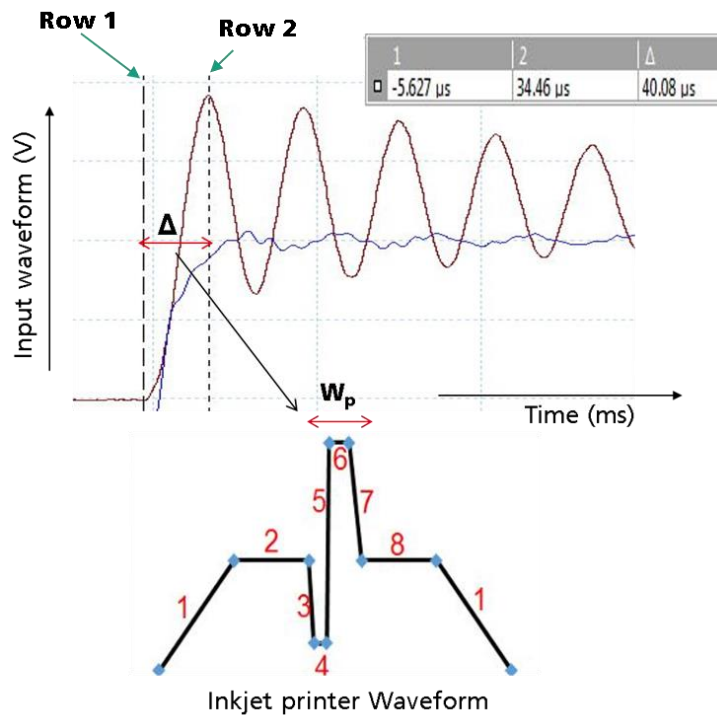


Figure 4.24: Picoscope measurement in the absence of sample; time interval between point of initiation and peak (Δ) relevant to pulse width (W_p) of waveform. Blue signal represents the rectangular input wave while the red waves represent the sinusoidal output.

When conducting this measurement on polymer inks, each ink produced a characteristic Δ value for the peak time and also a characteristic output wave, representing the resistance offered by the individual ink. Resistance of each ink is due to its density and viscosity. Since the P-ink from Batch 1 exhibited ideal characteristics, as explained in section 4.2, its Δ value therefore served as a reference value. Since it produced smooth printing while using default waveform, the ratio between the default pulse width and the measured Δ value of this ink could be used as scaling factor to calculate the required pulse widths for all other inks. A shift in the peak position relative

to P-ink 1, whether to the right or to the left, indicates a corresponding increase or decrease in the pulse time, respectively. An example of the same concept can be seen in Figure 4.26.

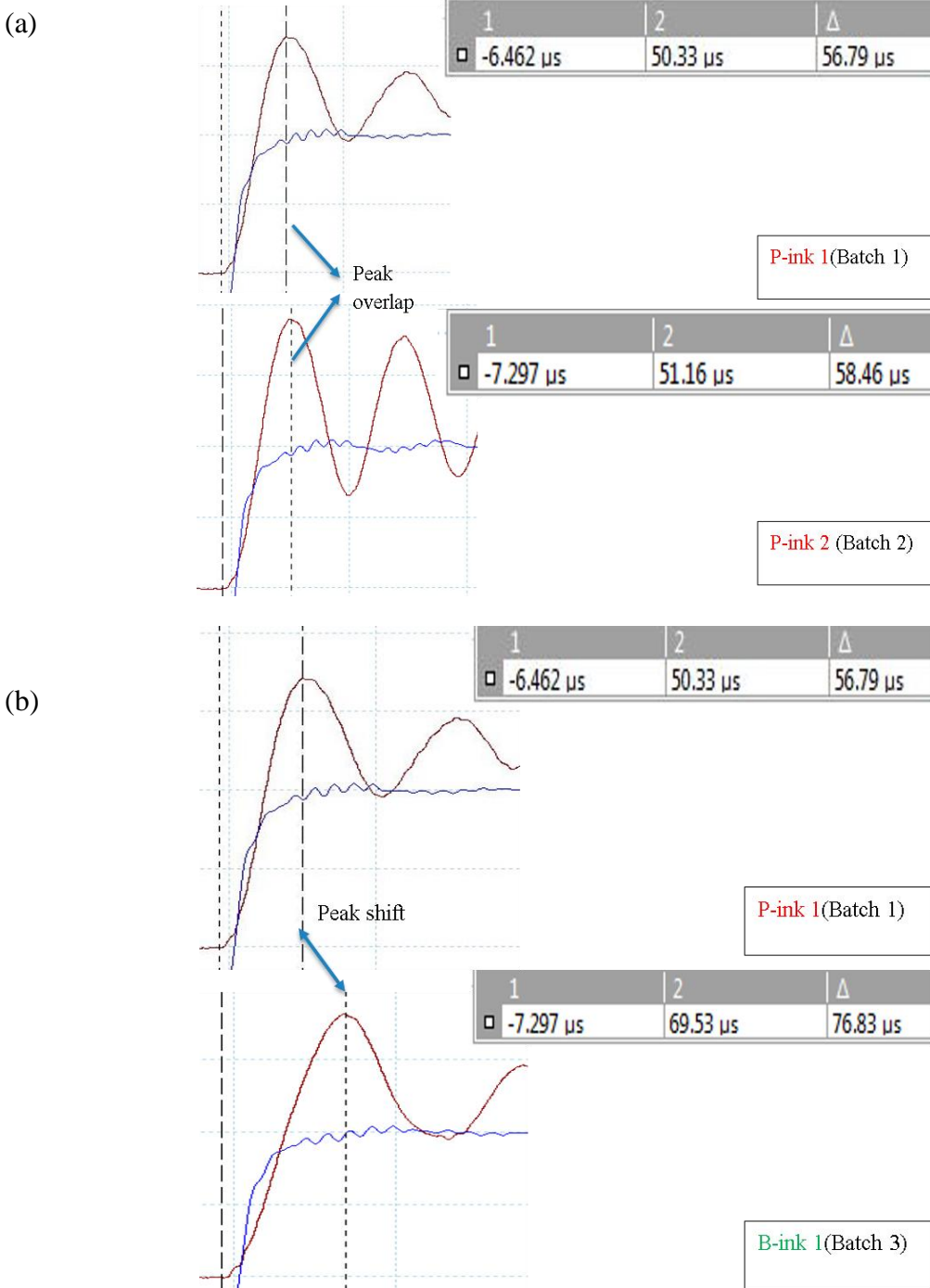


Figure 4.25: Picoscope measurement comparing a) P-ink 1 (Batch 1) and P-ink 2 (Batch 2) and b) P-ink 1 (Batch 1) and B-ink 1 (Batch 3). With P-ink 1 acting as reference, a shift of the peak for other inks implies, that a change in the pulse width of the piezo signal is required.

As shown in Figure 4.26 (a), there is overlap between the peak times for P-ink 1 from Batch 1 and P-ink 2 from Batch 2. This would imply that no change in the pulse width (i.e. step 5, 6 and 7 in Figure 4.24), compared to P-ink 1, was necessary. The anticipation was correct, as observed during printing. P-ink 2 also produced smooth printing results like P-ink 1 using the same signal settings. Similarly, in case of B-ink 1 of Batch 3, from Figure 4.26 we see a significant peak shift, which implies, that changes in the pulse width values are needed to obtain the desired printing behavior. From our experience with B-ink 1 for Batch 3 and as explained in detail in section 4.1, we realized, that the rheology of the ink also suggests the same. Similarly, other inks were also assessed.

For each ink, the peak time, as collected from Picoscope curves, can be related to the pulse width of the voltage waveform, given by time scales of step 5, 6, and 7, as explained earlier. The ratio of the two quantities enables quantitative comparison of different inks. The higher the difference compared to ratio for standard ink, more variations are needed in the timescales of voltage waveform. For reference ink, the values of peak time (t_p) ratio and pulse width (W_D) were found to be $53 \mu s$ and $17 \mu s$ respectively, producing a ratio of 3.11 (t_p / W_D). Relative to the reference ink, the pulse width for other inks were found using equation 4.1:

$$W_{p, Ink X} = t_{p, Ink X} / R_{Reference} \quad (4.1)$$

where, $W_{p, Ink X}$ is the pulse width of ink x, $t_{p, Ink X}$ is the peak time of the ink found using Picoscope and $R_{Reference}$ is the ratio of the reference ink i.e. 3.11.

As observed from printing experiences, inks with huge differences exhibit very poor printing, implying diverse underlying reasons.

4.2.2 Optimization of Printing Parameters

As mentioned in the previous section, waveform development with a suitable time dependent voltage is the key factor behind optimizing the printing process. The jetting frequency (shear strain), experienced by the inks at the nozzle, is a complex combination of frequency of the waveform and the nozzle firing frequency, and can be adjusted externally. As mentioned in previous sections, the working frequency of the inkjet printer is between 1000 -10,000 Hz (typically around 2000 - 5000 Hz). Due to the ambiguity of exact printing frequency, it becomes a tedious task to determine the exact rheological behavior exhibited by the inks during printing. As a result, the nearest we can get to the ideal rheological response to a given printing frequency is based on estimation and anticipation. The voltage and firing frequency parameters, even though seemingly ideal, do not guarantee an ideal droplet production and ideal printing behavior. However, the waveform significantly influences the droplet formation, volume, flying velocity and angle. The droplet volume determines how the droplet will upon impact spread on the substrate and how precisely it will generate the desired design. Around 12 pl is the ideal droplet volume considering to the nozzle size and the minimum resolution of the printer. The flying velocity determines the homogeneity of the print. All the droplets are expected to have a similar flying velocity. Dissimilar flying velocities can lead to some areas being left unprinted, while excessive ink is being deposited elsewhere. The angle of the flying droplets also signifies the precision of the design. Too large an angle would imply a larger deviation from the ideal orthogonal direction to the substrate and hence lead to imperfections in the printed structures. This can be a serious drawback for IBC solar cells due to their small feature sizes.

As has been mentioned in detail in section 4.1, changing the voltage are done only according to the viscosity values of the ink, with higher voltage needed for inks that are more viscous. In order to develop a printing process for a particular ink, its viscosity must lay in the required range for inkjet printing, tailoring the time scales of the waveform plays an indomitable role. As can be observed in Figure 4.24, each part of the ramp is associated to a time in μs . Increasing the time of any particular part of the ramp leads to lowering the frequency and vice versa. The maximum strain is achieved by a pulse ramp (which has the maximum voltage). Therefore, increasing the time of step 5, 6 and 7, i.e. fire ramp, time high and end ramp, as shown in Figure 4.24, plays a stronger role in lowering the frequency. This has a direct implication on the range of rheological characteristics prevalent during the printing operation. In such a way, we can change the parameters and hence select the desirable rheological properties which favor printing. This approach proved successful for some inks, as will be explained later.

Depending on the favorability of the rheological characteristics, successful prints were obtained for only two inks: P-ink (Batch 1) and P-ink 2 (Batch 2). These inks are referred to as P-ink 1 and P-ink 2 henceforth. Possible reasons for poor printing results of the other inks are explained in section 4.1.

4.2.2.1 P-ink 1

Given the near ideal rheological characteristics exhibited by P-ink 1, much changes were not required in the default waveform of the inkjet printer.

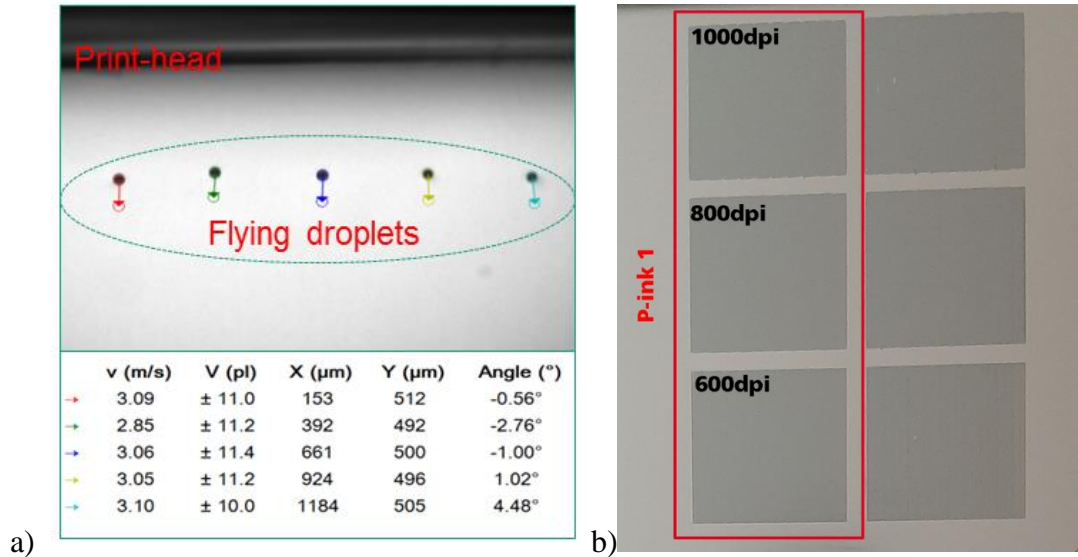


Figure 4.26: a) Dynamic analysis of the ink-droplets by drop-watcher of LP50 printer. Volume V , velocity v , and angle of flying droplets quantify the printing behavior. As here, controlling these parameters enables achievement of precise printing of droplets onto the silicon substrate. b) $2 \times 2 \text{ cm}^2$, P-ink 1 printed areas with three different resolutions, on Saw Damage Etched surface.

As we realize from Figure 4.26 a), the velocity and volume for all the drops are almost the same. The differences in the angle of deviations are not big enough to affect the printed structures of bulk areas, as in our case. Owing to the ideal rheological characteristics exhibited by this ink, the printing behavior was ideal, thus leading to excellent printed structures, as is shown in Figure 4.27 b). At 600 dpi, the squares produced are sharp edged and well defined. As the resolution increases, we experience bleeding edges, producing inaccuracy in our designs.

In Figure 4.27, optical microscopic images show the impact of different resolutions on the quality of the printed areas in terms of homogeneity of the ink distribution; 600 dpi produces sharp and well-defined edges with a homogeneous in distribution of ink, as suggested by ink color across the printed area. The images are captured at $200 \mu\text{m}$ resolution, after annealing the wafers at different temperatures above 900°C . Upon increasing the resolution to 1000 dpi, we can observe different colorations suggesting an inhomogeneous ink deposition. Darker colors along the periphery imply a larger volume of ink along the boundaries. An inhomogeneous ink distribution implies an inhomogeneous charge carrier distribution, leading to non-uniform electrical properties over a single printed area. The overall result at higher print resolutions is an inaccurate and oversized print structure with undesirably uneven electrical properties due to an uneven

dopant distribution. Given the results of printing, we can conclude 600 dpi is the best-suited printing resolution considering both the precision of the printed designs and the uniformity of the electrical properties.

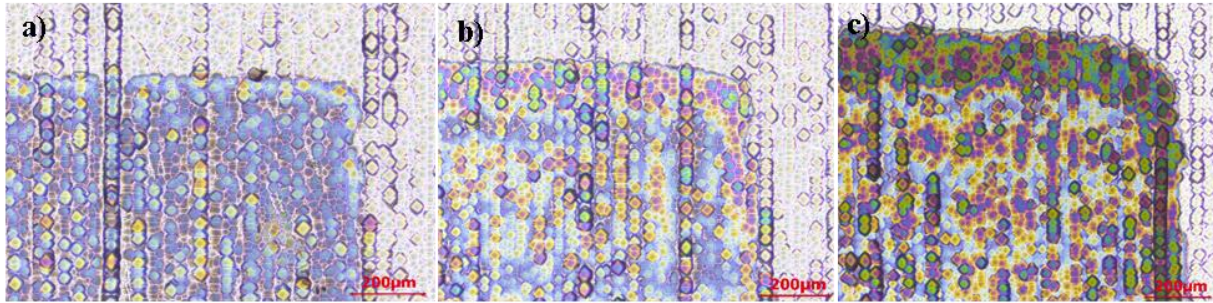


Figure 4.27: Optical microscopic images captured after high temperature annealing of structures printed with P-ink 1 at a) 600x600 dpi, b) 800x800 dpi and c) 1000x1000 dpi resolution.

4.2.2.2 P-ink 2

The rheological behavior of P-ink 2 was very different from ideal ink as has been explained in detail in section 4.1. However, changing the time of pulse ramp reduces the frequency and enables selection of favorable range of its rheological properties. As can be seen from Figure 4.28, the droplets produced are ideal in nature with no tails and satellites. The volume and the angle of flight are almost same for all the droplets. The flight-velocity being the same for all the droplets implies a good synchronization amongst all the nozzles.

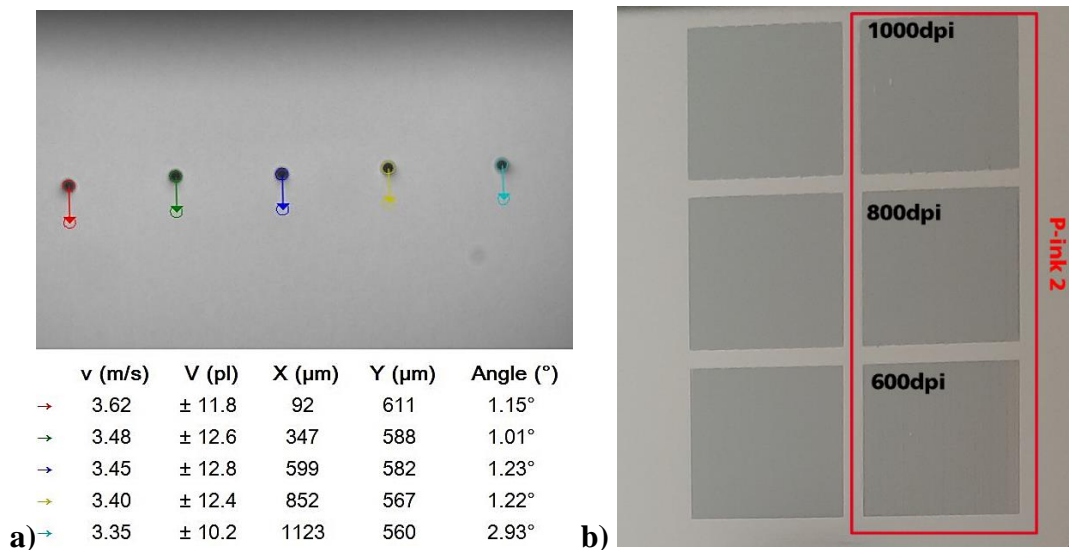


Figure 4.28: a) Dynamic analysis of P-ink2 by drop-watcher of LP50 inkjet printer. b) 2x2 cm², P-ink 2 printed areas with three different resolutions, on saw damage etched wafers, with minimal nozzle clogging.

Like P-ink 1, 600 dpi resolution produced the best printing results for P-ink 2. A higher resolution ended up with rounded corners and blurred/bleeding edges, causing inhomogeneity in the ink distribution, as shown in Figure 4.29. In addition to the voluminous deposition along the periphery, there is an uneven ink distribution along other areas as well, attributable to ink-surface interactions. Negative interactions can lead to dewetting or blistering on the surface of the substrate.

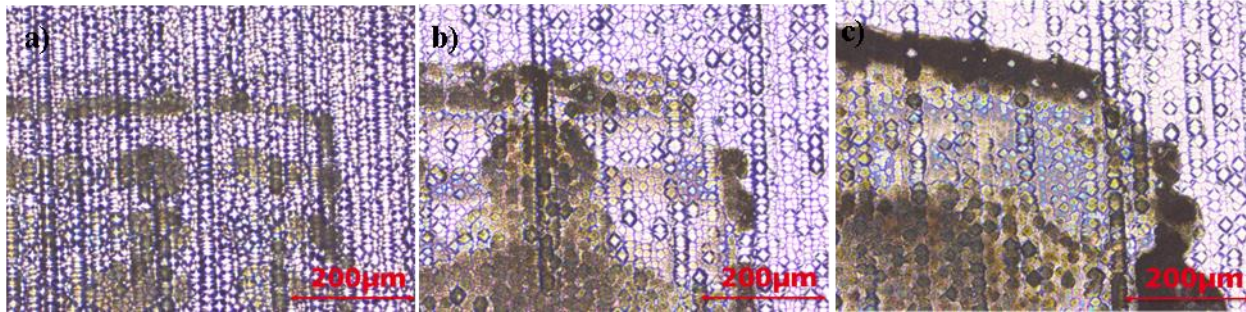


Figure 4.29: Optical microscopic images captured after high temperature annealing, for P-ink 1. The structures were printed at a resolution of a) 600 x 600 dpi, b) 800 x 800 dpi and c) 1000 x 1000 dpi.

4.2.2.3 B-ink

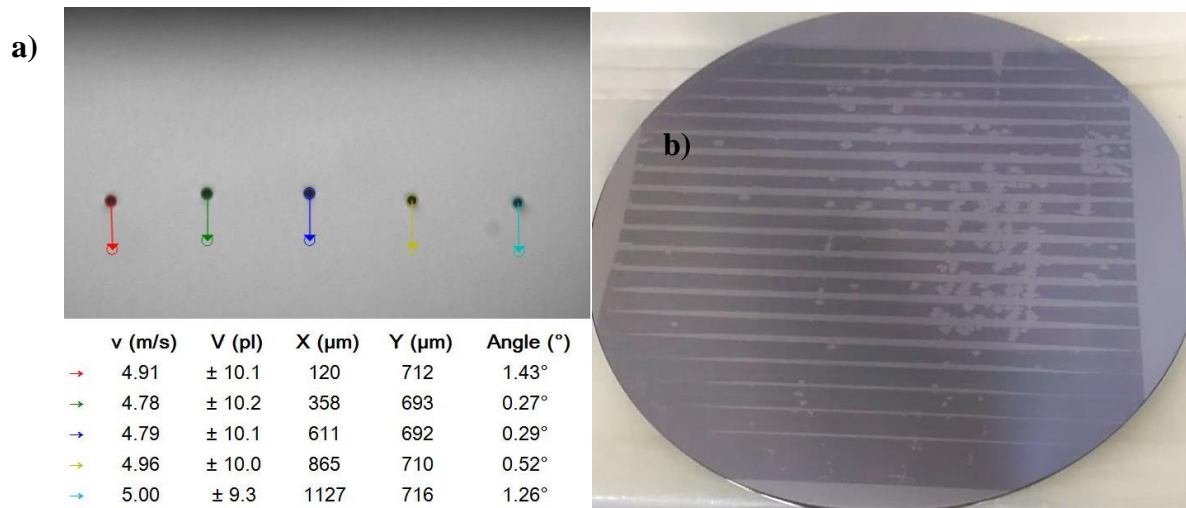


Figure 4.30: a) Dynamic analysis of B-ink 1 (Batch 1) by drop-watcher of LP50 inkjet printer b) 85x85 cm² printed area at 600x600 dpi, on shiny etched wafers, with dominant nozzle clogging and excessive dewetting.

Similar to P-ink of Batch 1, B-ink also exhibited nearly ideal rheological characteristics and accordingly, the droplets produced with the default voltage waveform, were also ideal. As seen in Figure 4.30 a) all the droplets have almost the same volume around 10 pL, the same deflection angle, as well as the same velocity of deposition on the substrate. Ideally, the printing should have been smooth, but the behavior of the ink and thereby the droplet production are not the only factors that determine the overall printing success, as has been understood from previous printing experiences as well. From Figure 4.30 b) we can see a somewhat good printing at the beginning (bottom side of image) which gets worse as the printing was continued, as evident from the clogging nozzle patterns (empty lines), probably caused by an interaction of the ink with nozzle material. In the upper half of the image, we also see evident dewetting, due to poor ink-substrate interactions. Therefore, for this ink, although initially the printing behavior was good, the ink showed strong dewetting when printed on FZ shiny etched wafers, as shown in Figure 4.30. Preparation of FZ samples is explained in Chapter 3. The results were similar to past experiences with the same ink in previous projects and therefore no further experiments were conducted.

4.3 Electrical Properties of inks

After extensively screening the inks based on their rheology and developing appropriate printing process, we evaluate the electrical properties of inks on lifetime samples having tunnel oxide passivating contacts (TOPCon) on both sides. Lifetime samples were prepared with different thickness of amorphous silicon (a-Si) layers deposited by means of Plasma Enhanced Chemical Vapor Deposition (PECVD) and Low Pressure Chemical Vapor Deposition (PLCVD), as described in Chapter 3. Lifetime samples enable characterization of charge carrier lifetime at different injection levels through photoconductance measurements.

Presence of a-Si layers induces passivation and owing to the quantum tunneling effect observed by charge carriers through the SiO_x layer, both the categories of samples (100nm and 50nm a-Si layered lifetime samples) fall under TOPCon, a follow up of Passivated Emitter Rear Contact (PERC) technology. The presence of tunneling layer as thin as 1.3nm ensures minimum role of pinholes in charge carrier transport, but does not rule out their presence. However, the dominant mode of charge transport remains tunneling.

4.3.1 Evaluation of passivation quality of P-doped TOPCon layers

In order to evaluate the surface passivation, lifetime dependent QSSPC measurements were conducted, after annealing the wafers at different temperatures for the diffusion of dopants into the substrate. As concluded from section 4.1 only P-ink 1 of Batch 1 and P-ink 2 of Batch 2 enabled a successful printing and the results obtained are therefore for the same two inks. Henceforth, the mentioning of the Batch of these inks will be left out and the inks will be referred to as ‘P-ink 1’ and ‘P-ink 2’ respectively. The results mentioned are for the optimized printing

resolution of 600 x 600 dpi. From previous printing experiences, it has been observed that resolutions lower than 600 x 600 dpi do not provide a sufficient concentration of charge carriers and therefore are not well suited for the development of efficient devices. Less concentration of charge carriers directly leads to a reduction in current density, while it indirectly makes the defects play a dominant role. Therefore, the overall electrical performance of the device would be poor. At the same time, higher resolutions come with their characteristic problems as well, which are explained in section 4.2.

4.3.1.1 Lifetime samples with 100nm PECVD (a-Si) TOPCon

The printed wafers were subject to various temperatures for annealing/diffusion, in order to assess the best annealing conditions to maximize the implied open circuit voltage, implied fill factor, and hence increases the passivation quality of the cell. According to selection of different temperatures and time for annealing, five recipes were chosen, as mentioned below:

Table 4.3: Annealing recipes used for lifetime samples with 100nm a-Si layers TOPCon.

Recipe number	Temperature (°C)	Time (min)
1	925	30
2	950	10
3	950	30
4	975	10
5	975	30

The a-Si layer starts transforming to poly-Si at around ~800°C. The main aim of designing as many recipes as possible is to find the best diffusion temperature and time for a maximum concentration of dopants in the poly-Si surface, while maintaining a shallow profile in c-Si.

As we observe from Figure 4.31, the value of iV_{oc} increases continuously, as we increase the temperature and time, for both P-ink 1 and 2. High temperatures and times provide more energy, making the conditions more conducive for an enhanced diffusion of Phosphorus atoms (P atoms) into the poly-Si layer. Higher the number of P atoms, higher is the concentration of n-type charge carriers and thus the corresponding iV_{oc} values. For P-ink 1, the values increase from 654 mV at 925°C, 30 min to a maximum of 720 mV at 975°C, 30 min. However, they remain somewhat similar, with ~700 mV for 950°C, 30 min and 975°C, 10 min implying similar overall diffusion conditions generated in these two situations. A higher surface charge carrier concentration enables a favorable energy band bending of the junction. Similarly, for P-ink 2, the iV_{oc} values increase from a minimum of 655 mV at 925°C, 30 min to maximum of 714 mV at 975°C, 10 min. For P-ink 2 we observe no further improvement at 975°C, 30 min, implying a saturation of the diffusibility of P-atoms at 975°C, 10 min. Considering the performance of both inks, we can conclude that 975°C, 30 min provides best cell characteristics in the annealed condition. However, the lower values at other temperatures can still be improved, as described later.

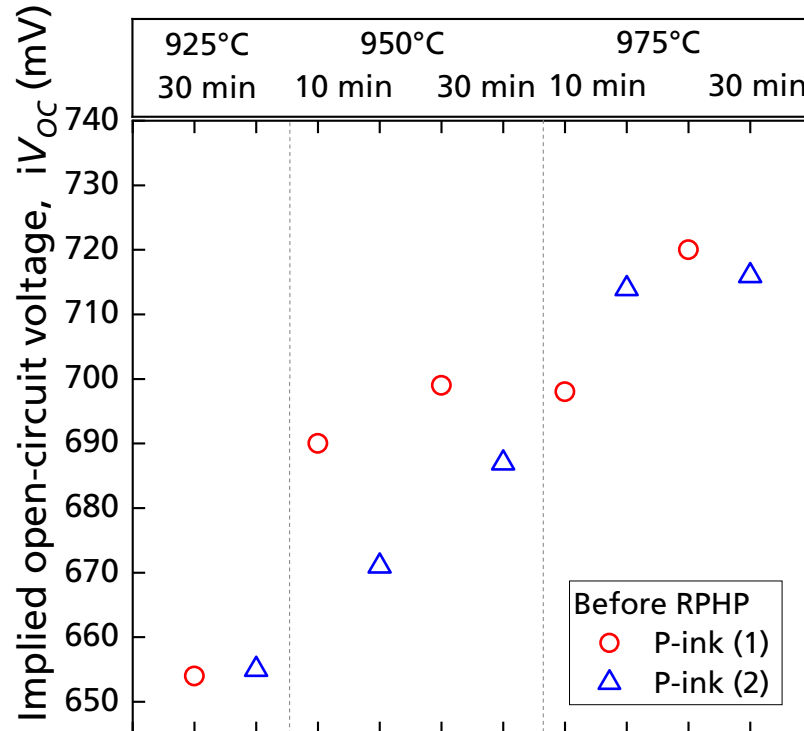


Figure 4.31: Implied open-circuit voltage ($iVOC$) of P-ink (1) and P-ink (2) printed on 100nm thick a-Si layers of lifetime sample, with resolution of 600x600 dpi, evaluated for different high-temperature processes before remote plasma hydrogen passivation (RPHP).

The implied fill factor (iFF) is the relevant parameters for the electrical quality of a contact and helps in assessing the recombination-limited FF potential. It is a direct measure of the minority carrier recombination at the Maximum Power Point (MPP). The difference between the measured effective lifetime and the intrinsic limit, defined by Auger recombination, is a measure for the quality of the passivated contacts. iFF and $iVoc$ show a similar trend in their values when increasing the time and temperature, as is evident from Figure 4.32. For P-ink 1, the values increase from a minimum of 65% at 925°C, 10 min to a maximum of ~86.8% at 975°C, 30 min, which remains almost same for last three recipes (temperature and time combinations). For P-ink 2, the iFF increases from 67% at 920°C, 10 min to a saturation value of ~86% at 970°C, 10 min. The saturation of iFF at high temperatures can be caused by a high Shockley-Read Hall recombination (SRH), which becomes dominant at low injection densities. A high temperature can lead to an intrusion of the charge carrier profile into the c-Si layer and thus making the SRH recombination dominant. An achievement of a 720 mV $iVoc$ and a ~86% iFF is a remarkable outcome of successful suppression of carrier recombination, indicating an excellent passivation over a wide injection range.

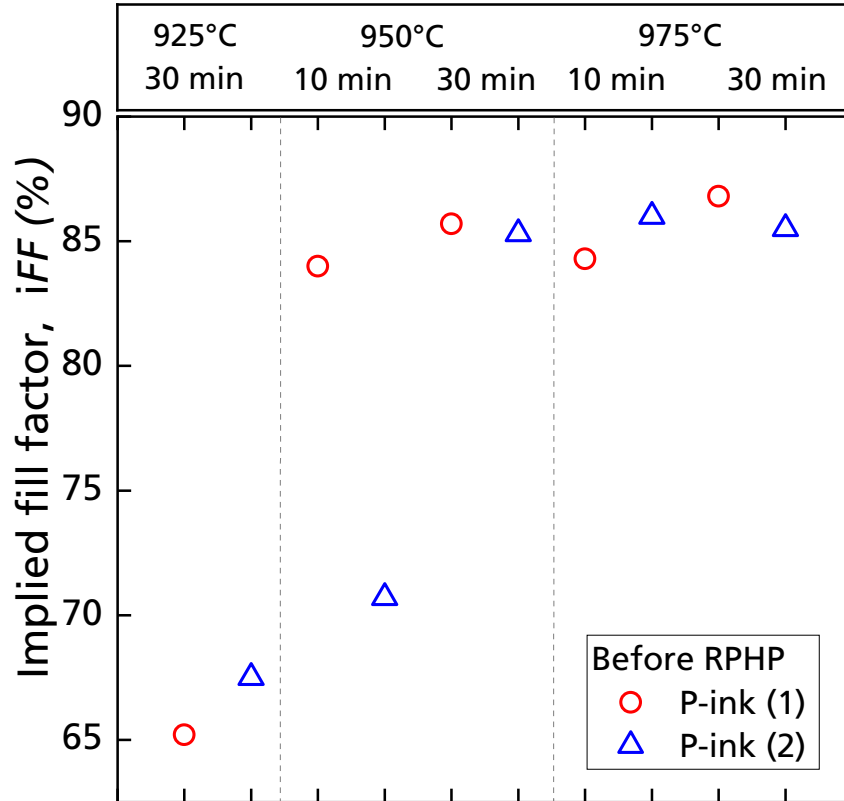


Figure 4.32: Implied fill factor (iFF) of P-ink (1) and P-ink (2) printed on 100nm a-Si layers of lifetime samples, with resolution of 600x600 dpi, evaluated for different high-temperature processes before remote plasma hydrogen passivation (RPHP).

4.3.1.2 Lifetime samples with 50nm LPCVD (a-Si) TOPCon

Unlike for a 100 nm a-Si sample, for a thin 50nm a-Si sample, there is an evident degradation of electrical characteristics, as can be observed from Figure 4.33. This can be a direct outcome of the difference in thickness of the a-Si layer. The degradation is more prominent in case of P-ink 2, which shows a maximum of 686 mV at 925°C, 10 min and continuously reduces to a minimum of 653 mV at 975°C, 30 min. As observed from the ECV results, P-ink 2 has higher charge concentration than P-ink 1. A high concentration of charge carriers along with high temperatures can lead to a deeper profile of charge carrier into the c-Si. As explained earlier, SRH recombination is directly related to the amount of dopants present, which makes it pre-dominant for P-ink 2. Moreover, since the *iFF* is measured at low charge injection levels, that makes the situation for P-ink 2 even more precarious, leading to a higher degradation. In addition, it could also be due to the local disruption of the SiO₂ tunnel junction in O₂ free environment [78]. For P-ink 1, however, there is some improvement in *iVoc* values from 694 mV at 925°C, 10 min to 702 mV at 950°C, 30 min, after which there is a strong reduction by ~20 mV to a value of 686 mV at 975°C, 30 min. From this data, it is clear that the optimum conditions for a thin a-Si layered substrate is at a lower temperature, while using P-ink 2 and around 950°C, 30 min for P-

ink 1. Therefore, promising values are produced by P-ink 1. These values can further be improved. The diffusion recipes used are tabulated below:

Table 4.4 : : Annealing recipes used for lifetime samples with 50nm a-Si layers TOPCon

Recipe number	Temperature (°C)	Time (min)
1	925	30
2	925	10
3	950	30
4	975	10

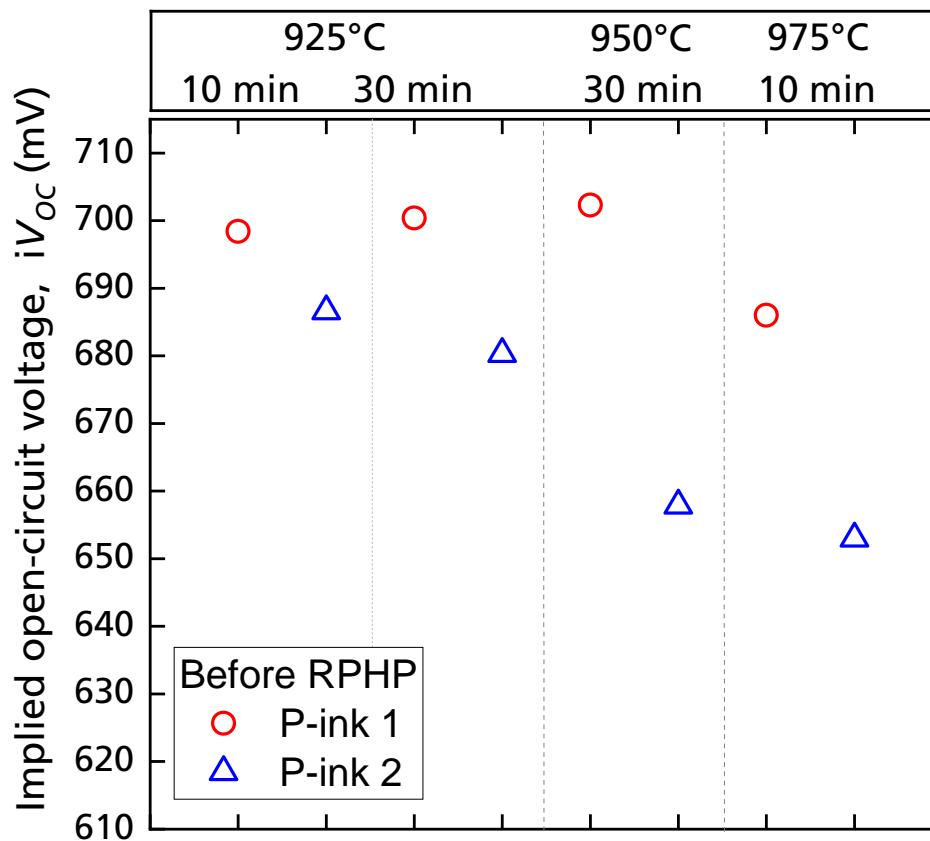


Figure 4.33: Implied open-circuit voltage (iV_{OC}) of P-ink (1) and P-ink (2) printed on 50nm a-Si layers of lifetime samples, with resolution of 600x600 dpi, evaluated for different high-temperature processes before remote plasma hydrogen passivation (RPHP).

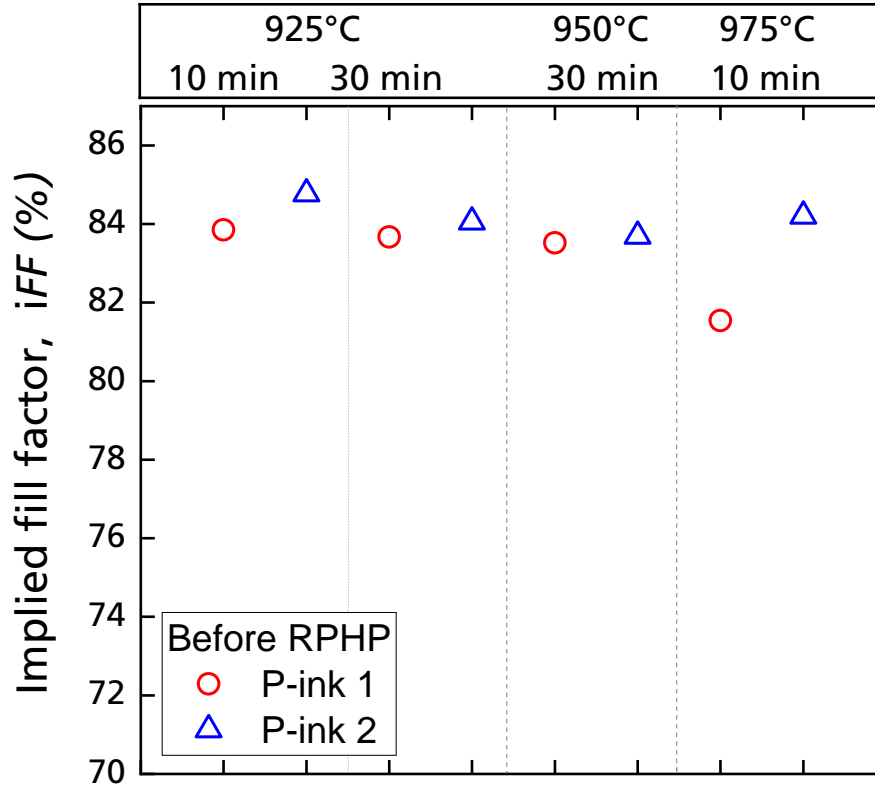


Figure 4.34: Implied fill factor (*iFF*) of P-ink (1) and P-ink (2) printed on layers of 50nm thin a-Si lifetime samples at 600x600 dpi, evaluated for different high-temperature processes before remote plasma hydrogen passivation (RPHP).

From the *iFF* values, as depicted in Figure 4.34, degradation is again evident at higher temperatures. A reduction in the *iFF* values is not by the same scale as for *iVoc*. The measurement at 975°C, 30 min did not yield a compatible result and hence was neglected.

4.3.2 Evaluation of Passivation Quality after Hydrogen Passivation (RPHP)

4.3.2.1 Lifetime samples with 100nm PECVD (a-Si) TOPCon

As was expected from RPHP, the values of the *iVoc* for wafers, which initially showed low values, was substantially improved by a margin as big as ~75 mV, as can be observed from Figure 4.35. The highest measured *iVoc* after RPHP reaches 732 mV for P-ink 1 and 734 mV for P-ink 2. Therefore, it is now reasonable to deduce that the availability of P-atoms was not a limitation for the reduced voltage but the rather the presence of defects, which hindered the flow of charge carriers. The wafers, which were initially annealed at low temperatures, were subject to the RPHP treatment in order to improve their characteristics. As we observe from the Figure, the difference between the *iVoc* values before and after RPHP gradually reduce towards higher

temperatures, suggesting an upper limit to the possible improvement in iV_{oc} values by that method.

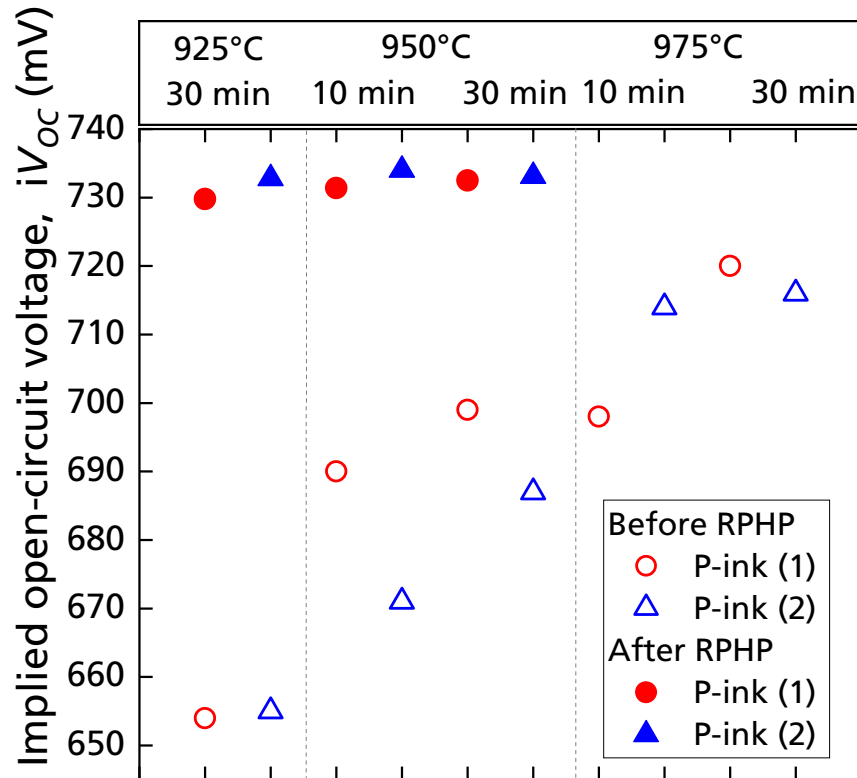


Figure 4.35: Implied open-circuit voltage (iV_{oc}) of P-ink (1) and P-ink (2) printed on 100 nm a-Si layers of lifetime samples at 600x600 dpi, evaluated for various high-temperature processes before and after remote plasma hydrogen passivation (RPHP).

Moreover, the values show saturation for both inks right after 910°C, 10 min, after RPHP, implying similar improvements irrespective of the previous annealing history. We can also observe a similar saturation in the data for iFF after RPHP treatment, where we finally reach values as high as 86.7% for P-ink 1 and 87% for P-ink 2, which is almost the same as the maximum values attained without RPHP treatment.

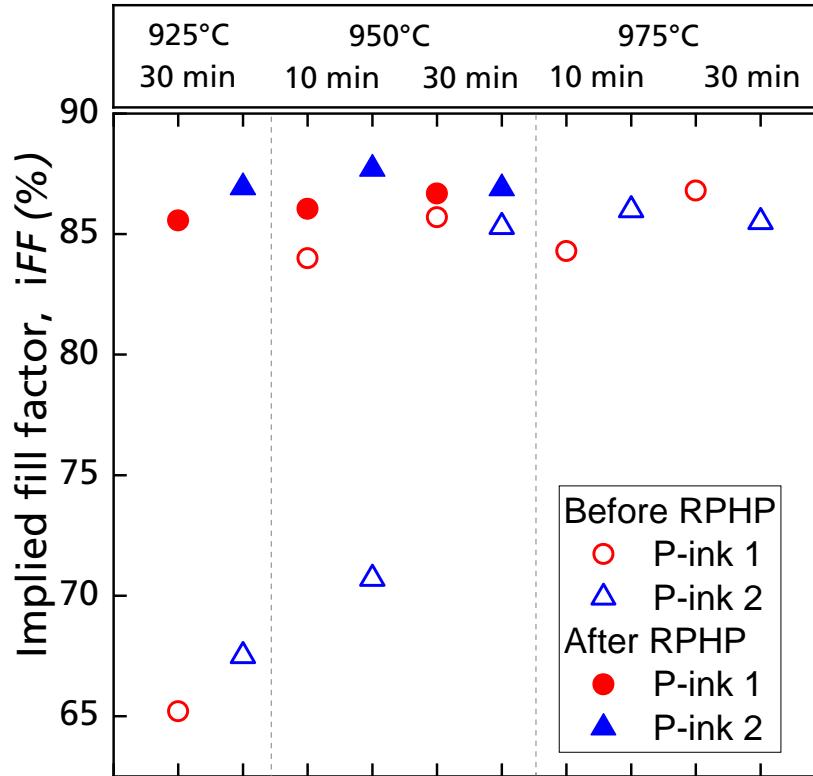


Figure 4.36: Implied fill factor (iFF) of P-ink (1) and P-ink (2) printed on 100nm a-Si layers of lifetime samples at 600x600 dpi, evaluated for different high-temperature processes before and after remote plasma hydrogen passivation (RPHP).

4.3.2.2 Lifetime samples with 50nm LPCVD (a-Si) TOPCon

Similar to the effect of RPHP in the previous case, we observe an increase in the values of iV_{oc} and iFF for 50 nm a-Si samples as well. However, the change in the characteristics is less pronounced. The iV_{oc} for P-ink 1 shows almost no increase for two recipes (1 & 3) and ~ 10 mV for two recipes (2 & 4) with a maximum of 710 mV at 925°C, 30 min. For P-ink 2, a maximum improvement is observed for the first recipe with an improvement of 6 mV, producing final 692 mV. For the subsequent recipes, there is almost no change due to RPHP, as observed from the overlap of the values before and after RPHP.

Similar effects can be seen for iFF values, where the change in the values due to RPHP is minimal for both the inks, with a maximum difference of 4% for P-ink 1, its maximum value being 85%, and a difference of 1% for P-ink 2, obtaining a maximum of 85% again. The results, however, are not compatible with the iV_{oc} and lifetime values. As mentioned in the introductory part, these samples contain B-ion implanted dopants on the front side. This can prove to be a limitation for no substantial change in iFF values.

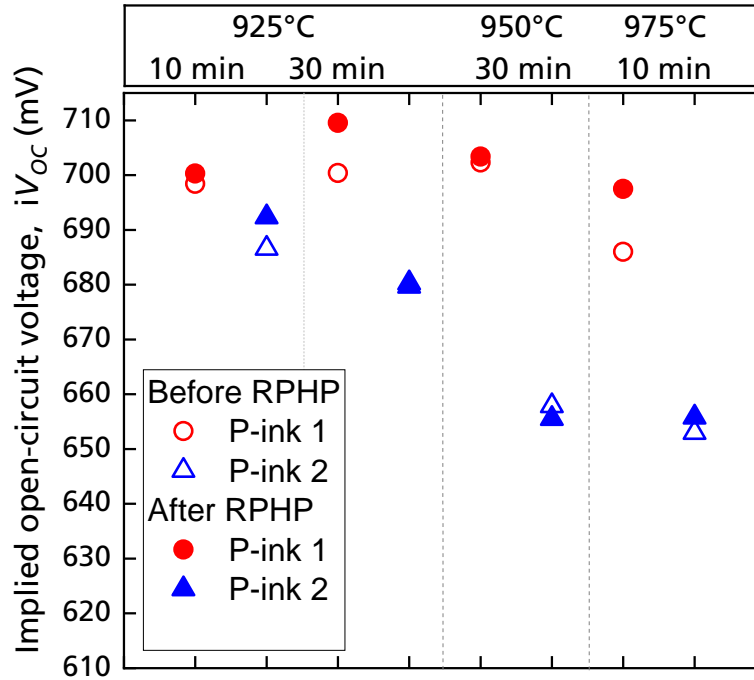


Figure 4.37: Implied open-circuit voltage (iV_{oc}) of P-ink (1) and P-ink (2) printed on 50nm a-Si layers of lifetime samples at 600x600 dpi, evaluated for different high-temperature processes before remote plasma hydrogen passivation (RPHP).

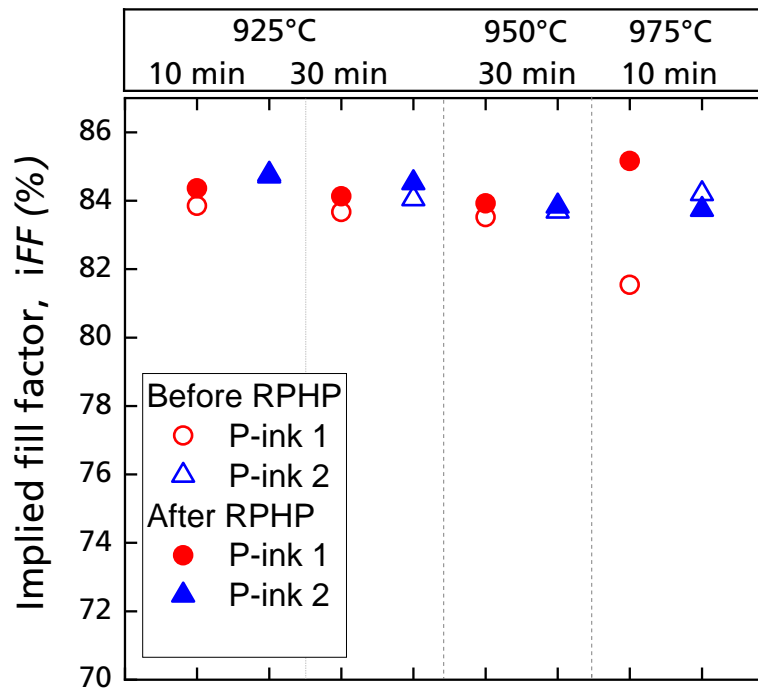


Figure 4.38: Implied fill factor (iFF) of P-ink (1) and P-ink (2) printed on 50nm thick a-Si layers of lifetime sample, with resolution of 600x600 dpi, evaluated for different high-temperature processes before and after remote plasma hydrogen passivation (RPHP).

Summary

From the QSSPC data, we can summarize the electrical characteristics based on two explanations:

- a-Si layer thickness: Passivation quality of a-Si layers (which later transforms to poly-Si) changes for both 100nm and 50nm layered lifetime samples. Performance differs according to the inks used (the charge carrier concentration specific to each ink) and according to the temperature to which the lifetime samples are subjected during annealing. For 100 nm a-Si layered samples, excellent outcomes were obtained for both, P-ink 1 & 2, producing iV_{oc} as high as 732 mV & 734, respectively. For these samples, higher temperatures favored passivation quality. Contrarily, for 50 nm a-Si layered samples comparatively lower temperatures favor improved passivation quality for both P-ink 1 & 2, with maximum iV_{oc} obtained 710 mV and 692 mV respectively. However, since the 50 nm a-Si samples used in this thesis are asymmetrical, we can find results for symmetrical samples in work previously done by Z.Kiaee et al [79] using the P-ink 1. The difference in passivation quality can be related to the charge carrier concentration on the surface (poly-Si) and the profile depths across poly-Si produced by both inks. Relevance of charge carrier concentration to the passivation quality is explained in further sections.
- Inks: P-ink 1 and P-ink2, although showing similar trends for iV_{oc} and iFF in general, exhibit differences in their electrical properties, primarily due to the difference in the concentration of ‘P’ atoms contained in both inks. Dopant concentration in inks determines the difference in charge carrier concentration diffused into the poly-Si layer, which later determines their respective electrical characteristics. Moreover, the performance of the inks on two different substrates was also observed to be different.

After analyzing the results, we can reasonably choose optimized heat treatment conditions for best electrical performance, according to the thickness of a-Si and ink used, as tabulated below.

Table 4.3: Best electrical characteristics of P inks at different heat treatment conditions.

Sample (thickness of a-Si layer)	Ink used	Before RPHP		After RPHP	
		iVoc (mV)	iFF (%)	iVoc (mV)	iFF (%)
100nm	P-ink 1	720 (975°C, 30min)	86.8 (975°C, 30min)	732 (950°C, 30min)	86.7 (950°C, 30min)
	P-ink 2	714 (975°C, 30min)	86 (975°C, 30min)	734 (950°C, 30min)	87 (950°C, 30min)
50nm	P-ink 1	702 (950°C, 30min)	84 (950°C, 30min)	710 (950°C, 30min)	85 (975°C, 10min)
	P-ink2	686 (925°C, 30min)	85 (925°C, 30min)	692 (925°C, 30min)	85 (925°C, 30min)

4.3.3 Evaluation of charge carrier profiles

Through the ECV method, we can develop very fine diffusion profiles of charge carriers with ‘depth resolution’ as small as 1 nm with concentration as high as 10^{21} cm^{-3} [80]. In this thesis, diffusion profile developed by P-ink 1 and P-ink 2 on lifetime samples with 100 nm thick a-Si layer, up to $\sim 0.5 \mu\text{m}$ depth, have been accurately determined. For a comparative analysis of the 50 nm thick a-Si layered samples, one can refer to results already acquired by Kiaee et al [81]. The work includes profiles of both inks on 50nm thick a-Si layered FZ lifetime samples.

Diffusion of Phosphorus in poly-Si layer depends on the role of concentration gradient of the vacancies in the layer. The diffusion profile can be divided into three regions: surface region, transition region and normal diffusion region. Profiles obtained for both P-inks in our case can also be explained using vacancy model, details of which can be found in literature [11]. From Figures 4.39 sudden shift of charge carrier concentration can be observed, after a constant value for some depth. The abrupt reduction signifies the presence of the interface, in our case the SiOx (tunnel oxide). As more evident in Figure 4.39, no data was collected near the transition from poly-Si to c-Si substrate ($\sim 0.1 \mu\text{m}$), which occurs due to carrier depletion effect.

In order to optimize the printing results, various printing resolutions were employed. Inkjet printing offers the flexibility of printing at resolutions as low as 300x300 dpi. The resolution chosen determines the number of drops deposited per inch. More droplets on same area imply a higher volume of ink deposited and hence a higher concentration of charge carriers. As from printing experiences, resolutions less than 500x500 dpi (drops per inch) do not produce enough concentration of dopants on the printed layers and hence were not applied. Moreover, at resolutions higher than 600 dpi, due to a higher thickness of the printed layers, blistering was observed after hotplate curing, which has been explained in detail in section 4.2. Indeed, ink-surface interaction is also a valid reason for blistering. Poor interactions causing poor adhesion of ink on substrate increase the chances of blistering, as well as high dewetting possibilities. The charge carrier concentration for P-ink 1 changes substantially with resolution and reduces from $5 \times 10^{19} \text{ cm}^{-3}$ at 600x600 dpi to $1.7 \times 10^{19} \text{ cm}^{-3}$ at 1000x1000 dpi. Blistering at higher resolutions may be the reason behind this. Moreover, since the concentration is measured for lifetime samples treated at 975°C , 30 min, it is also possible that the dopant source ink will have partially degraded (chemically) on the surface of the wafer, before the initiation of diffusion into the poly-Si layer. Therefore, for P-ink 2 as well, 600x600 dpi provided the best results, although being below the expected 10^{20} cm^{-3} . For P-ink 2, the resolution does not seem to have an as prominent impact on the charge carrier concentration in the diffused layer, signifying the resistance of the ink to high temperatures. It may also imply the presence of the solubility limit of phosphorus atoms in the layer, which has also been explained in section 4.2. The maximum concentration is $N_{\text{poly-Si}} = \sim 2 \times 10^{20} \text{ cm}^{-3}$. Therefore, out of the two inks, the most promising results were produced by P-ink 2 after 975°C , 30 min diffusion at 600x600 dpi.

From the curves, diffusing behavior of the charge carriers can be analyzed at the annealing condition of 975°C, 30 min across the depth of the substrate. Although a higher concentration of charged species does improve the charge carrier density and provides chances of increasing the J_{OC} (open circuit current density), however, it can also have a negative impact on the diffusion profile. This can be observed for P-ink 2 (Figure 4.40) and the decreasing slope the curves present at higher resolutions. 1200 dpi presents the least steep slope, implying the highest availability of the charged species. The depreciating impact is on the overall passivating quality of the wafer as the charge carriers diffuse into the substrate and disrupt the junction, otherwise desired for poly-Si and the substrate, in terms of their charge carrier density and thus presenting higher chances of Auger recombination. A desirable profile is produced at 600 dpi, where the property of the junction is maintained and there is a sudden drop in the concentration after a depth of $\sim 0.1 \mu\text{m}$. Higher concentration of P-atoms can also lead to lattice strains and lead to defect generation in the wafers. This can be the reason behind the degradation of the characteristics of FZ wafers, as observed in Figure 4.40.

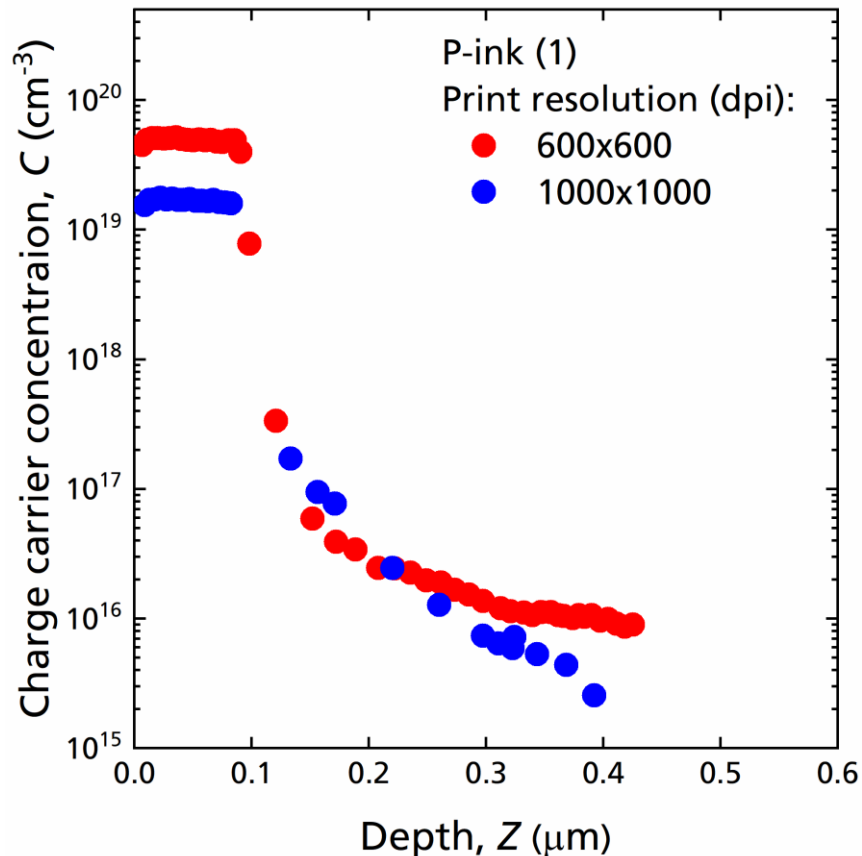


Figure 4.39: Charge carrier concentration vs. depth for selected samples doped by P-ink (1) with resolutions of 600x600 dpi and 1000x1000 dpi, annealed at 975 °C for 30 min.

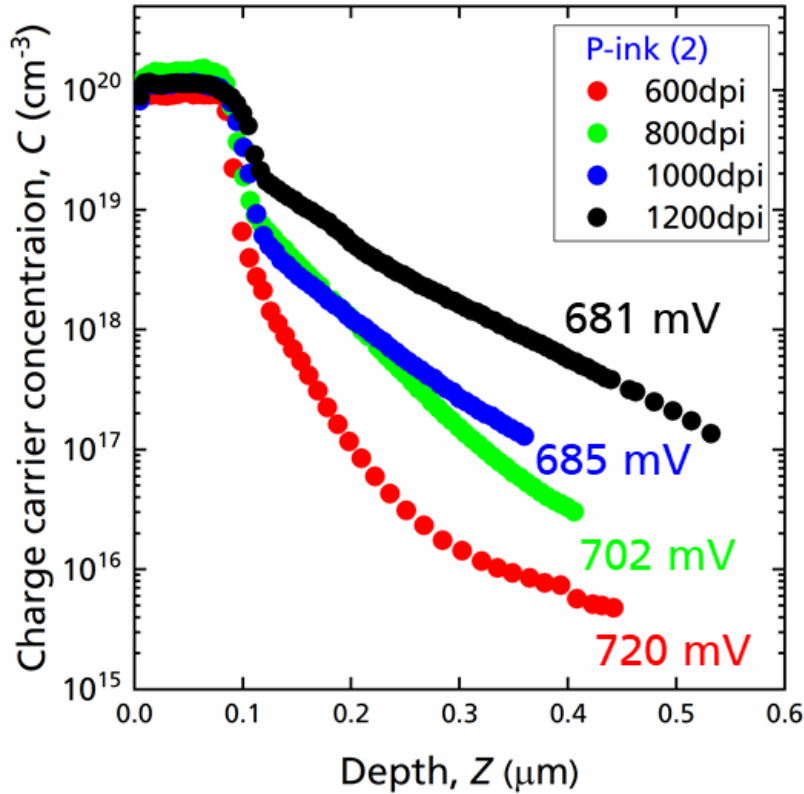


Figure 4.40 : Charge carrier concentration vs. depth for lifetime samples with 100nm a-Si layer, doped by P-ink (2) at multiple resolutions and annealed at 975 °C for 30min. iV_{oc} produced with each resolution is mentioned along the curves.

For P-ink 1, the difference between the surface and the substrate charge carrier concentration is more than three orders. For P-ink 2 with 600 dpi resolution, the surface contains an around five orders of magnitude higher number of charge carriers than the substrate. For higher resolutions, there is a gradual change of the concentration enabling a poor distinguishability between the two depths.

Summary

The distribution of charge carriers across the substrate determines the electrical property of each layer into which those charge carriers have diffused. ECV results reflect not only the concentration of active charge carriers, but also give us an idea about the junction properties of the device. A steep slope change at the transition of layers, which in our case occurs at a depth of 100 nm (0.1 μm) is desirable. A shallow peak concentration implies that the substrate (c-Si) does not contain excess minority charge carriers, which can contribute to SRH recombination traps and therefore reduce the iV_{oc} and iFF values. A correlation between the printing resolution (concentration of charge carriers) of P-ink 2 and its electrical characteristics (iV_{oc} , in particular) can be understood from the data presented in Figure 4.40. Shallow and well-defined curves are obtained for 600 x 600 dpi resolution. This coincides with the maximum iV_{oc} values, also obtained at the same resolution, as explained in detail in section 4.2. At higher resolutions, charge carriers are diffused deep into the substrate (small concentration gradient), making them unfit for solar cell applications. Similarly, for P-ink 1, a well-defined profile is again obtained for 600 x 600 dpi. Based on such experiences, printing was carried out at 600 x 600 dpi on both substrates, fetching remarkable iV_{oc} and iFF results, as high as 734 mV and 87%, respectively. On this basis it can be concluded that 600 x 600 dpi is the optimized printing resolution for best electrical performance of inks.

Chapter 5

Summary and Outlook

SUMMARY

The aim of this thesis was to comprehend relation between rheology of polymer solution based dopant source inks and their jetting/printing behavior, in the wake of optimizing inkjet printing operations. Reliable inkjet printing is another step towards making solar cell technology economically viable and affordable for masses, that being the broader objective of this research. Besides affordability, we also aimed at assessing the influence of rheology and hence inkjet printing performance of the inks in determining passivation quality of Tunnel Oxide Passivating Contacts (TOPCon). These two measures combined together, therefore ensure an improved technology at an affordable cost. To realize the same, numerous characterizations were conducted and analyzed, a brief summary of which is presented in this section.

- **Rheology – Inkjet relevance**

Phosphorus (P) and Boron (B) based inks were characterized for complex viscosity (η^*), elastic modulus (G') and viscous modulus (G'') using Piezo Axial Vibrator (PAV) Rheometer. The trend of evolution of rheological properties with respect to frequency (ω) (10-10,000Hz), temperature (25°C and 45°C) and aging time (time elapsed from filling date of ink bottles) was investigated. Inkjet working frequency lies between 1000-10,000Hz, typically around 2000 Hz. The trend of properties in this range specifically was taken into consideration.

From data it has been established, that complex viscosity plays a determinant role in defining the actuation voltage required for printing. For inks with viscosity falling in inkjet required range, i.e. 2-20 mPa.s, voltages around default actuation voltage of LP50 printer, that of 25 V suffices in producing ideal droplets with no associated tails, ligaments and satellites and minimal nozzle clogging. As a result, inkjet printing of different structures with great accuracy and precision has been made possible in this thesis. For inks with viscosity higher than these values, such as resin based dopant source inks which showed ~25 mPa.s, actuation voltage as high as 65 V is required to enable ejection of inks from the nozzle. However, it has also been observed from nature of inks which exhibited good printability, that some degree of non-Newtonian nature, which implies transition in elastic nature of inks, could help better drop formation.

The elastic component of complex modulus, as has been established in results, plays most important role in determining printability of inks. Ideally, G' value below 10 Pa, is good for stable printing. However, as experienced, more than the magnitude, trend of evolution

of G' is more important for printability. For the inks which show either an inverted parabola (vertex below 10 Pa at most) for G' (Gaussian like) or non-increasing G' (maximum below 10 Pa), tendencies of good printability were witnessed. These trends hold highest relevance within the inkjet printing range. Inks with increasing values indicate strong elastic nature, which is as undesirable for printing as is too less elasticity. For very dilute inks with too small G' , inks fail to form droplets and tend to spread over the nozzle area, whereas concentrated inks such as the ones based on resin, exhibit increasing G' which reaches 200 Pa, fail to come out of the nozzles even during purging. Therefore, an optimum value less than a decade in magnitude with non-increasing trend supports good printability.

Viscous component of complex modulus, representative of the inherent fluid nature of inks, does not play as determinant a role in printability as the other two rheological parameters do. Almost all the inks show similar linear growth of viscous component of complex modulus as all the inks are polymer based solutions in organic (alcoholic) solvents.

Besides particular response of a polymer shown by dopant source inks, based on the structure and length of its chains, there are other factors which were observed to be equally important in deciding their printability. The most important of these are the nearness of critical parameters at the operating conditions of inks, while printing. This includes both critical molecular weight of the polymer as well as critical concentration of the polymer in the solution. Solutions, which operate at the boundaries of criticality produce inconsistent results to the extent of failure of printing operations.

Temperature plays an invincible role in changing the rheology of inks. Characterizing inks at different temperatures hints towards tentative nearness of critical parameters. At higher temperatures, parameters show a reduction in their overall magnitude. However, some inks, which show the opposite behavior tend to perform poor while printing. Such inks usually lead to excessive nozzle clogging, making it difficult to obtain good prints.

Rheology of inks, as determined by the structure of inks, is found to be dependent on the natural degradation mechanisms to which an ink is subjected during storage, i.e. aging. Due to breakage of chains into shorter segments elasticity is reduced, which leads to failure of drop formation. Complex viscosity also reduces by a large scale, dropping to values ~ 1 mPa.s for some inks, which is lower than the inkjet required range. Such undesirable reductions in properties makes aged inks unfit for printing purposes.

Understanding the rheological behavior of inks, therefore, offered a perspective for optimizing the externally variable parameters (waveform frequency, jetting frequency, temperature and voltage) and tailoring the service conditions to make them conducive for producing near ideal behavior, similar to that of reference ink.

- **Electrical characteristics – doping and passivation quality**

To assess the passivation quality of TOPCon doped with inkjet printing of dopant inks, two groups of lifetime samples were prepared with a-Si layers deposited with different thicknesses (100nm and 50nm) and methods (PECVD and LPCVD). The substrates also differ in their method of fabrication: Czochralski and Float zone process, and in their surface orientation. However, thickness of passivation layer is the dominant differentiating factor. It has been observed that after annealing/diffusing at different temperatures, starting from 925°C for 10 minutes to 975°C for 30 minutes, outstanding results were given for both substrate categories.

For 100nm a-Si lifetime samples, outstanding passivation was exhibited after annealing at 975°C for 30 minutes, producing $iV_{oc} = 734\text{mV}$ and $iFF = 87\%$, for P-ink2. Values increase on increasing the dwell time and temperature in furnace.

For 50nm a-Si lifetime samples, remarkable results were produced after annealing at 925°C for 30 minutes, producing $iV_{oc} = 710\text{mV}$ and $iFF = 85\%$, for P-ink1. Values degrade on increasing the dwell time and temperature in furnace. These results are comparable to the excellent passivation results reported by Steinhauser et al [82], with an iV_{oc} of 735 mV and iFF of 88% on 200 μm thick lifetime samples.

From Electrochemical Capacitance Voltage measurements, we obtained promising results for both printable P-inks. For P-ink 1, active charge carrier concentration slightly less than 10^{20}cm^{-2} and for P-ink 2, $\sim 2 \times 10^{20}\text{cm}^{-2}$ was obtained, the latter reaching saturation solubility limit. The ink with high minority charge carrier concentration produced excellent effective lifetime ($\sim 5\text{ms}$) iV_{oc} and iFF results. Both the inks, therefore act as inexhaustible diffusion sources.

OUTLOOK

Rheological understanding of the inks enables assessment of inks in order to anticipate their printing behavior. Understanding the correlation between the rheological results and the printing behavior can further be applied to develop inks with tailor made properties to ideally suit the inkjet printer. Inks with optimized polymer molecular weight, molecular weight distribution, type of solvents, concentration of polymer in solvents and concentration of dopants in polymer chain can be developed accordingly. Judicious choice of such constitutive elements can therefore pave a way for cost-efficient technology solar cell applications. This understanding and technology can further be extended to other application where precision, homogeneity and productivity are advantageous and preferred, such as organic thin-film transistors, light-emitting diodes, conductive structures, memory devices, sensors, etc. State-of-the-art inkjet printing holds promising future for upscaling to the industrial level and making printed electronic devices economically, technologically as well ecologically more favorable.

This page is intentionally left blank.

List of Figures

Figure 1.1: Schematic cross-section of different IBC solar cells containing thin, highly doped c-Si (crystalline Si) below passivating nitride layer.	1
Figure 2.1: p-n junction of a silicon solar cell with e-h pairs being created by incoming photons with energies of $h\nu$ and electrons being swept away to the right to be used for electricity [5].	5
Figure 2.2: Energy Band Diagram with E versus k for a) GaAs and b) Silicon [6].	5
Figure 2.3: Diamond crystal structure of Silicon atom [5].	6
Figure 2.4: Energy bands (Valence band and Conduction band) of insulators, semiconductors and metals [7].	6
Figure 2.5: Infinite and finite diffusion sources [11].	10
Figure 2.6: The complete structure and working of a solar cell [12].	10
Figure 2.7: Collection probability of charge carriers under different circumstances [13].	11
Figure 2.8: (a) Equivalent circuit of an ideal solar cell; (b) Practical solar cell equivalent circuit [14].	12
Figure 2.9: (a) Energy band diagram of a p/n/p junction solar cell showing common recombination mechanisms [15], (b) Energy vs wave-vector (k) representation of recombination mechanisms [16].	13
Figure 2.10: Micro-grooved PESC [23].	16
Figure 2.11: Structure of PERC cell [23].	17
Figure 2.12: Structure of IBC solar cell [23].	17
Figure 2.13: Parallel plate model	19
Figure 2.14: Flow curves [27]	20
Figure 2.15: Stress relaxation modulus for methyl acrylate-methyl methacrylate copolymers. Dashed line represent a typical Rouse theory prediction. Adapted from Fujino et al. (1961) [29].	23
Figure 2.16: Viscosity versus the product cM , for polystyrenes at concentrations between 25 and 100%. Data at the various concentrations are shifted vertically to avoid overlap. Adapted from Graessley (1974) [29].	24
Figure 2.17: Star polymer relaxation process[29].	26
Figure 2.18: Schematic of solution process and dispersion degradation/aging [30].	27
Figure 2.19: The response of an ideal solid (spring) to the application and subsequent removal of a strain inducing force [28]	29
Figure 2.20: Response of an ideal liquid (dashpot) to the application and subsequent removal of a strain inducing force [28].	29
Figure 2.21: The Maxwell model [32].	30
Figure 2.22: Stress-strain correlations according to Maxwell's model [33].	30
Figure 2.23: Point of entanglement [35].	31

Figure 2.24: Schematic presentation of types of networks in concentrated polymer solutions involving primary bonds, secondary bonds, and entanglements [35].....	32
Figure 2.25: Maxwell’s Retarded Model [35].....	32
Figure 2.26: The idea of reptation in polymer solutions (taken from articles by Klein, 1978, and de Gennes, 1979). [29]......	34
Figure 2.27: Inkjet printing systems: (a) continuous inkjet and (b) drop-on-demand inkjet [38]......	36
Figure 2.28: Four categories of piezo DOD print-head designs, (a) squeeze mode, (b) shear mode, (c) bend mode, (d) push mode [40].....	37
Figure 2.29: PiXDRO LP50 inkjet printer (Meyer Burger Technology AG) with different parts.	38
Figure 2.30: Schematic of different phases of driving pulse for DMC print-head [41].	39
Figure 2.31: Jetting behavior of droplets from printer drop watcher, (a) favorable droplet formation, (b) formation of satellite droplets due to low surface tension, (c) random fluid spray, (d) long tail formation due to high jetting voltage or low surface tension [43].	41
Figure 2.32: Equilibrium contact angle (θ_{eq}) of a droplet on a substrate [38].....	41
Figure 2.33: Different behaviors of liquid drops upon impact with a substrate [44].	42
Figure 2.34: Wetting behavior of a droplet on a substrate [51].....	43
Figure 3.1: Schematic of experimental design of this thesis explaining steps chronologically.	44
Figure 3.2: Schematic illustration of lifetime sample.	45
Figure 3.3: A 156 mm edge length pseudo-square wafer with SiO _x passivation.....	46
Figure 3.4: Schematic of Float Zone (FZ) wafer growth [51].....	47
Figure 3.5: Schematic of lifetime samples with saw damage etched surface with 100nm a-Si layer on front side. SiO _x between a-Si and c-Si substrate is the tunneling layer.	48
Figure 3.6: Schematic of lifetime samples with shiny etched surfaces with 50nm a-Si layer on both sides. Front side is B-ion doped and the rear side is printed n-doped.	49
Figure 3.7: PAV rheometer setup at Fraunhofer ISE.	52
Figure 3.8: Geometric analog of PAV (Kirschenmann, L., Ph.D. thesis, University of Ulm, 2003) [57].	54
Figure 3.9: (a) Longitudinal cut view of Piezoelectric Axial Vibrator (PAV) rheometer used in this thesis. (b) Transverse cut view of the PAV, with top late removed. Quadratic tube contains the actor and the four piezo-elements stuck on both sides of two opposite tube walls. Remaining two walls contain four more sensors [53].	54
Figure 3.10: Picoscope 2000 series used for waveform simulation for dopant source inks[58].	57
Figure 3.11: Sinusoidal voltage as a function of time, generated by Picoscope [59].....	58
Figure 3.12: Sinusoidal voltage (marked in purple) as a function of time- output generated by Picoscope. Over time, the output signal gets attenuated. Curve in black represents input rectangular wave, distorted due to device noise (adapted from sample tests conducted by Tri Tuladhar).	59

Figure 3.13: a) Schematic representation of working principle of inkjet printing, b) MeyerBurger LP50 inkjet printer.	60
Figure 3.16: GS glovebox with gas purifier system at Fraunhofer ISE.	60
Figure 3.15: Carl Zeiss Microscope at Fraunhofer ISE.	61
Figure 3.16: Wafer Profiler CVP21 setup at Fraunhofer ISE: (a) wafer profiler, (b) sample holder.	62
Figure 3.17: Basic setup of electrochemical cell [63].	63
Figure 3.18: Schematics illustration of Sinton WCT-120 inductively coupled setup for QSSPC measurement [67].	64
Figure 4.1: Evolution of complex viscosity, viscous and elastic components of complex modulus with respect to frequency, for the reference ink.	66
Figure 4.2: Complex viscosity measurement of fresh (as received) dopant source inks with respect to frequency for: a) Batch 1, b) Batch 2 and c) Batch 3 Phosphorus and Boron inks.	69
Figure 4.3: Evolution of viscous modulus with respect to frequency for fresh (as received) dopant source inks for a) Batch 1, b) Batch 2 and c) Batch 3.	72
Figure 4.4: Evolution of Elastic (G') and Viscous (G'') components of complex modulus measurement with respect to frequency for Batch 1.	73
Figure 4.5: Evolution of Elastic (G') and Viscous (G'') components of complex modulus with respect to frequency for P-inks of Batch 2.	74
Figure 4.6: Evolution of Elastic (G') and Viscous (G'') components of complex modulus measurement with respect to frequency for B-inks of Batch 2.	75
Figure 4.7: Evolution of Elastic (G') and Viscous (G'') components of complex modulus measurement with respect to frequency for highly resinous P and B-inks of Batch 3.	76
Figure 4.8: Transition of viscosity due to change in the structure of polymer [73].	78
Figure 4.9: A typical viscoelastic spectrum for an entangled viscoelastic spectrum [28].	79
Figure 4.10: Polymer ink (P-ink 1 & 2, Batch 2) crystals around nozzle area of cartridge.	80
Figure 4.11: Resinous inks of Batch 3 retracing into the nozzle after being subjected to 60V, 5s for purging.	83
Figure 4.12: Filtration B-ink 1 of Batch 2, through a 20 μ m filter.	83
Figure 4.13: Manual pressure applied on Batch 3 ink to pass through DMC nozzle used in LP50 printer.	84
Figure 4.14: Change of rheological parameters of reference ink with respect to temperature and frequency.	85
Figure 4.15: Change of rheological parameters of P-ink (Batch 1) with respect to temperature and frequency.	86
Figure 4.16: Change of rheological parameters of B-ink (Batch 1) with respect to temperature and frequency.	87

Figure 4.17: Change of rheological parameters of a)P-ink 1, b) P-ink 2, c) B-ink 1 and d) B-ink 2 (Batch 2) with respect to temperature and frequency.	89
Figure 4.18: Change of rheological parameters of a)P-ink 1 and b)B-ink 1 (Batch 3) with respect to temperature.....	90
Figure 4.19: Change of rheological parameters of P-ink and B-ink (Batch 1) with respect to to aging time.	95
Figure 4.20: Change of rheological parameters of P-ink 1 and P-ink 2 (Batch 2) with respect to to aging time.....	96
Figure 4.21: Change of rheological parameters of B-ink 1 and B-ink 2 (Batch 2) with respect to to aging time.....	97
Figure 4.22: Change of rheological parameters of P-ink and B-ink (Batch 3) with respect to to aging time.....	98
Figure 4.23: Default waveform of PiXDRO LP50 inkjet printer.....	99
Figure 4.24: Picoscope measurement in the absence of sample; time interval between point of initiation and peak (Δ) relevant to pulse width (W_p) of waveform. Blue signal represents the rectangular input wave while the red waves represent the sinusoidal output.	100
Figure 4.25: Picoscope measurement comparing a) P-ink 1 (Batch 1) and P-ink 2 (Batch 2) and b) P-ink 1 (Batch 1) and B-ink 1 (Batch 3). With P-ink 1 acting as reference, a shift of the peak for other inks implies, that a change in the pulse width of the piezo signal is required.	101
Figure 4.26: a) Dynamic analysis of the ink-droplets by drop-watcher of LP50 printer. Volume V , velocity v , and angle of flying droplets quantify the printing behavior. As here, controlling these parameters enables achievement of precise printing of droplets onto the silicon substrate. b) $2 \times 2 \text{ cm}^2$, P-ink 1 printed areas with three different resolutions, on Saw Damage Etched surface.	104
Figure 4.27: Optical microscopic images captured after high temperature annealing of structures printed with P-ink 1 at a) 600x600 dpi, b) 800x800 dpi and c) 1000x1000 dpi resolution.	105
Figure 4.28: a) Dynamic analysis of P-ink2 by drop-watcher of LP50 inkjet printer. b) $2 \times 2 \text{ cm}^2$, P-ink 2 printed areas with three different resolutions, on saw damage etched wafers, with minimal nozzle clogging.	105
Figure 4.29: Optical microscopic images captured after high temperature annealing, for P-ink 1. The structures were printed at a resolution of a) 600 x 600 dpi, b) 800 x 800 dpi and c) 1000 x 1000 dpi.	106
Figure 4.30: a) Dynamic analysis of B-ink 1(Batch 1) by drop-watcher of LP50 inkjet printer b) $85 \times 85 \text{ cm}^2$ printed area at 600x600 dpi, on shiny etched wafers, with dominant nozzle clogging and excessive dewetting.	106
Figure 4.31: Implied open-circuit voltage ($iVOC$) of P-ink (1) and P-ink (2) printed on 100nm thick a-Si layers of lifetime sample, with resolution of 600x600 dpi, evaluated for different high-temperature processes before remote plasma hydrogen passivation (RPHP).	109
Figure 4.32: Implied fill factor (iFF) of P-ink (1) and P-ink (2) printed on 100nm a-Si layers of lifetime samples, with resolution of 600x600 dpi, evaluated for different high-temperature processes before remote plasma hydrogen passivation (RPHP).	110

Figure 4.33: Implied open-circuit voltage (*iVOC*) of P-ink (1) and P-ink (2) printed on 50nm a-Si layers of lifetime samples, with resolution of 600x600 dpi, evaluated for different high-temperature processes before remote plasma hydrogen passivation (RPHP)..... 111

Figure 4.34: Implied fill factor (*iFF*) of P-ink (1) and P-ink (2) printed on layers of 50nm thin a-Si lifetime samples at 600x600 dpi, evaluated for different high-temperature processes before remote plasma hydrogen passivation (RPHP). 112

Figure 4.35: Implied open-circuit voltage (*iVOC*) of P-ink (1) and P-ink (2) printed on 100 nm a-Si layers of lifetime samples at 600x600 dpi, evaluated for various high-temperature processes before and after remote plasma hydrogen passivation (RPHP)..... 113

Figure 4.36: Implied fill factor (*iFF*) of P-ink (1) and P-ink (2) printed on 100nm a-Si layers of lifetime samples at 600x600 dpi, evaluated for different high-temperature processes before and after remote plasma hydrogen passivation (RPHP). 114

Figure 4.37: Implied open-circuit voltage (*iVOC*) of P-ink (1) and P-ink (2) printed on 50nm a-Si layers of lifetime samples at 600x600 dpi, evaluated for different high-temperature processes before remote plasma hydrogen passivation (RPHP). 115

Figure 4.38: Implied fill factor (*iFF*) of P-ink (1) and P-ink (2) printed on 50nm thick a-Si layers of lifetime sample, with resolution of 600x600 dpi, evaluated for different high-temperature processes before and after remote plasma hydrogen passivation (RPHP). 115

Figure 4.39: Charge carrier concentration vs. depth for selected samples doped by P-ink (1) with resolutions of 600x600 dpi and 1000x1000 dpi, annealed at 975 °C for 30 min. 119

Figure 4.40 : Charge carrier concentration vs. depth for lifetime samples with 100nm a-Si layer, doped by P-ink (2) at multiple resolutions and annealed at 975 °C for 30min. *iVoc* produced with each resolution is mentioned along the curves. 120

List of Symbols

Symbol	Definition	Unit
T	Temperature	K
t	Time	sec
R	Resistance	Ω
I	Current	A
V	Voltage	V
I_{PH}	Photon-current	A
I_P	Shunt Resistance Current	A
I_D	Diode Current	A
V_D	Diode Voltage	V
I_0	Dark Saturation Current	A
I_L	Load Current	A
ρ	Resistivity	$\Omega\text{-cm}$
σ	Conductivity	S/m
iV_{OC}	Implied Open-circuit Voltage	V
V_{OC}	Open-circuit Voltage	V
I_{SC}	Short-circuit Current	A
I_{MMP}	Maximum Power Point Current	A
V_{MMP}	Maximum Power Point Voltage	V
E_F	Fermi Energy	eV
E_g	Bandgap Energy	eV
FF	Fill Factor	---
E_V	Photon Energy	eV
E	Electric Field	V/m
q	Elementary Charge	C
E_A	Activation Energy	J
j_{0E}	Emitter Saturation Current Density	fA/cm^2
J_0	Current Density	mA/cm^2
k_B	Boltzmann Constant	$J.K^{-1}$
N_A	Acceptor Concentration	cm^{-3}
N_D	Donor Concentration	cm^{-3}
n_i	Intrinsic Carrier Concentration	cm^{-3}
n	Electron Concentration	cm^{-3}
p	Hole Concentration	cm^{-3}
D	Diffusion Coefficient	cm^2/s
D_0	Diffusivity Constant	cm^2/s
C_S	Dopant Concentration at Interface	cm^{-3}
V_T	Thermal Voltage	$e.V$
τ	Lifetime	ms

List of Acronyms and Abbreviations

ISE	Institute for Solar Energy Systems
PV	Photovoltaics
Si	Silicon
B	Boron
P	Phosphorus
PSG	Phosphor-silicate Glass
FSF	Front Surface Field
BSF	Back Surface Field
FZ	Float Zone
ECV	Electrochemical Capacitance Voltage
CV	Capacitance Voltage
Cz	Czochralski
QSSPC	Quasi Steady State Photo-conductance
HNO ₃	Nitric Acid
Al ₂ O ₃	Aluminum Oxide
IBC	Interdigitated Back Contact
MPP	Maximum Power Point
PECVD	Plasma Enhanced Chemical Vapor Deposition
LPCVD	Low Pressure Chemical Vapor Deposition
SiN _x	Silicon Nitride
SiO ₂	Silicon (di) Oxide
SIMS	Secondary Ion Mass Spectroscopy
SRH	Shockley-Read-Hall
ARC	Anti-Reflection Coating
CB	Conduction Band
VB	Valence Band
PERC	Passivated Emitter and Rear Cell
PERT	Passivated Emitter Rear Totally Diffused
PERL	Passivated Emitter Rear Locally Diffused
SCR	Space Charge Region
SC1	Standard Clean 1
SC2	Standard Clean

References

- [1] F. Feldmann, M. Bivour, C. Reichel, H. Steinkemper, M. Hermle, and S. W. Glunz, “Tunnel oxide passivated contacts as an alternative to partial rear contacts,” *Solar Energy Materials and Solar Cells*, vol. 131, pp. 46–50, 2014.
- [2] M. A. Green, Y. Hishikawa, E. D. Dunlop, D. H. Levi, J. Hohl-Ebinger, and A. W.Y. Ho-Baillie, “Solar cell efficiency tables (version 52),” *Prog Photovolt Res Appl*, vol. 26, no. 7, pp. 427–436, 2018.
- [3] <https://www.suss.com/en/products-solutions/inkjet-printing>.
- [4] http://solarcellcentral.com/junction_page.html.
- [5] <http://large.stanford.edu/courses/2015/ph240/zhao-a1/>.
- [6] <http://www.students.tut.fi/~khamousk/semi.html>.
- [7] <https://www.radiation-dosimetry.org/what-is-semiconductivity-band-theory-definition/>.
- [8] A. Ural, P. B. Griffin, and J. D. Plummer, “Silicon self-diffusion under extrinsic conditions,” *Appl. Phys. Lett.*, vol. 79, no. 26, pp. 4328–4330, 2001.
- [9] A. Bentzen, “Phosphorus diffusion and gettering in silicon solar cells,” Dissertation, University of Oslo, Oslo, 2006.
- [10] G. L. Vick and K. M. Whittle, “Solid Solubility and Diffusion Coefficients of Boron in Silicon,” *J. Electrochem. Soc.*, vol. 116, no. 8, p. 1142, 1969.
- [11] Scotten W. Jones, *Diffusion in Silicon.*, 2008.
- [12] K. Mertens and G. Roth, *Photovoltaics: Fundamentals, technology and practice*. West Sussex: Wiley, 2014.
- [13] <https://www.pveducation.org/pvcdrom/solar-cell-operation/collection-probability>.
- [14] W. H. Ali, P. Cofie, J. H. Fuller, S. Lokesh, and E. S. Kolawole, “Performance and Efficiency Simulation Study of a Smart-Grid Connected Photovoltaic System,” *EPE*, vol. 09, no. 02, pp. 71–85, 2017.
- [15] R. Islam and K. Saraswat, “Limitation of Optical Enhancement in Ultra-thin Solar Cells Imposed by Contact Selectivity,” (eng), *Scientific reports*, vol. 8, no. 1, p. 8863, 2018.

- [16] Z. Yuan, A. Anopchenko, N. Daldosso, R. Guider, D. Navarro-Urrios, A. Pitanti, R. Spano, and L. Pavesi, "Silicon Nanocrystals as an Enabling Material for Silicon Photonics," *Proc. IEEE*, vol. 97, no. 7, pp. 1250–1268, 2009.
- [17] S. J. Pearton, J. W. Corbett, T. S. Shi, "Hydrogen in crystalline semiconductors," 1987.
- [18] <https://www.pveducation.org>.
- [19] <https://www.pveducation.org/pvcdrom/characterisation/bulk-lifetime>.
- [20] D. E. Kane and R. M. Swanson, "Measurement of the emitter saturation current by a contactless photoconductivity decay method (silicon solar cells)," in *18th IEEE Photovoltaic Specialists Conference Las Vegas*, Las Vegas, 1985, pp. 578–583.
- [21] A. B. Sproul, "Dimensionless solution of the equation describing the effect of surface recombination on carrier decay in semiconductors," *J. Appl. Phys.*, vol. 76, no. 5, pp. 2851–2854, 1994.
- [22] C. Reichel, F. Feldmann, R. Müller, R. C. Reedy, B. G. Lee, D. L. Young, P. Stradins, M. Hermle, and S. W. Glunz, "Tunnel oxide passivated contacts formed by ion implantation for applications in silicon solar cells," *J. Appl. Phys.*, vol. 118, no. 20, p. 205701, 2015.
- [23] A. Ebong and N. Chen, "Metallization of crystalline silicon solar cells: A review," in *High Capacity Optical Networks and Emerging/Enabling Technologies*, Istanbul, Turkey, Dec. 2012 - Dec. 2012, pp. 102–109.
- [24] A. Richter, J. Benick, F. Feldman, Ed., *Both side contacted Silicon solar cells: options for approaching 26% efficiency*.
- [25] S. W. Glunz and F. Feldmann, "SiO₂ surface passivation layers – a key technology for silicon solar cells," *Solar Energy Materials and Solar Cells*, vol. 185, pp. 260–269, 2018.
- [26] T. van Vliet and H. Lyklema, "6 - Rheology," in *Fundamentals of Interface and Colloid Science : Particulate Colloids*, J. Lyklema, Ed.: Academic Press, 2005, 6-1-6-88.
- [27] *File:Types of Non-Newtonian Fluids.png - Wikimedia Commons*. Accessed on: Mar. 11 2020.
- [28] Malvern Instruments Worldwide, *A Basic Introduction to Rheology*.
- [29] Christopher W. Macosko, *Rheology: Principles, Measurements, and Applications*: Wiley-VCH, 1994.

- [30] J. Li, I. E. Jacobs, S. Friedrich, P. Stroeve, and A. J. Moulé, “Solution aging and degradation of a transparent conducting polymer dispersion,” *Organic Electronics*, vol. 34, pp. 172–178, 2016.
- [31] David L. Allara, “Aging of polymers,” *Environmental Health Perspectives*, vol. 11, no. 29-45, 1975.
- [32] G. C. Papanicolaou and S. P. Zaoutsos, “Viscoelastic constitutive modeling of creep and stress relaxation in polymers and polymer matrix composites,” in *Woodhead Publishing series in composites science and engineering, Creep and fatigue in polymer matrix composites*, R. M. Guedes, Ed., Oxford: Woodhead Publishing, 2019, pp. 3–59.
- [33] *Maxwell and kelvin voight models of viscoelasticity presentation*. [Online] Available: <https://www.slideshare.net/Hopemungwariri/maxwell-and-kelvin-voight-models-of-viscoelasticity-presentation>. Accessed on: Mar. 12 2020.
- [34] D. C. Vadillo, T. R. Tuladhar, A. C. Mulji and M. R. Mackley, “The rheological characterization of linear viscoelasticity for ink jet fluids using piezo axial vibrator and torsion resonator rheometers,” *J. Rheol.* 54, 781-795 July/August 2010, Jun. 2010.
- [35] J. D. Ferry, “Viscoelastic properties of polymer solutions,” *Research of the National Bureau of Standards*, vol. 41, 1948.
- [36] W. Zapka, Ed., *Handbook of industrial inkjet printing: A full system approach : Volume 1 & 2*. Weinheim: Wiley-VCH, 2018.
- [37] S. Magdassi, *The chemistry of inkjet inks*. Singapore, Hackensack NJ: World Scientific, 2010.
- [38] S. D. Hoath, *Fundamentals of inkjet printing: The science of inkjet and droplets*. Weinheim: Wiley-VCH, 2016.
- [39] Roland Yudadibrata Utama, “Inkjet Printing for Commercial High-Efficiency Silicon Solar Cells,” Doctor of Philosophy, University of New South Wales, ARC Centre of Excellence for Advanced Photovoltaics and Photonics, 2009.
- [40] Yuanyuan Liu, “Inkjet printed drops and three dimensional ceramic structures.” Doctor of Philosophy, The University of Manchester, 2016.
- [41] Yuanyuan Liu, “Inkjet printed drops and three-dimensional ceramic structures: PhD Dissertation,” https://www.research.manchester.ac.uk/portal/files/60827015/FULL_TEXT.PDF, 2016.
- [42] <https://www.suss.com/en/products-solutions/inkjet-printing>.

- [43] E. R. Lee, *Microdrop Generation*: CRC Press, 2018.
- [44] R. Rioboo, M. Marengo, and C. Tropea, “Time evolution of liquid drop impact onto solid, dry surfaces,” *Exp Fluids*, vol. 33, no. 1, pp. 112–124, 2002.
- [45] K. Nakajima and N. Usami, *Crystal growth of Si for solar cells*. Berlin: Springer, 2009.
- [46] H. Kobayashi, K. Imamura, W.-B. Kim, S.-S. Im, and Asuha, “Nitric acid oxidation of Si (NAOS) method for low temperature fabrication of SiO₂/Si and SiO₂/SiC structures,” *Applied Surface Science*, vol. 256, no. 19, pp. 5744–5756, 2010.
- [47] H. Kobayashi Asuha, O. Maida, M. Takahashi, and H. Iwasa, “Nitric acid oxidation of Si to form ultrathin silicon dioxide layers with a low leakage current density,” *Journal of Applied Physics*, vol. 94, no. 11, pp. 7328–7335, 2003.
- [48] A. Fukano and H. Oyanagi, “Highly insulating ultrathin SiO₂ film grown by photooxidation,” *Journal of Applied Physics*, vol. 94, no. 5, pp. 3345–3349, 2003.
- [49] A. Moldovan, F. Feldmann, G. Krugel, M. Zimmer, J. Rentsch, M. Hermle, A. Roth-Fölsch, K. Kaufmann, and C. Hagendorf, “Simple Cleaning and Conditioning of Silicon Surfaces with UV/Ozone Sources,” *Energy Procedia*, vol. 55, pp. 834–844, 2014.
- [50] W. G. Pfann, “Principles of Zone-Melting,” *JOM*, vol. 4, no. 7, pp. 747–753, 1952.
- [51] <https://www.pveducation.org/pvcdrom/manufacturing-si-cells/float-zone-silicon>.
- [52] Martin A Green, “The path to 25% silicon solar cell efficiency: History of silicon cell evolution,” *Progress in Photovoltaics: Research and Applications*, vol. 17, 2009.
- [53] Crassous et al., “Characterization of the viscoelastic behavior of complex fluids using the piezoelastic axial vibrator,”
- [54] G. H. McKinley and T. Sridhar, “FILAMENT-STRETCHING RHEOMETRY OF COMPLEX FLUIDS,” *Annu. Rev. Fluid Mech.*, vol. 34, no. 1, pp. 375–415, 2002.
- [55] S. D. Hoath, I. M. Hutchings, G. D. Martin, T. R. Tuladhar, M. R. Mackley, and D. Vadhilo, “Links Between Ink Rheology, Drop-on-Demand Jet Formation, and Printability,” *J. Imaging Sci. Technol.*, vol. 53, no. 4, p. 41208, 2009.
- [56] L. Kirschenmann and W. Pechhold, “Piezoelectric Rotary Vibrator (PRV) – a new oscillating rheometer for linear viscoelasticity,” *Rheol Acta*, vol. 41, no. 4, pp. 362–368, 2002.

- [57] D. C. Vadillo, T. R. Tuladhar, A. C. Mulji, and M. R. Mackley, "The rheological characterization of linear viscoelasticity for ink jet fluids using piezo axial vibrator and torsion resonator rheometers," *Journal of Rheology*, vol. 54, no. 4, pp. 781–795, 2010.
- [58] <https://www.picotech.com/oscilloscope/2000/picoscope-2000-specifications>.
- [59] P. Technology, "PicoScope 6 User's Guide,"
- [60] "Chapter 5: Electrochemical Capacitance-Voltage (C-V) Measurements of CBE Grown InP Layers," pp. 111–140.
- [61] E. Peiner, A. Schlachetzki, and D. Krüger, "Doping profile analysis in Si by electrochemical capacitance-voltage measurements," *J. Electrochem. Soc.*, vol. 142, no. 2, pp. 576–580, 1995.
- [62] B. Sermage, Z. Essa, N. Taleb, M. Quillec, J. Aubin, J. M. Hartmann, and M. Veillerot, "Electrochemical capacitance voltage measurements in highly doped silicon and silicon-germanium alloys," (English), *Journal of Applied Physics*, vol. 119, no. 15, 2016.
- [63] D. K. Schroder, *Semiconductor material and device characterization*. Hoboken, New Jersey, Piscataway, New Jersey: IEEE Press Wiley-Interscience; IEEE Xplore, 2006.
- [64] <https://www.probion.fr/en/tutorials/ecvp/ecvprofiling.html>.
- [65] R. A. Sinton and A. Cuevas, "Contactless determination of current–voltage characteristics and minority-carrier lifetimes in semiconductors from quasi-steady-state photoconductance data," *Appl. Phys. Lett.*, vol. 69, no. 17, pp. 2510–2512, 1996.
- [66] R. A. Sinton, A. Cuevas, and M. Stuckings, "Quasi-steady-state photoconductance, a new method for solar cell material and device characterization," in *25th IEEE Photovoltaic Specialists Conference Washington DC*, Washington DC, 1996, pp. 457–460.
- [67] Halvard Haug, "New methods fro investigation of surface passivation layers for crystalline silicon solar cells.," *Philosophiae Doctor*, University of Oslo, Oslo, 2014.
- [68] Zhou et sal, "Dopant ink composition for forming doped regions in semiconductor substrates, and methods for fabricating dopant ink compositions," US 8,975,170 B2 13/280,077.
- [69] P. Cheng, C. Yan, Y. Li, W. Ma, and X. Zhan, "Diluting concentrated solution: a general, simple and effective approach to enhance efficiency of polymer solar cells," *Energy Environ. Sci.*, vol. 8, no. 8, pp. 2357–2364, 2015.

- [70] Basheer Al-Shammari, Tariq Al-Fariss, Fares Al-Sewailm, Rabeh Elleithy, “Effects of Polymer Concentration and Cross-Linking Density on Rheology of Chemically Cross-Linked Poly(vinyl alcohol) near the Gelation Threshold,”
- [71] N.F. Morrison and O.G. Harlen, Ed., *Inkjet printing of non-Newtonian fluids: .*, 2011.
- [72] S. D. Hoath, I. M. Hutchings and G. D. Martin, T. R. Tuladhar, M. R. Mackley and D. Vadillo, “Links Between Ink Rheology, Drop-on-Demand Jet Formation, and Printability,” *Journal of Imaging Science and Technology*® 53(4): 041208–041208-8, 2009., 2009.
- [73][http://support.moldex3d.com/r15/en/standardinjectionmolding_material_materialmodels_viscositymodel\(thermoplasticonly\).html](http://support.moldex3d.com/r15/en/standardinjectionmolding_material_materialmodels_viscositymodel(thermoplasticonly).html).
- [74] C. Wagner, Y. Amarouchene, D. Bonn, and J. Eggers, “Droplet detachment and satellite bead formation in viscoelastic fluids,” (eng), *Physical review letters*, vol. 95, no. 16, p. 164504, 2005.
- [75] David F. James and John H. Saringer, “Flow of dilute polymer solution through converging channels,” Apr. 1982.
- [76] A. Lee, K. Sudau, K. H. Ahn, S. J. Lee, and N. Willenbacher, “Optimization of Experimental Parameters to Suppress Nozzle Clogging in Inkjet Printing,” *Ind. Eng. Chem. Res.*, vol. 51, no. 40, pp. 13195–13204, 2012.
- [77] Keefer, “Hydrolysis of silicate glasses,” 1984.
- [78] F. Feldmann, M. Bivour, C. Reichel, M. Hermle, and S. W. Glunz, “Passivated rear contacts for high-efficiency n-type Si solar cells providing high interface passivation quality and excellent transport characteristics,” *Solar Energy Materials and Solar Cells*, vol. 120, pp. 270–274, 2014.
- [79] Z. Kiaee, C. Reichel, M. Nazarzadeh, R. Keding, F. Feldmann, J. D. Huyeng, M. Jahn, R. Singh, M. Hermle, F. Clement, Ed., *Inkjet-printing of phosphorus and boron dopant sources for tunnel oxide passivating contacts*, 2019.
- [80] H. Wu, G. Ru, Y. Zhang, C. Jin, B. Mizuno, Y. Jiang, X. Qu, and B. Li, “Electrochemical capacitance-voltage characterization of plasma-doped ultra-shallow junctions,” *Front. Electr. Electron. Eng. China*, vol. 3, no. 1, pp. 116–119, 2008.
- [81] Kiaee et al., Ed., *Printed dopant sources for locally-doped SiOx/poly-Si passivating contacts*, 2018.

[82] B. Steinhauser, J.-I. Polzin, F. Feldmann, M. Hermle, and S. W. Glunz, "Excellent Surface Passivation Quality on Crystalline Silicon Using Industrial-Scale Direct-Plasma TOPCon Deposition Technology," *Sol. RRL*, vol. 2, no. 7, p. 1800068, 2018.

ACKNOWLEDGEMENT

Reaching a goal marks an achievement, no matter how big or small. It is an acknowledgment of one's toil. Nevertheless, success never belongs to the person alone. An accomplishment is a testimony to all the support one receives, material or immaterial. This work also carries with it efforts of many people, to whom I am immensely grateful.

I would begin with expressing my sincere gratitude to my supervisor, Dr Zohreh Kiaee for selecting me for this work. She has been a true guidance, throughout. Under her supervision, besides improving my academic skills, I have learnt much more. Through her valuable discussions and accompaniment during experimental sessions, I have learnt tremendously in ways both obvious and subtle. She has always been extremely patient and encouraging through my shortcomings. It was through her praiseworthy management that I could assimilate as much information in this time, which never seemed enough. She will always be as an inspiration.

I am highly thankful to Dr Roman Keding for having included me in his team and providing a welcoming and supportive environment to all his team members. I am thankful to Dr Christian Reichel in designing and developing the theory behind my experimentation along with Dr Zohreh.

The gratitude goes equally to my supervisor from Politecnico di Milano, Professor Francesco Briatico Vangosa, who always replied timely to all my queries and put an end to all my curiosities related to this work. I am thankful to him for deciding to be my internal supervisor. I am thankful to Professor Roberto Frassine for teaching me a course on 'Mechanical Durability of Polymers', which was of significant importance during my thesis, besides directing me to Prof. Francesco for supervision. I would also like to mention my co-rapporteur Prof Roberto Chiesa, who guided me from the beginning in matters concerning my thesis and otherwise. I feel honored to be a student of such professors.

At Fraunhofer ISE, many people have supported me, including but not limited to Mike Jahn (through all the printing troubles), by Raj (in various laboratories) and by Andreas Losel. Their support has strengthened the technical part of my work.

I am thankful to my friends at Fraunhofer alike for their company, which helped during my stressful moments. Aathira, Eyerusalem, Khadija, Bilal, Taimoor, Milad, Marcel and Kaveh- for making 'The Container' an office that I shall remember.

I am especially thankful to Zohreh, Milad and Richard for the long printing sessions we have had together. Certainly working with them has been enjoyable. Richard was helpful especially during the completion of my thesis.

My acknowledgment would be incomplete without thanking Hannan, who introduced me to Fraunhofer ISE. I will always owe to him.